

Sea-ice surface properties and their impact on the under-ice light field from remote sensing data and in-situ measurements

Dissertation

zur Erlangung des Grades
Doktor der Naturwissenschaften
- Dr. rer. nat. -

vorgelegt im
Fachbereich 1 (Physik/Elektrotechnik)
der Universität Bremen

von

Stefanie Arndt

November 2016



1. Gutachter: Prof. Dr. Peter Lemke
2. Gutachter: Prof. Dr. Christian Haas

Die Dissertation wurde angefertigt am

Alfred-Wegener-Institut Helmholtz-Zentrum für Polar- und Meeresforschung

in Betreuung durch die Gutachter und Dr. Marcel Nicolaus, Dr. Wolfgang Dierking und
Dr. Sascha Willmes

*The noise resembles the roar of heavy,
distant surf. Standing on the stirring ice
one can imagine it is disturbed by the
breathing and tossing of a mighty giant below.*

- Ernest Shackleton (1874–1922) -

Abstract

The surface properties of sea ice dominate many key processes and drive important feedback mechanisms in the polar oceans of both hemispheres. Examining Arctic and Antarctic sea ice, the distinctly different dominant sea-ice and snow properties in spring and summer are apparent. While Arctic sea ice features a seasonal snow cover with widespread surface ponding in summer, a year-round snow cover and strong surface flooding at the snow/ice interface is observed on Antarctic sea ice. However, substantial knowledge gaps exist about the spatial distribution and temporal evolution of these properties, and their impacts on exchange processes across the atmosphere/ocean interface. This thesis aims to overcome these limitations by quantifying the influence of surface properties on the energy and mass budgets in the ice-covered oceans.

Remote sensing data and in-situ observations are combined to derive the seasonal cycle of dominant sea-ice surface characteristics, and their relation to the transfer of solar radiation from the atmosphere through snow and sea ice into the upper ocean.

This thesis shows that characteristics of the solar radiation under Arctic sea ice can be described directly as a function of sea-ice surface properties as, e.g., sea-ice type and melt pond coverage. Using this parameterization, an Arctic-wide calculation of solar radiation through sea ice identifies the surface melt onset as the main driver of the annual sea-ice mass and energy budgets.

In contrast, an analysis of the spring-summer transition of Antarctic sea ice using passive microwave satellite observations indicates widespread diurnal freeze-thaw cycles in the top snow layers. While the associated temporary thawing is identified as the predominant melt process, subsequent continuous melt in deeper snow layers is rarely found on Antarctic sea ice. Instead of directly influencing the snow depth on Antarctic sea ice, these melt processes rather modify the internal stratigraphy and vertical density structure of the snowpack. An additional analysis of satellite scatterometer observations reveals that snow volume loss on Antarctic sea ice is mainly driven by changes in the lower snowpack, due to the widespread presence of sea-ice surface flooding and snow-ice formation prior to changes in the upper snowpack. As a consequence, the largely heterogeneous and metamorphous Antarctic snowpack prevents a direct correlation between surface properties and the respective characteristics of the penetrating solar radiation under the sea ice. However, surface flooding is identified as the key process governing the variability of the

under-ice light regime on small scales.

Overall, this thesis highlights that the mass and energy budgets of Antarctic sea ice are determined by processes at the snow/ice interface as well as the temporal evolution of physical snowpack properties. These results are in great contrast to presented studies on Arctic sea ice, where seasonally alternating interactions at the atmosphere/snow- or atmosphere/sea-ice interface control both the energy and mass budgets. An improved understanding of the seasonal cycle of dominant sea-ice and snow surface characteristics in the Arctic and Antarctic is crucial for future investigations retrieving sea-ice variables, such as sea-ice thickness and snow depth, from recent microwave satellite observations.

Contents

Abstract	I
List of Acronyms	VII
1 Thesis - motivation and outline	1
1.1 Motivation	1
1.2 Scope of the thesis	3
1.3 Thesis outline	4
1.4 Publications within the thesis	5
2 Sea ice - an overview	7
2.1 The role of sea ice in the climate- and ecosystem	7
2.2 Snow on sea ice	10
2.3 Temporal evolution of surface properties of Arctic and Antarctic sea ice . .	10
2.4 Ongoing changes of sea ice in both hemispheres	12
2.5 Remote sensing of sea ice and snow	16
3 The impact of Arctic sea ice surface melt on transmitted heat fluxes	23
3.1 Introduction	23
3.2 Theoretical background	25
3.2.1 Optical properties of sea ice	25
3.2.2 Surface energy budget of sea ice	26
3.3 Method	27
3.3.1 Solar heat flux equations	28
3.3.2 Seasonality of surface properties and transmittance of Arctic sea ice	30
3.3.3 Deriving trends	33
3.3.4 Input data sets	34
3.4 Results	36
3.4.1 Seasonal cycle of solar radiation under Arctic sea ice in 2011	36
3.4.2 Light transmission from 1979 to 2011	37
3.5 Discussion	39
3.5.1 Seasonality and trends of transmitted fluxes	39

Contents

3.5.2	Comparison with field data	40
3.5.3	Limitation	43
3.5.4	Sensitivity studies	44
3.5.5	Additional parameters influencing the Arctic under-ice light field . .	46
3.6	Summary and Conclusions	48
4	Timing and regional patterns of snowmelt on Antarctic sea ice from passive microwave satellite observations	51
4.1	Introduction	51
4.2	Melt transition retrieval from passive microwave data	53
4.2.1	Background	53
4.2.2	Melt onset proxies from passive microwave data	54
4.2.3	Melt transition retrieval	56
4.2.4	Data sets	58
4.3	Results	58
4.3.1	Spatial variability of snowmelt patterns	58
4.3.2	Characteristic regions and surface melt types	60
4.4	Discussion	62
4.4.1	Limitations and uncertainties	62
4.4.2	Comparison of surface melt patterns with field data and previous studies	64
4.4.3	Decadal variability of snowmelt patterns	67
4.5	Summary and Conclusions	68
5	Retrieval of seasonal snowmelt stages on Antarctic sea ice from satellite scatterometer observations	71
5.1	Introduction	71
5.2	Snowmelt retrieval from satellite scatterometer data	73
5.2.1	Data sets	73
5.2.2	Methods	74
5.3	Results	77
5.3.1	Study locations	77
5.3.2	Spatial variability	79
5.4	Evaluation of transitions from satellite scatterometer observations	80
5.4.1	Inter-comparison of active microwave observations	80
5.4.2	Limitations of the assembled time series of satellite scatterometer observations	82
5.4.3	Comparison with melt transition from passive microwave data . . .	83
5.4.4	Time series of transition dates	85
5.5	Summary and Conclusions	86

6	Influence of surface properties on light transmission through Antarctic sea ice	89
6.1	Introduction	89
6.2	Data and Methods	91
6.2.1	Study site and measurements	91
6.2.2	Data analyses	93
6.3	Results	96
6.3.1	Physical properties of the ice floe and their distribution functions . .	96
6.3.2	Light attenuation	98
6.3.3	Spectral correlation surfaces	99
6.3.4	Spectral light attenuation and transmission	100
6.4	Discussion	102
6.4.1	Spatial variability of the under-ice radiation	102
6.4.2	Comparison to Arctic light transmittance	103
6.5	Summary and Conclusions	104
7	Key findings and Outlook	107
7.1	Implications of seasonal effects on the sea-ice mass and energy budgets: A bi-polar view	107
7.2	Knowledge gain for remote sensing applications	112
7.3	Ideas for future field campaigns and research	114
	Bibliography	116
	List of Figures	139
	List of Tables	141
	Acknowledgements	143
	Curriculum Vitae	149
	Erklärung	149

List of Acronyms

AMSR-E	Advanced Microwave Scanning Radiometer - Earth Observing System
ASCAT	Advanced Scatterometer
ASL	Amundsen Sea Low
CDW	Circumpolar Deep Water
EASE-Grid	Equal-Area Scalable Earth-Grid
ECMWF	European Centre for Medium-Range Weather Forecasts
EFO	Early Freeze Onset
EMO	Early Melt Onset
ENSO	El Niño-Southern Oscillation
ERS-1/2	European Remote Sensing platforms
FO	Freeze Onset
FYI	First-year ice
GEM-2	Ground-based multi-frequency electromagnetic induction instrument
ICDC	Integrated Climate Data Center
IMB	Ice Mass-balance Buoy
ITP	Ice-tethered profiler
LBL	Long baseline positioning system
MIZ	Marginal-ice zone
MO	Melt Onset
MODIS	Moderate Resolution Imaging Spectroradiometer
MYI	Multi-year ice
NASA	National Aeronautics and Space Administration
NDI	Normalized difference index
NIR	Near-infrared spectrum
NSIDC	National Snow and Ice Center
NUI	Nereid Under-Ice
OSI SAF	Ocean and Sea Ice Satellite Application Facilities
QSCAT	Quick Scatterometer (QuikSCAT)
ROV	Remotely Operated Vehicle
SAM	Southern Ocean Annual Mode
SCP	Scatterometer Climate Record Pathfinder

List of Acronyms

SHEBA	Surface Heat Budget of the Arctic Ocean
SIC	Sea-ice concentration
SIE	Sea-ice extent
SIPEX	Sea Ice Physics and Ecosystems Experiment
SIR	Scatterometer Image Reconstruction
SSM/I	Special Sensor Microwave Imager
SSMIS	Special Sensor Microwave Imager/ Sounder
SMO	Continuous Snowmelt Onset
TeSMO	Temporary Snowmelt Onset
TIR	Thermal-infrared spectrum
VIS	Visible spectrum
WISKEY	Winter studies on sea ice and key species
WWOS	Winter Weddell Outflow Study
XPR	Cross-polarized ratio

1

1.1 Motivation

Sea ice is a crucial component in the Earth's climate system. It dominates the exchange processes between the atmosphere and the ocean in the polar regions, and alters therefore seasonal and inter-annual variations at the ocean/atmosphere interface. Since sea ice acts as a sensible indicator of climate change, it undergoes remarkable opposing trends in sea-ice extent, age and season duration in in the Arctic with respect to the Antarctic. While Arctic sea ice reveals an overall declining trend in its extent, thickness, and age during the last decades, the sea-ice cover of the southern hemisphere has expanded on average. Moreover, the Antarctic-wide positive trend is composed of regionally-opposing sea-ice changes, especially between East and West Antarctica. Although several studies suggest changes in the large-scale atmospheric and oceanic circulation patterns as main drivers for the increase in Antarctic sea-ice extent and the strong regional sea-ice variability, the seasonal and inter-annual variability of snow- and surface properties and thickness of Antarctic sea ice is rarely studied in this context. Moreover, the impact of the temporal variability and spatial distribution of changing physical properties of the Antarctic snowpack and associated snowmelt processes on the mass and energy budgets of sea ice is less quantified so far.

Looking at Arctic and Antarctic sea ice, it is apparent that not only the sea-ice extent evolves in opposite ways during the last decades, but also the seasonality of the snow and sea-ice surface properties differ crucially in both hemispheres (Figure 1.1). The different seasonal evolution of surface properties and its associated interaction with the atmosphere and ocean plays an essential role for the mass and energy budgets of Arctic and Antarctic sea ice, as well as the ice-associated ecosystem. However, recent studies on the interaction of shortwave radiation and Arctic sea ice are limited to specific regions and/or seasons of the year, while large-scale, multi-seasonal, and inter-annual changes of the partitioning of solar radiation between atmosphere, sea ice and ocean are sparse. The remoteness of the Antarctic leads to even less knowledge on the relation between Antarctic sea-ice surface properties and their impact on the energy and mass budgets of the ice-covered

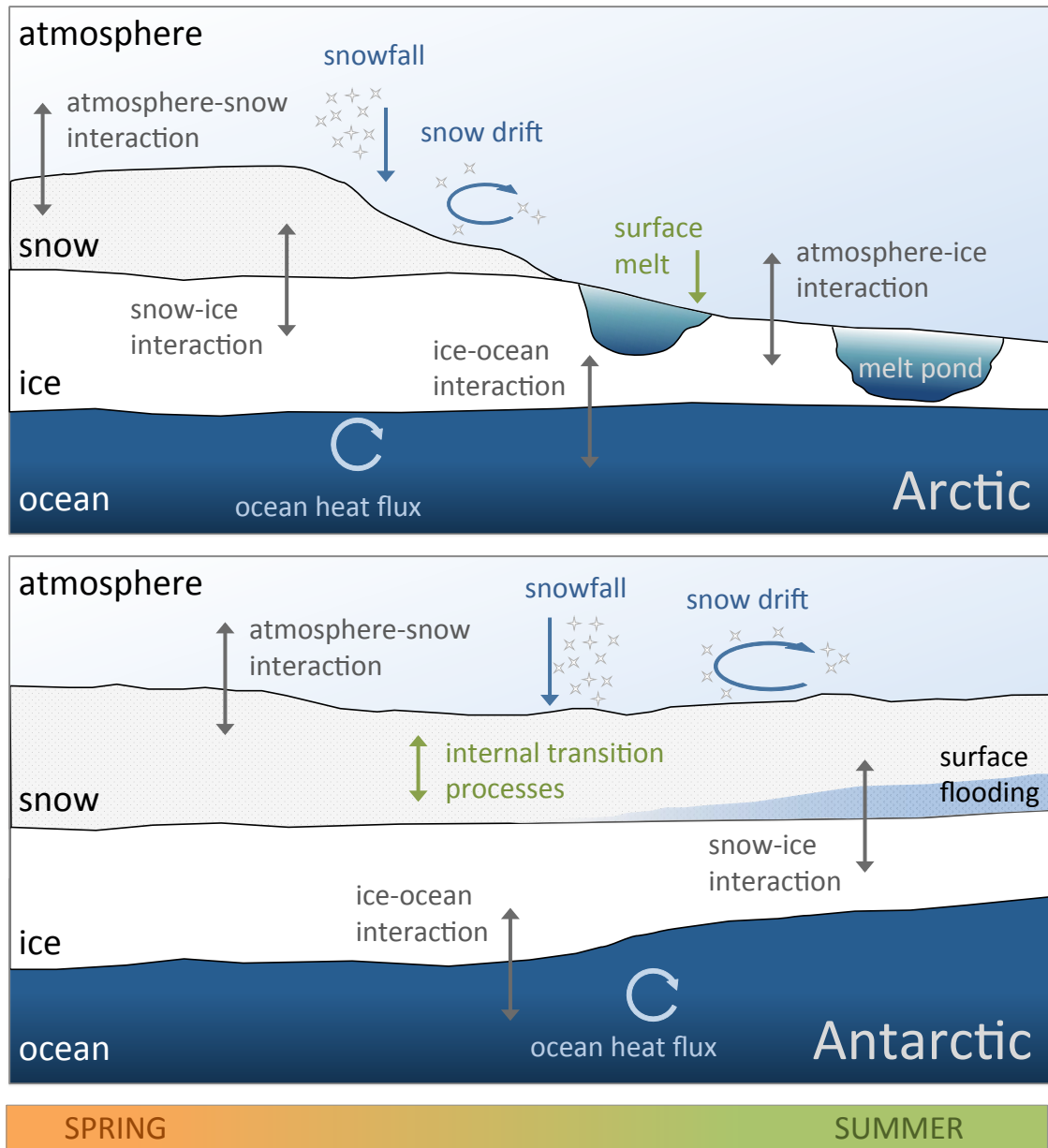


Figure 1.1: Schematic of dominant processes and interactions in the northern (upper panel) and southern (lower panel) ice-covered ocean during the spring-summer transition. To highlight the opposing seasonal evolution of surface and bottom melt processes of Arctic and Antarctic sea ice, this schematic neglects that sea ice floats in a hydrostatic equilibrium.

Southern Ocean. While the widespread ponding of Arctic sea ice is known to dominate the bright under-ice light regime in the northern polar regions, it is poorly understood how the characteristic metamorphous Antarctic snow layer and the prevalent flooding at the snow/ice interface of Antarctic sea ice influence the under-ice light field.

1.2 Scope of the thesis

The observed ongoing change of sea ice in both hemispheres has not only an impact on the mass budget of sea ice but also on the partitioning of solar radiation between atmosphere, sea ice, and ocean (e.g. Cavalieri and Parkinson, 2012; Parkinson and Cavalieri, 2012; Stammerjohn et al., 2012; Turner et al., 2015, Section 2.4). Thus, the transition of Arctic sea ice towards a thinner and more seasonal ice cover, associated with an earlier surface melt onset and increasing melt pond coverage, might also affect the energy budget of Arctic sea ice as well as the ice-associated ecosystem (e.g. Perovich et al., 2007b; Perovich and Polashenski, 2012; Stroeve et al., 2014, Section 2.1 and 2.4). Therefore, the **first research question** for this thesis is:

What is the quantitative impact of the ongoing change in Arctic sea-ice conditions on the large-scale, multi-seasonal, and inter-annual partitioning of solar energy in the system and the associated changes in the mass budget of Arctic sea ice?

Arctic and Antarctic sea-ice areas are known as being rather different. This is studied not only regarding their opposing evolution in sea-ice extent during the last decades (e.g. Stammerjohn et al., 2012, Section 2.4) but particularly in their distinctly different dominant surface properties in spring and summer. While snow melts on Arctic sea ice during the spring-summer transition and the subsequent surface melt leads to a widespread ponding of the sea-ice surface, snow persists year-round on Antarctic sea ice (e.g. Massom et al., 2001; Perovich and Polashenski, 2012, Section 2.2). Nevertheless, the physical properties of the southern snowpack are modified during the seasonal cycle. Therefore, the **second research question** for this thesis is:

Which processes and mechanisms drive the temporal variability and spatial distribution of physical properties and associated surface melt of the snowpack on Antarctic sea ice?

The opposing sea-ice surface properties of Arctic and Antarctic sea ice during the spring-summer transition do also lead to crucially different relations between surface properties and their impact on the energy and mass budgets of the northern and southern hemisphere. Therefore, the **third research question** for this thesis is:

How do the distinctly different summer surface properties between northern and southern hemisphere sea-ice cover influence the partitioning of solar radiation between atmosphere, sea ice and ocean as well as the seasonal mass budget of the contrasting Arctic and Antarctic sea-ice cover?

1.3 Thesis outline

The thesis is organized in four main chapters. In addition, Chapter 2 gives an overview on sea ice as a major component in the polar climate- and ecosystem as well as its connection to remote sensing applications. The main part of the content of the following chapters is based on three studies that have already been published (Chapter 3 and 4) or are still in peer-review process (Chapter 6). Another unpublished chapter (Chapter 5) supplements the investigations of this thesis. Thus, the chapters form independent studies building on each other. Due to a separate introduction, methodology, and summary part for every chapter, there is partial overlap in the contents of different chapters, e.g. regarding the literature review, but the chapters are consistent in it.

Chapter 3 focuses on the quantification of solar radiation fluxes through Arctic sea ice for the entire Arctic during all seasons of the year and is investigating on the first research question (Section 1.2). For this purpose, a new parameterization of light transmittance through Arctic sea ice as a function of variable sea-ice properties and their seasonality is developed. The chapter is based on Arndt and Nicolaus (2014), published in *The Cryosphere*.

Based on the results of Chapter 3, **Chapter 4** takes up the importance of the seasonality of surface properties for the energy and mass budgets not only for Arctic but also for Antarctic sea ice. Therefore, a method is developed to derive the two stages of snowmelt with a regionally adaptive approach from passive microwave data. The distinguished temporary and continuous snowmelt stages allow characterizing the dominant melt patterns on Antarctic sea ice. This work is investigating on the second research question (Section 1.2). This chapter is published as Arndt et al. (2016) in the *Journal of Geophysical Research: Oceans*.

In order to resolve also seasonal melt processes in the lower snowpack, a similar snowmelt onset retrieval method as for the passive microwave satellite observations is applied on satellite scatterometer observations in **Chapter 5** supplementing the second research question. Therefore, data from the satellites ERS-1/2, ASCAT and QSCAT are combined to provide a decent time series.

In **Chapter 6** the previously discussed snow and surface properties of Antarctic sea ice are related to their optical properties and the associated impact on the mass and energy budgets leading to an improved understanding of the third research question. The study is based on field measurements during the ship-borne expedition WHISKY. The chapter is currently under review as Arndt et al. (under review) in the *Journal of Geophysical Research: Oceans*.

Finally, **Chapter 7** summarizes the main achievements of this thesis and provides an outlook on potential future work.

1.4 Publications within the thesis

Publication 1 – Arndt & Nicolaus (2014)

Arndt, S., M. Nicolaus (2014): Seasonal cycle and long-term trend of solar energy fluxes through Arctic sea ice. *The Cryosphere*, 8(6), 2219–2233, doi: 10.5194/tc-8-2219-2014.

Author contributions

Stefanie Arndt developed the idea and concept of the study. She developed the parameterization of the light transmittance through Arctic sea ice for all seasons, as well as the subsequent up-scaling of the approach for the entire Arctic. She performed all necessary calculations, and analyzed and discussed the results. Marcel Nicolaus provided ideas for the concept of the study and its discussion. Both authors wrote the manuscript.

Part of the work of this paper has been conducted in the framework of the Master’s thesis by the author (Arndt, 2013). Here, the parameterization and up-scaling approach were developed. Within the framework of this dissertation the study was extended to the calculation of corresponding potential sea-ice bottom melt in order to relate the inter-annual changes in the Arctic-wide energy budget to sea-ice mass budget changes. Moreover, the results were discussed more detailed regarding limitations of the study and were related to recent studies on the Arctic energy budget.

Publication 2 – Arndt et al. (2016)

Arndt, S., M. Nicolaus, W. Dierking, S. Willmes (2016): Timing and regional patterns of snowmelt on Antarctic sea ice from passive microwave satellite observations, *Journal of Geophysical Research: Oceans*, 121(8), 5916–5930, doi: 10.1002/2015JC011504.

Author contributions

All authors discussed possibilities to improve and extend the previous study by Willmes et al. (2009) to distinguish different snowmelt processes and describe dominant melt patterns. Stefanie Arndt developed the methodology to retrieve the two melt transitions, analyzed the results, discussed them regarding uncertainties, limitations and comparisons with available field data and previous studies. All authors contributed ideas and input for the analysis and discussion and wrote the manuscript.

Publication 3 – Arndt et al. (under review)

Arndt, S., K. M. Meiners, R. Ricker, T. Krumpfen, M. Nicolaus (under review): Influence of snow thickness and surface flooding in light transmission through Antarctic pack ice, *Journal of Geophysical Research: Oceans*.

Author contributions

Stefanie Arndt processed and analyzed the data, plotted and discussed the results and wrote most of the manuscript. Klaus M. Meiners, Robert Ricker and Thomas Krumpfen participated in the ship-based campaign. All authors contributed ideas for the analysis and discussion, and improved the manuscript.

The manuscript preparation and writing is the result of the granted outgoing scholarship provided by the graduate school POLMAR for a research stay of Stefanie Arndt at the Antarctic Climate & Ecosystem Cooperative Research Centre in Hobart (Tasmania).

Publication 4 – Katlein et al. (2015)

Katlein, C., **S. Arndt**, M. Nicolaus, M. V. Jakuba, S. Elliott, L. L. Whitcomb, C. J. McFarland, S. Suman, D. K. Perovich, R. Gerdes, A. Boetius and C. R. German (2015): Influence of ice thickness and surface properties on light transmission through Arctic sea ice, *Journal of Geophysical Research: Oceans*, 120(9), 5932–5944, doi: 10.1002/2015JC010914.

Author contributions

The majority of the authors participated in the ship-based campaign and were involved in the study planning and data acquisition. Christian Katlein performed most of the calculation and analyzed and discussed the results. All authors, including Stefanie Arndt, provided input for the analysis and discussions of the results and wrote of the manuscript.

2.1 The role of sea ice in the climate- and ecosystem

The Earth's climate system is a complex and interactive system composed of atmosphere, ocean, biosphere, pedosphere and cryosphere. Interactions between atmosphere and ocean are the most essential elements in the global system as their mutual exchange of energy and matter determine environmental conditions. Even though the sea-ice cover at higher latitudes is, on a global scale, a comparable thin layer, it alters the interactions between atmosphere and ocean crucially. The insulating layer modifies both, the exchange of heat and matter fluxes but also the transfer of momentum at the ocean/atmosphere interface (Dieckmann and Hellmer, 2010).

The periodic freeze up of the upper ocean and melting of sea ice is a direct response of atmospheric variations in the polar regions, such as surface temperature and incoming solar radiation. These seasonal variations of the northern and southern sea-ice cover are one of the major components of the annual cycle of the Earth's surface. While Arctic sea ice reaches its minimum sea-ice extent in September and maximum in February, the minimum sea-ice extent of Antarctic sea ice is reached in March and the maximum in September (Figure 2.1, Comiso (2010)). The two polar sea-ice covers do not only differ in the seasonal cycle of sea-ice extent but particularly in their geographical setting, respective sea-ice growth and decay processes, the seasonality of surface processes, as well as large-scale climate and ice-ocean interactions and feedback mechanisms.

Arctic sea ice forms in a basin surrounded by landmasses of the Eurasian and American continents whereas the Antarctic continent is surrounded by the Southern Ocean and the adjacent Indian, Atlantic and Pacific Oceans. The annual variation of sea-ice extent is therefore much larger in the Antarctic (3 to 19×10^6 km²) compared to the Arctic (4 to 16×10^6 km²), since sea-ice formation and drift is not limited by surrounding landmasses (Dieckmann and Hellmer, 2010) (Figure 2.1). Moreover, Antarctic sea ice extends to much lower latitudes (about 60 to 70°) compared to the Arctic sea ice (about 70 to 90°) (Maksym et al., 2012).

During the sea-ice formation processes, most of the salt dissolved in the ocean water is

2 Sea ice - an overview

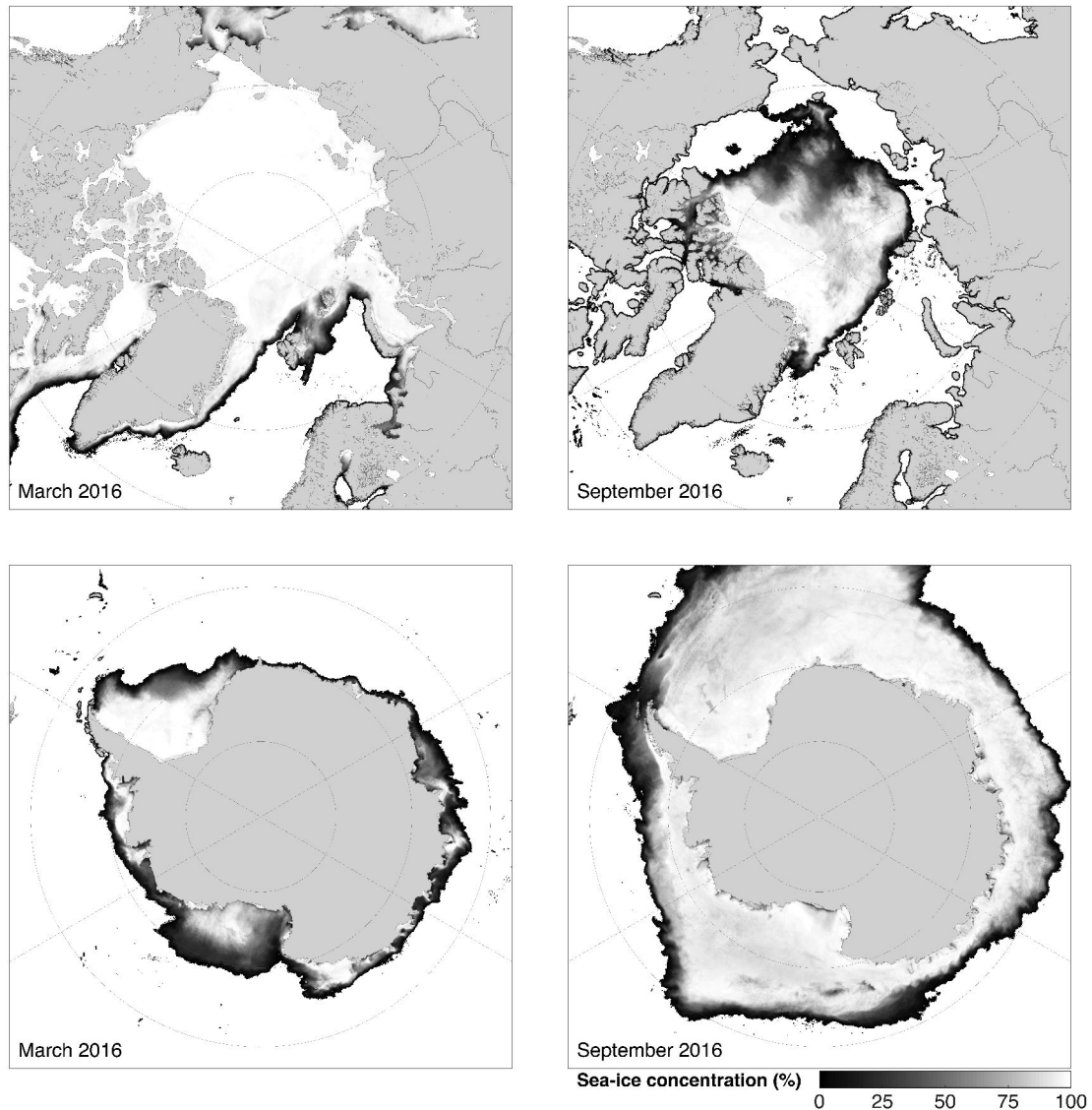


Figure 2.1: Sea-ice concentration in the northern (upper panels) and southern (lower panels) hemisphere in 2016. Plotted are monthly mean values for March and September. Sea-ice concentration data are provided by www.meereisportal.de (Spren et al., 2008).

not incorporated into the sea-ice structure and therefore released into the upper ocean. The resultant densification of the ocean surface layer leads to an unstable vertical density stratification, driving the thermohaline circulation. Melting of sea ice releases fresh water into the upper ocean, stabilizing the stratification and reducing convection (Perovich and Richter-Menge, 2009).

Due to its higher albedo, the mostly snow-covered sea ice reflects major parts of the incoming solar radiation back to the atmosphere, compared to the darker light-absorbing ocean, and plays therefore an important role in the global radiation budget (Perovich

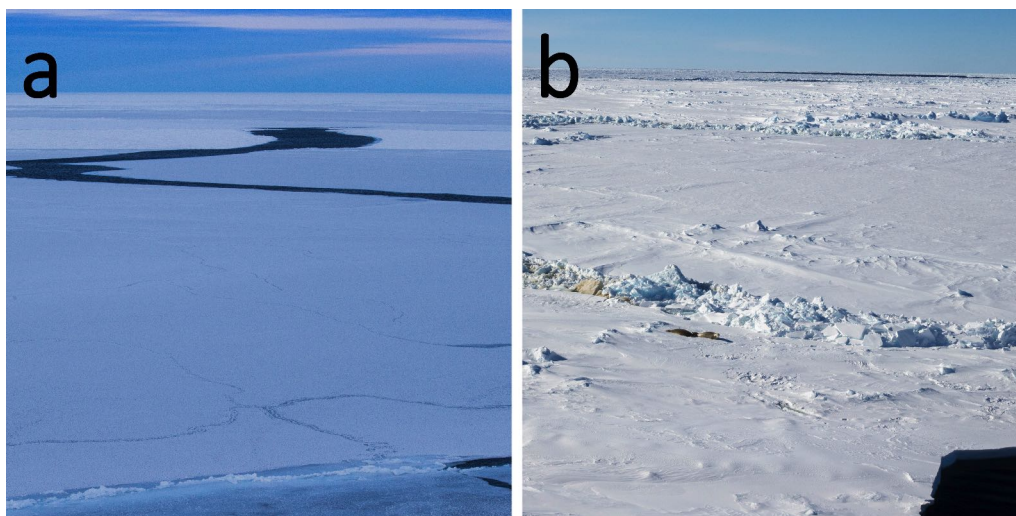


Figure 2.2: Photographs of (a) level sea ice with a distinct lead structure and (b) ridged sea ice. Photographs were taken in the northeastern Weddell Sea (2013, 2016).

and Polashenski, 2012; Perovich et al., 2011a, 2002). Moreover, the reflectivity of sea ice, and resultant ability of light penetration through snow and sea ice into the upper ocean, determines the under-ice light field (Perovich, 1996). The latter eventually accounts for warming of the upper ocean layer and subsequent bottom melt of sea ice but also controls oceanic biological activity, such as e.g. primary production (Fernandez-Mendez et al., 2015). In addition, sea ice provides a habitat for marine mammals and acts as a source of nutrients and food for several polar species (Arrigo, 2014; Thomas and Dieckmann, 2002).

Sea-ice motion is mainly driven by atmospheric forcing (Holland and Kwok, 2012; Spreen et al., 2011). Wind patterns in the lower atmosphere cause convergence and divergence of sea-ice floes contributing to changes in sea-ice extent in the Arctic and Antarctic sea-ice regions. Sea-ice divergence can result in open water areas, as e.g. leads, in which new thin ice may be formed during freezing conditions. Convergence typically leads to dynamical growth of sea ice thickness through deformation and ridging (Figure 2.2). The bounded northern sea-ice cover leads therefore to more deformed ice and reveals thicker and more perennial sea ice while in the Southern Ocean only small fractions in the western Weddell Sea and along the Antarctic coast indicate multi-year sea ice (Dieckmann and Hellmer, 2010). Thus, the resultant change in sea-ice extent and freshwater redistribution due to sea-ice drift modifies the regional pattern of heat fluxes between atmosphere and ocean, and consequently affects large-scale atmospheric circulation patterns (Overland and Wang, 2010; Stammerjohn et al., 2008).

The variety of processes related to sea ice emphasizes its importance in the Earth's climate system. As sea ice acts as a sensitive indicator for the ongoing climate change, it is important to improve our understanding on processes determining its properties, distribution and seasonality in the past, present and future (Dieckmann and Hellmer,

2010).

2.2 Snow on sea ice

The presence of snow on sea ice alters the properties of the underlying ice cover as well as associated physical and biological processes and exchanges at the interfaces between atmosphere, sea ice and ocean (Sturm and Massom, 2010). Due to its low thermal conductivity and therefore exceptional insulating properties, snow plays a key role in the thermodynamics of sea ice and thus determines its surface energy and mass budgets crucially (Massom et al., 2001; Meier et al., 2014). During winter, snow insulates the sea ice from the cold atmosphere, limiting the ice growth at the bottom (Maykut and Untersteiner, 1971). In spring and summer, snow enhances the ability of the sea-ice surface to reflect incoming shortwave radiation and determines therefore also the amount of light absorbed within and transmitted through the ice/snow column to the upper ocean layer (Perovich et al., 2011a). The higher albedo of snow-covered sea ice might also prevent extensive surface ablation and delays the timing of surface melt onset and the subsequent sea-ice reduction in spring (Sturm and Massom, 2010), known as the ice-albedo feedback (Curry et al., 1995). Thus, snow on sea ice determines also the seasonal cycle, in terms of growth and melt processes, of Arctic and Antarctic sea ice whereas the annual variations in the (snow) surface properties differ considerably between both polar regions.

2.3 Temporal evolution of surface properties of Arctic and Antarctic sea ice

Arctic sea ice is governed by a distinct seasonal cycle of surface properties (Figure 2.3a). During winter snow accumulates at the sea-ice surface (Sturm et al., 2002). Increasing temperatures in northern spring (May) lead to a decreasing snow depth and first occurrence of melt ponds at the surface (Perovich and Polashenski, 2012). The melt onset changes also the radiative budget of the surface as albedo drops from approx. 0.8 for cold and dry snow to approx. 0.5 and less (e.g. Perovich and Polashenski, 2012; Perovich et al., 2002). During the subsequent enhanced melt, snow is assumed to melt completely while the melt pond coverage increases rapidly until the end of the melt season and represents the main characteristic of Arctic summer sea ice (Perovich and Polashenski, 2012). As soon as air and surface temperatures drop below the freezing point, surface freezing commences. Hence, former melt ponds refreeze and snow accumulation begins (Perovich, 1991).

In contrast, the snowpack on Antarctic sea ice generally persists throughout the year with substantial seasonal changes in its physical properties (Figure 2.3b). The snow cover is characterized by diurnal thawing and refreezing at the snow surface and comprehensive internal melt during austral spring/summer (Eppler et al., 1992; Willmes et al., 2006).

2.3 Temporal evolution of surface properties of Arctic and Antarctic sea ice

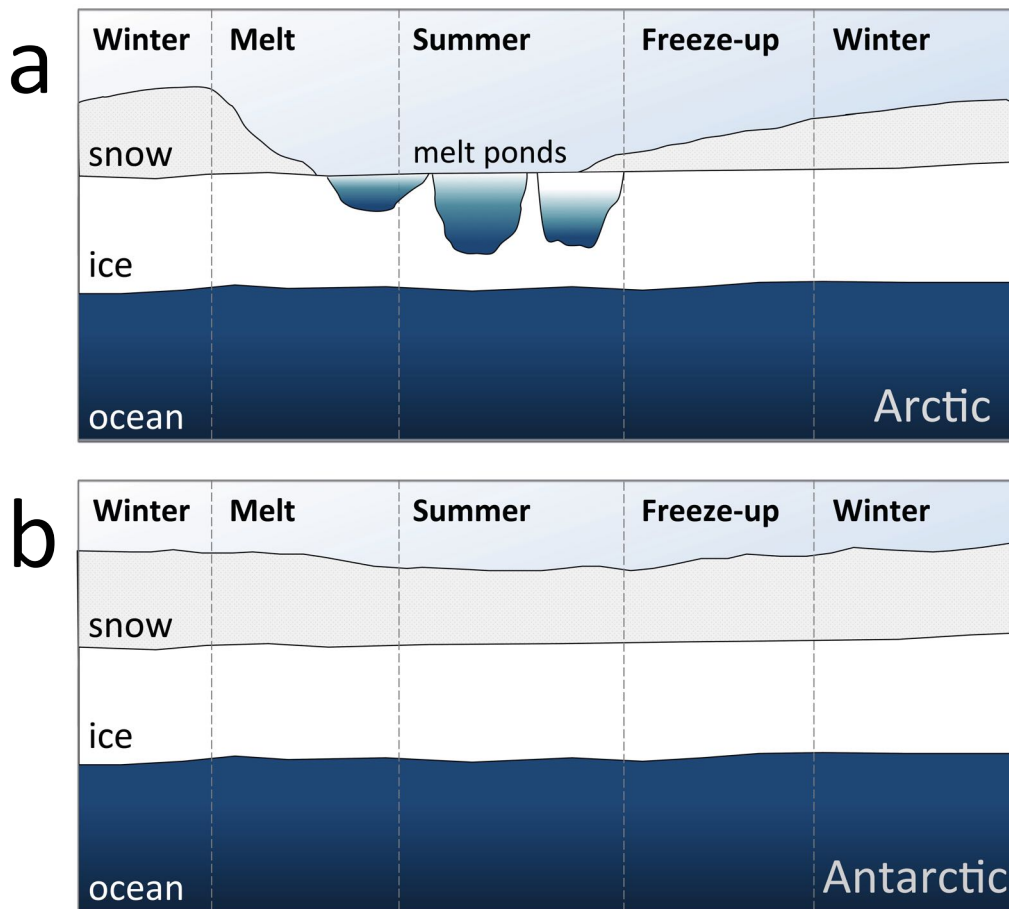


Figure 2.3: Schematic of the seasonal cycle of surface properties of (a) Arctic and (b) Antarctic sea ice.

The snowmelt water penetrates through the snowpack, and either refreezes and forms internal ice lenses and layers in the snowpack, or refreezes at the snow/ice interface when the temperature gradients within the snow and ice layer are positive (Haas et al., 2001). The subsequent frozen freshwater layer is called superimposed ice (Figure 2.4). Moreover, high snow loads on Antarctic sea ice lead to a depression of the sea-ice surface below the water level (negative freeboard) causing a widespread flooding at the snow/ice interface in the Southern Ocean (Eicken et al., 1994; Haas et al., 2001; Nicolaus et al., 2009). Refreezing of the resulting mixture of snow and saline sea water, called slush, results in snow-ice formation at the snow/ice interface (Figure 2.4). Both processes are governed by strong snow metamorphism and contribute significantly to the sea-ice growth at the surface and thus to the mass budget of Antarctic sea ice (Eicken et al., 1995, 1994; Haas et al., 2001; Jeffries et al., 1997; Nicolaus et al., 2009). Surface flooding is highly seasonally and regionally dependent. Its occurrence increases with the beginning of austral summer as basal ice melt increases due to high oceanic heat fluxes in the Southern Ocean (Martinson

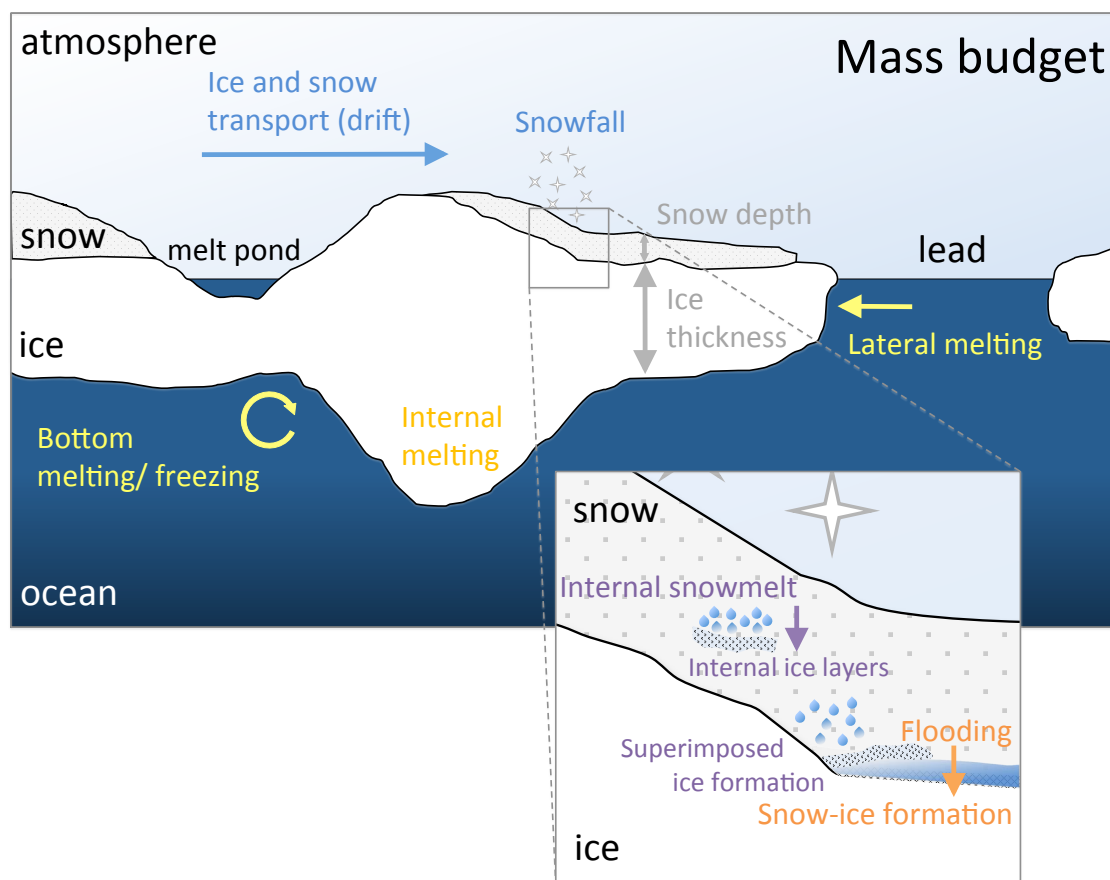


Figure 2.4: Schematic of processes modifying the mass budget of sea ice. The zoom-in resolves small-scale processes at the snow/ice interface.

and Iannuzzi, 1998) while the thick snowpack remains. Thus, we observe in the ice-covered Southern Ocean often ice-growth processes at the sea-ice surface and melt processes at the bottom, whereas the opposite is valid in the north due to a distinct seasonal cycle of surface properties and a weak Arctic oceanic heat flux (3 to 4 Wm², e.g. Huwald et al. (2005); Perovich et al. (1997)).

2.4 Ongoing changes of sea ice in both hemispheres

Sea-ice extent is the most common variable to describe the past and recent sea-ice cover in the polar regions. From satellite-based passive microwave observations it is possible to determine the sea-ice extent (defined as areal coverage with at least 15% ice coverage) for Arctic and Antarctic sea ice since 1973. During this observation period, a remarkable trend of the sea-ice extent is observed, which proceeds which evolves contrarily in in the northern and southern ice-covered oceans.

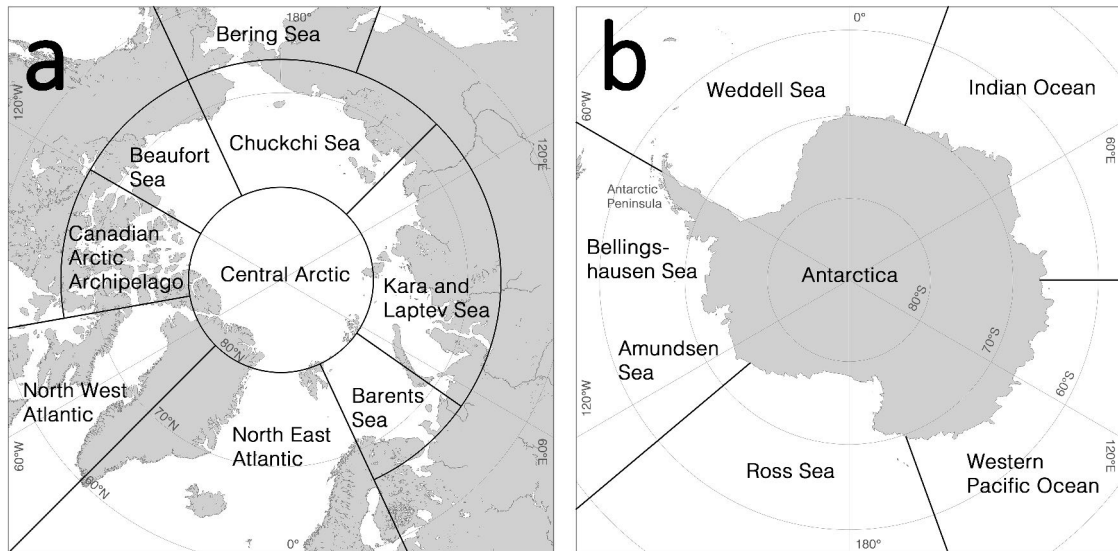


Figure 2.5: Overview of different (a) Arctic and (b) Antarctic regions as used in the thesis. Regions are based on Gloersen et al. (1992) and Overland and Wang (2007).

Arctic sea ice

Arctic sea ice reveals a declining trend in extent for all seasons since 1979 with an annual average of -4.3% per decade, based on the NASA Team sea-ice concentration algorithm (Fetterer, 2002). The largest trend is observed during the sea-ice minimum in September with values about -12.7% per decade, while trends during the sea-ice maximum (i.e. March) are smaller (-2.5% per decade) but still statistically significant at the 99% confidence level (Meier et al., 2014) (Figure 2.6a). While the sea-ice extent reached the lowest minimum value in the satellite record in September 2012 (3.41 Mio. km^2), the lowest maximum was reached in March 2016 (14.52 Mio. km^2). Nevertheless, the year-round sea-ice decline shows regional differences. Cavalieri and Parkinson (2012) reported for the period from 1979 to 2010 a decline in sea-ice extent between about 1 and 9% per decade for the Canadian Archipelago and Kara and Barents Seas, respectively, while an increase of about 2% per decade is recorded for the Bering Sea (see Figure 2.5a for definition of regions).

The overall decrease of Arctic sea-ice extent has been accompanied by a reduction in sea-ice thickness and volume during the last years (e.g. Laxon et al., 2013; Lindsay and Schweiger, 2015; Renner et al., 2014). The retrieval of an overall trend in sea-ice thickness is difficult since detailed measurements of sea-ice thickness have been lacking compared to the well-documented change in sea-ice extent: While field investigations are limited to the spatial and temporal coverage (Haas et al., 2010), satellite-based observations allow for an Arctic-wide estimate of ice thicknesses since 2003 between October and April only (e.g. Kwok and Rothrock, 2009; Ricker et al., 2014). Thus, Renner et al. (2014) reported from in-situ measurements on a sea-ice thinning at the end of the melt season in Fram Strait by

2 Sea ice - an overview

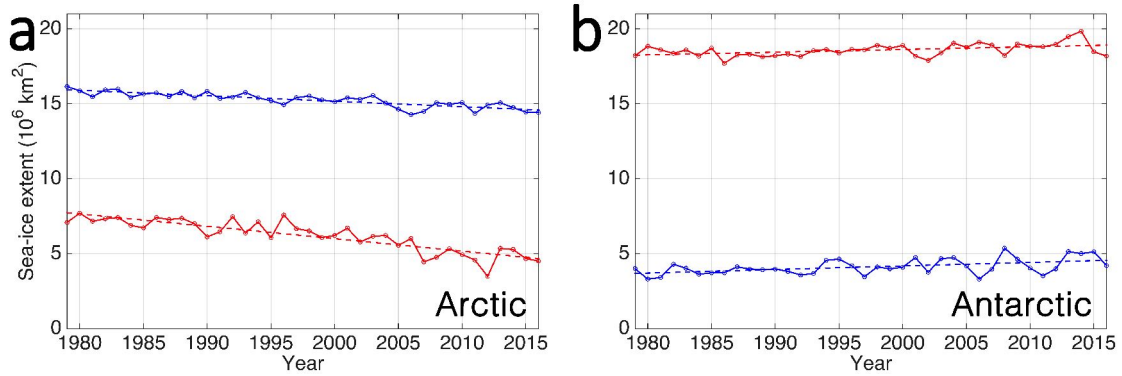


Figure 2.6: Monthly mean (a) Arctic and (b) Antarctic sea-ice extent in March (blue) and September (red) and the corresponding trend (dashed lines). Based on sea-ice concentration data provided by www.meereisportal.de (Spreen et al., 2008).

more than 50 % between 2003 and 2012. A combination of subsurface, aircraft, and satellite observations of sea-ice thickness show that the Arctic-wide ice thickness decreased by 34 % in the period 2000 to 2012, which translates to a decadal decline of about $0.58 \pm 0.07 \text{ m}$ (Lindsay and Schweiger, 2015). Considering September thicknesses only, a decline of 50 % is observed. Combining sea-ice extent and thickness indicate also a significant decline in sea-ice volume, which is about three times stronger in autumn (4291 km^3) than in winter (1479 km^3) between 2003 to 2008 and 2010 to 2012 (Laxon et al., 2013).

The decline in sea-ice thickness and volume is strongly related to a shift in sea-ice age towards a younger thinner sea-ice cover. While in the mid-1980s the multi-year ice coverage accounted for about 60 % of the total winter sea-ice extent (March), the extent dropped in 2013 to less than 30 % whereas ice older than 4 years has almost disappeared (Maslanik et al., 2011; Meier et al., 2014).

The given decrease in sea-ice extent and thickness as well as the related evolution towards a younger Arctic sea-ice cover result from a strong linkage of processes and key climate variables in the Arctic climate system. It includes increasing year-round air temperatures, leading to an earlier melt onset, whereas the expanding open water area enhances the ice-albedo feedback, increases incoming solar energy being absorbed by the ice/ocean system, and thus increases sea surface temperatures and delays the autumn freeze-up, leading to a lengthening of the Arctic-wide melt season of 5 days per decade from 1979 to 2013 (Stroeve et al., 2014, 2012).

Antarctic sea ice

In contrast to the drastic reduction of sea ice in the Arctic Ocean, the Antarctic sea-ice cover has expanded on average since 1979. The annual Antarctic-wide sea-ice extent shows a small increasing trend of about +1.5 % per decade for the period 1979 to 2013, which is dominated by the increase during the last years as the trend for the shorter time

2.4 Ongoing changes of sea ice in both hemispheres

period until 2006 was calculated as $+1.0 \mp 0.4\%$ per decade (e.g. Cavalieri and Parkinson, 2012; Parkinson and Cavalieri, 2012; Turner et al., 2014). While the Antarctic sea-ice extent reached the highest maximum value in the satellite record in September 2014 (20.14 Mio. km²), the highest minimum was recorded in the following spring with an extent of 5.51 Mio. km² (March 2015, Figure 2.6b).

Since sea-ice variability of the ice-covered Southern Ocean is significantly spatially heterogeneous, it is necessary to consider the evolution of sea-ice extent and its seasonality on a regional basis (Parkinson and Cavalieri, 2012; Stammerjohn et al., 2012; Turner et al., 2015). The Antarctic-wide positive trend in sea-ice extent is composed of regionally-opposing sea-ice changes, particularly between the Antarctic Peninsula and the adjacent Bellingshausen and Amundsen Seas, and the (western) Ross Sea (Lemke et al., 1980; Stammerjohn et al., 2012; Turner et al., 2015) (Figure 2.5b). Thus, the sea-ice extent increases, except for the sector of the Bellingshausen and Amundsen Seas, where a major decrease of $5.1 \mp 1.6\%$ per decade has occurred (Parkinson and Cavalieri, 2012). In contrast, the strongest increase in sea-ice extent has been observed in the Ross Sea with a rate of $5.2 \mp 1.4\%$ per decade (Parkinson and Cavalieri, 2012). Trends in the remaining sectors are comparable to the positive overall circumpolar trend. Thus, the overall increase in Antarctic sea-ice extent is a slight imbalance between the positive trend in East Antarctica and the contrasting trends in the western part.

The regional opposite becomes also evident from the evolution of the duration of the sea-ice (free) season in certain Antarctic regions (Massom and Stammerjohn, 2010; Stammerjohn et al., 2012). The timing of sea-ice retreat and advance governs the solar energy budget of the upper ocean and affects therefore not only physical properties, such as the sea-surface temperature and appearance of ocean upwelling (Martinson, 2012), but controls also the seasonal cycle of the associated polar marine ecosystem (Ducklow et al., 2007). During the last decades, regional patterns of changes in the seasonality are associated with the observed evolution in sea-ice extent in the Southern Ocean (Maksym et al., 2012; Stammerjohn et al., 2012). Thus, along the Antarctic Peninsula and the adjacent Bellingshausen and Amundsen Seas a pronounced prolongation of the sea-ice free season by more than three months has been observed between 1979/80 and 2010/11 (Stammerjohn et al., 2012). Again, the evolution in the (western) Ross Sea is opposed as the sea-ice free season has been shortening by two months which is consistent with the greatest sea-ice gain in the area (Stammerjohn et al., 2012).

Even though, the reasons for the overall increase in Antarctic sea-ice extent and the strong sea-ice variability are still not fully explained, the latter is suggested to be related to changes in the large-scale atmospheric circulation patterns and oceanic conditions. A comprehensive review of the changes in the atmospheric circulation patterns is given by Turner et al. (2015), which will be summarized in the following.

The dominant atmospheric system explaining the crucial differences in the evolution of sea-ice extent between the ice-covered ocean west of the Antarctic Peninsula and the

Ross Sea, is the so-called Amundsen Sea Low (ASL). The westerly wind flow around the Antarctic continent is perturbed reaching the Ross Sea region due to the irregular coastline, intensifying the atmospheric circulation in the Amundsen Sea and creates a quasi-stationary low pressure anomaly in the South Pacific (Maksym et al., 2012; Turner et al., 2013a). Persistent and stronger winds deepen the clockwise-rotating ASL system, causing stronger warm winds from the north along the eastern limb at the Antarctic Peninsula. Thus, the ice edge in the Bellingshausen Sea is pushed further south, while the ice retreat is speeded up in spring and the subsequent advance is delayed in autumn (Stammerjohn et al., 2008; Turner et al., 2014, 2016). In contrast, persistent southerly cold air outbreaks along the western limb of the low pressure system at the Ross Ice Shelf lead to a more extensive and longer-living sea-ice cover in the Ross Sea.

The region affected by the ASL is also characterized by the strongest teleconnections between the tropical Pacific to the Southern Ocean. Therefore also several atmospheric climate modes, as e.g. the Southern Ocean Annual Mode (SAM) and El Niño-Southern Oscillation (ENSO) can account for regional changes in the annual and seasonal sea-ice extent (Coggins and McDonald, 2015; Stammerjohn et al., 2008; Turner et al., 2013b, 2015; Fogt and Wovrosh, 2015). During El Niño events, cyclones move further south in the southern Atlantic and further north in the southern Pacific (Yuan, 2004), bringing colder air and simultaneously more sea ice into the western ice-covered ocean (Bellingshausen and Weddell Seas) and warmer air but less ice in the Ross Sea region (Yuan, 2004). During La Niña, the opposite occurs. Moreover, a simultaneous appearance of La Niña and SAM leads to a further deepening and southeastward track of the ASL, and therefore stronger northerly winds associated with a delayed sea-ice retreat in the Bellingshausen Sea (Maksym et al., 2012; Turner et al., 2016).

Nevertheless, the annual and seasonal variability in Antarctic sea-ice extent might not only be related to variations in atmospheric circulations patterns. Several other studies have proposed different hypotheses explaining the ongoing evolution. Thus, e.g. changes in wind stress (Lefebvre and Goosse, 2008; Liu et al., 2004; Turner and Overland, 2009) and increasing near-surface winds allow for greater surface mixing and upwelling of Circumpolar Deep Water (CDW) (Holland and Kwok, 2012; Maksym et al., 2012), while an enhanced basal melting from the Antarctic shelf leads to the formation of a relative cold and fresh surface layer which shields the ocean surface from the warmer deeper waters (Bintanja et al., 2015, 2013; Martinson, 2012). Both processes might lead to an enhanced sea-ice formation and could explain the observed overall peak in Antarctic sea-ice extent trend in autumn and early winter (Lieser et al., 2014; Turner et al., 2015).

2.5 Remote sensing of sea ice and snow

Satellite-based remote sensing is widely used to monitor geophysical variables related to the cryosphere in the northern and southern hemisphere. Satellite-derived signatures of sea

ice require a detailed understanding of interactions of sea-ice and snow surface properties with the electromagnetic radiation with respect to the satellite sensor parameters as, e.g., wavelength, polarization and incidence angle (Rees, 2005; Lubin and Massom, 2006). It is therefore useful to separate the electromagnetic spectrum into wavelength classes of similar behavior of the involved electromagnetic radiation (Chuvieco and Huete, 2009). Thus, the major components of the electromagnetic spectrum for sea-ice observations are the visual (VIS, 0.35 to 0.7 μm), the near-infrared (NIR, 0.7 to 3 μm), the thermal-infrared (TIR, 8 to 14 μm), and the microwave part (≥ 1 mm) (Lubin and Massom, 2006). While in the VIS and NIR spectrum the reflectance of the Earth's surface of the incoming solar radiation dominates over the thermal emission of the surface, the opposite is valid for the TIR spectrum. However, radiation in both, the VIS/NIR and TIR spectrum is not able to penetrate through cloud coverage. Investigations in this spectral range are therefore limited to clear-sky conditions. In contrast, the observations in the microwave spectrum are nearly independent of atmospheric conditions as with decreasing frequency the atmosphere gets more transparent. Instead, the microwave signal is mainly influenced by the emission from the surface (Rees, 2005; Lubin and Massom, 2006).

Concerning sea ice, surface emission in the microwave regime is highly dependent on the sea-ice type and the presence of snow as the snow depth, grain size and type alter the emission. Moreover, microwave observations are indirectly sensitive to the liquid water content of the surface. While liquid water is essentially opaque at microwave wavelengths, this is not the case for sea ice and snow. The difference of microwave emission from water and sea ice can be exploited to determine useful geophysical parameters, e.g., sea-ice concentration and the timing of surface melt and freeze processes (Rees, 2005; Lubin and Massom, 2006).

In general, remote sensing observations can be separated into measurements with passive and active sensor systems.

Passive microwave observations

Passive microwave sensors measure the natural emission of the surface as an equivalent brightness temperature, T_B . For microwave radiometry of sea-ice surfaces, the Rayleigh-Jeans approximation can be applied to the Planck's law assuming that atmospheric effects, as, e.g., radiation directly contributed from the atmosphere or down-welling radiation from the atmosphere, are negligible (Ulaby et al., 1986). This relates the temperature of a medium, T , linear to its emitted radiation (within the microwave regime), which can be described as the brightness temperature, T_B ,

$$T_B(f,p) = \varepsilon(f,p) \cdot T. \quad (2.1)$$

The microwave emissivity, ε , is a function of frequency, f , and polarization, p . The latter refers to the electrical field vector in the plane perpendicular to the propagation

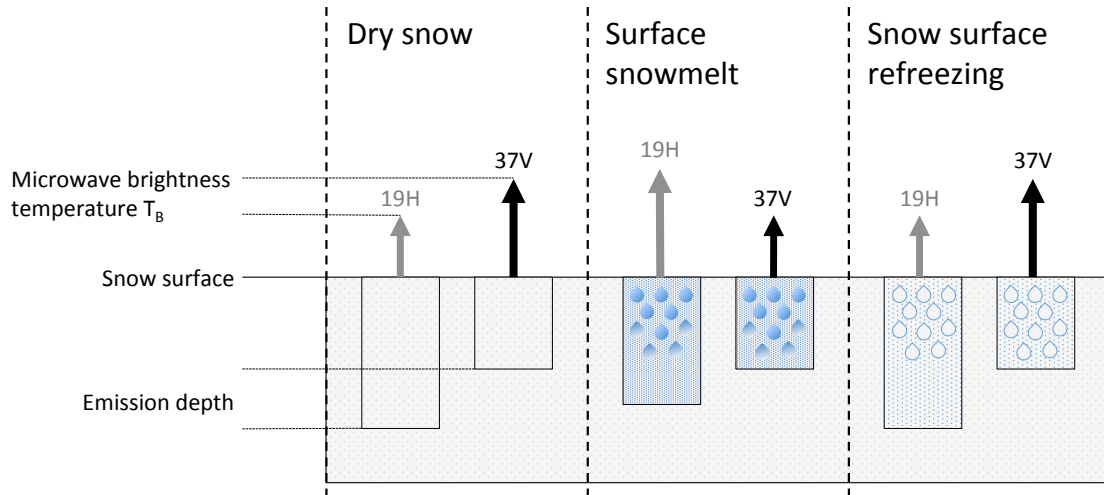


Figure 2.7: Schematic of the microwave brightness temperature and its emission depth for changing surface properties during the seasonal cycle. Differences in emission depth and associated changing brightness temperatures are shown from vertically polarized radiance at 37 GHz (37V) and horizontally polarized radiance at 19 GHz (19H). Modified after Willmes (2007).

direction of a plane electromagnetic wave and is therefore either horizontal (H) or vertical (V) (Lubin and Massom, 2006). The given concept uses the assumption of an infinite half space of the emitting material implying a depth-independent surface temperature. This concept is used throughout the thesis.

Several algorithms exploit the frequency and polarization dependency of the brightness temperature to convert the microwave signal into geophysical parameters as, e.g., sea-ice concentration and type (Comiso, 1983; Comiso et al., 1997). The most prominent wavelengths are 19 and 37 GHz. While the difference between the vertically and horizontally polarized radiances at 19 GHz allows for distinguishing between ice-covered and open-ocean areas, the discrimination between first- and multi-year ice is more dominant at 37 GHz. Recent algorithms parameterize these two characteristics to derive total and ice-type related sea-ice concentration (Cavalieri et al., 1984).

Furthermore, the time series of brightness temperature, T_B , of different frequencies and polarizations are used to determine the seasonal cycle of sea-ice surface properties as, e.g., surface melt and freeze processes (Figure 2.7). While dry snow contributes to volume scattering at frequencies higher than 30 GHz (low emission depth), it appears almost transparent to microwave frequencies below approximately 30 GHz (high emission depth). When snow starts to melt, the liquid water content increases and thus surface scattering becomes dominant (Mätzler and Hüppi, 1989). Since surface scattering is weaker compared to volume scattering, the emissivity of the wet snowpack increases while the emission depth decreases (Abdalati and Steffen, 1997; Tedesco, 2015; Ulaby et al., 1986). The as-

sociated increase in the brightness temperature is more pronounced at the horizontal than vertical polarization (Abdalati and Steffen, 1995). This polarization difference diminishes with increasing snow wetness due to changes in the dielectric properties at the air/snow interface. Moist snow affects the brightness temperature at all frequencies as well as its emission depth.

In Section 4 (Arndt et al., 2016), the sensitive behavior of microwave signatures to the seasonal cycle of surface properties is used to determine the timing of dominant (snow) surface melt processes on Antarctic sea ice.

Active microwave observations

Active microwave sensors transmit a microwave signal and measure the backscattered signal determined by the scattering properties of the illuminated surface area (Rees, 2005; Lubin and Massom, 2006). The normalized measure of the backscatter from the surface area is given by the radar backscatter coefficient, σ^0 . According to Lubin and Massom (2006), it is defined as the ratio of scattered power relative to isotropic scattering targets and a calibrated estimate of the return power of a radar pulse at the satellite. The microwave emission and backscatter behavior of sea ice and its snow cover is determined by four parameters (Lubin and Massom, 2006; Onstott and Shuchman, 2004):

- a. the surface roughness;
- b. the orientation of the sea-ice and snow surface features relative to the radar azimuth look and incident angle;
- c. the complex dielectric constant (or complex permittivity) of sea ice and snow; and
- d. the presence of dielectric discontinuities or discrete scatter as, e.g., air bubbles.

Surface roughness alters the intensity of the backscatter response from sea ice. It is a measure of the irregularity of a target area in both vertical and horizontal direction compared to the radar wavelength (Onstott and Shuchman, 2004). Rough surfaces, e.g., in the case of ridged sea ice, tend to reflect a significant fraction of the incident microwave energy in the direction of the illumination. In contrast, smooth surfaces, e.g., in the case of undeformed young sea ice or calm open water, tend to reflect a significant fraction of the incident microwave energy away from the direction of the incoming radiation. The specular behavior of the smooth surface leads to relatively low backscatter response compared to the rough surface acting as a diffuse reflector with a high backscatter response (Lubin and Massom, 2006).

The complex permittivity, ϵ , is the quantity with the major influence on the interaction of microwave radiation with snow-covered sea ice (Shokr, 1998; Ulaby et al., 1986). It describes the electric properties of a medium and its resultant electromagnetic wave

propagation, scattering, reflection and attenuation, and is defined as (Lubin and Massom, 2006; Onstott and Shuchman, 2004)

$$\epsilon = \epsilon' - j\epsilon'' \tag{2.2}$$

with $j = \sqrt{-1}$. The real part, ϵ' , is referred to as the dielectric constant or the permittivity, which determines the proportion of energy that penetrates the medium. It is therefore proportional to the degree of scattering by the medium. The imaginary part, ϵ'' , is referred to as the dielectric loss factor governing the wavelength-dependent penetration depth into the sea-ice and snow layer. The energy loss from the dielectric interface through the medium is wavelength- and temperature-dependent (Lubin and Massom, 2006; Onstott and Shuchman, 2004; Hallikainen and Winebrenner, 1992).

Sea ice and snow are considered to be a three-phase medium comprising pure ice, air, and liquid brine (Weeks and Ackley, 1986). Thus, the volumetric fraction of the present liquid water content and the incorporated impurities dominate the bulk permittivity and therefore the received backscatter signal of sea ice and snow. The sensitive response of the backscatter signal to physical properties of the sea ice and its snow cover is widely exploited to monitor dominant characteristics of sea ice in the northern and southern hemisphere. Arctic first-year ice is characterized by a smooth surface and a large number of brine inclusions. The resultant high dielectric loss, despite of the high permittivity, results in surface scattering (low penetration depth) being the predominant scattering mechanism of the received backscatter signal at the C-Band (4 to 8 GHz) (Lubin and Massom, 2006). In contrast, the low salinity of Arctic multi-year ice leads to an higher permittivity and thus a lower dielectric constant. The additional weaker dielectric loss in the perennial sea-ice cover promotes deep penetration of microwave energy into the snow and ice. Hence, the incoming microwave radiation interacts with dielectric discontinuities and discrete scatters as, e.g. large incorporated air bubbles. The resultant strong volume scattering from multiple scattering in the medium leads to a high backscatter response (Lubin and Massom, 2006; Onstott and Shuchman, 2004).

However, the interpretation of the backscatter signal over Antarctic sea ice is not comparable to the northern hemisphere. The year-round snow cover and the subsequent widespread flooding of Antarctic multi-year ice (Section 2.3) leads to generally equivalent backscatter interactions compared to those of Arctic first year ice. In contrast, Antarctic first-year might have an initially higher backscatter response due to its characteristic surface ridging, irregular floe edges and snow crystals on top (Sandven et al., 2006).

In addition, the seasonal cycle of the radar backscatter signature can be utilized to monitor temporal variations in the surface, i.e. surface melt and freeze. While the former is indicated by a sudden increase (decrease) in Arctic first-year (multi-year) sea-ice backscatter signal, the latter is shown by a slow return of the backscatter signal to winter values (Barber et al., 1995, 1998; Mortin et al., 2012, 2014; Winebrenner et al., 1998).

However, the opposing backscatter signal of Antarctic multi-year ice compared to Arctic sea ice is also reflected in its seasonal cycle due to the dominant appearance of superimposed ice and flooding at the snow/ice interface during the spring transition (Haas (2001), Section 2.3). As a continuation of the work by Haas (2001), Chapter 5 discusses how the seasonal cycle of backscatter signatures over perennial Antarctic sea ice can be related to the seasonal snowmelt processes in the lower snowpack.

3

The impact of Arctic sea ice surface melt on transmitted heat fluxes

Sea ice plays an important role in the global climate system. Arctic sea ice has not only decreased in volume during the last decades, but has also changed its physical properties towards a thinner and more seasonal ice cover. These changes do not only strongly impact the energy budget and thus the partitioning of solar radiation between atmosphere, sea ice, and ocean, but also affect the sea-ice mass balance as well as the ice-associated ecosystem. These changes have been quantified in several studies for certain regions and/or seasons of the year (e.g. Hudson et al., 2013; Nicolaus et al., 2012).

In this chapter, the focus is put on on the quantification of large-scale, multi-seasonal, and inter-annual changes in the energy budget of Arctic sea ice due the ongoing changes in the prevalent sea-ice conditions. Doing so, solar shortwave fluxes through sea ice were estimated for the entire Arctic Ocean during all seasons. To address this topic, a new parameterization of light transmittance through sea ice was developed for all seasons of the year as a function of variable sea-ice properties. The combination with satellite-derived time series observations, as sea-ice concentration and type, melt pond coverage and surface melt and freeze-onset, as well as re-analysis data on solar surface radiation, allows for the quantification of solar short-wave radiation fluxes through Arctic sea ice and associated potential sea-ice bottom melt rates for the entire seasonal cycle from 1979 to 2011. The results enable to identify crucial surface properties and processes controlling the energy budget of Arctic sea ice.

This chapter is in large parts identical to the content published in Arndt and Nicolaus (2014), while Section 3.5.5 is a summary of the content published in Katlein et al. (2015). To emphasize the importance of optical properties and the associated impact on the surface energy balance for the energy and mass budgets of Arctic sea, an extension of the theoretical background is an additional contribution for this chapter.

3.1 Introduction

The evolution of Arctic sea ice towards a thinner, younger, and more seasonal sea-ice cover during the last few decades (e.g. Comiso, 2012; Haas et al., 2008; Maslanik et al., 2011, 2007) has a strong impact on the partitioning of solar energy between the atmosphere,

3 *The impact of Arctic sea ice surface melt on transmitted heat fluxes*

sea ice, and ocean (e.g. Perovich et al., 2011a, 2007a; Wang et al., 2014). Decreased surface albedo (Perovich et al., 2011a), earlier melt onset, and a longer melt season (Markus et al., 2009, updated) have contributed to the observed increases in sea ice and snow melt (Perovich and Richter-Menge, 2009), and higher absorption and transmission of solar irradiance within and through Arctic sea ice (Nicolaus et al., 2012; Stroeve et al., 2014). Beyond the physical consequences of the observed changes, strong impacts on ecological interactions and biogeochemical processes are expected, such as changes in habitat conditions for ice-associated organisms or changes in primary production (Arrigo et al., 2012; Deal et al., 2011; Popova et al., 2012).

Various studies have shown the immediate link between sea-ice energy and mass balance, as well as the impact of energy fluxes on the physical properties of sea ice (Grenfell et al., 2006; Light et al., 2008; Perovich and Richter-Menge, 2009). These heat fluxes are composed of short-wave, long-wave, conductive, and turbulent fluxes at the interfaces of sea ice with the atmosphere and the ocean. Beyond these energy budget approaches, sea-ice mass balance may also be derived from direct comparisons of sea-ice growth during winter, and surface and bottom melt during summer (Perovich et al., 2011b).

From studies on the interaction of sunlight and sea ice, it has been possible to improve our understanding of the effects of snow cover (Perovich et al., 2007b), melt ponds (Rösel and Kaleschke, 2012; Schröder et al., 2014), and biological interactions (Arrigo et al., 2012; Mundy et al., 2007, 2005). In addition, the spatial variability (Perovich et al., 2011a) and seasonal changes (Nicolaus et al., 2010a; Perovich and Polashenski, 2012; Perovich et al., 2002) in the optical properties of sea ice and snow have been studied by different methods. However, previous studies have not quantified large-scale, multi-seasonal, and inter-annual changes, because these studies were limited to different regions and/or seasons of the year. In addition, these studies have described measurements on different ice types, which also differ in their optical properties as a result of their growth history (Perovich and Polashenski, 2012). One possible approach obtaining such generalized studies on the in- and under-ice energy budgets in sea-ice-covered oceans would be to use a radiative transfer model in combination with surface energy budgets, as implemented by Perovich et al. (2011a). However, such a model would require adequate knowledge about the distribution of snow and sea ice (as forcing data) to derive the optical properties of sea ice and snow as a function of space and time. This type of information is not available yet, in particular not for timescales on the order of decades. An alternative approach is to use existing remote sensing and re-analysis data together with a parameterization of light transmittance through sea ice. This method was developed by Nicolaus et al. (2013, 2012) to calculate Arctic-wide radiation fluxes through sea ice. However, these studies were restricted to 1 month (August 2011) when comprehensive in situ measurements are available from the trans-polar cruise of German research vessel *Polarstern*.

In order to improve the understanding of the ongoing change in sea-ice conditions and the associated impact on the partitioning of solar energy, we provide an estimate of the

monthly shortwave radiative transfer through sea ice for the entire Arctic Ocean for the period 1979 to 2011. To emphasize the changing physical properties of the Arctic sea-ice cover, our estimates include fluxes through sea ice only. Therefore, we use a definition of 6 types of sea ice over the annual cycle, define 6 distinct time periods of insolation conditions, and include the temporal and spatial variability of melt ponds to extend and generalize the upscaling method of Nicolaus et al. (2013, 2012). In order to investigate the reliability of the method and to obtain a measure of uncertainty, we perform sensitivity studies by comparing the calculated fluxes to in situ observations obtained from the Transpolar Drift, between 86.5 and 88.5° N, during the drift study of the schooner Tara from April to September 2007 (Nicolaus et al., 2010a). Finally, it was possible to estimate transmitted heat fluxes through sea ice and to derive trends for the entire Arctic basin for the period of 1979 to 2011. Since this study focuses on the variability of sea-ice properties, changes in sea-ice concentrations are not considered.

3.2 Theoretical background

3.2.1 Optical properties of sea ice

Optical properties of sea ice and snow are related to their physical structure and state in the spectral range of roughly 250 to 2500 nm (Perovich, 1996, 2001). They contribute to the understanding of physical-optical interactions and its impact on a temporal and spatial scale, including the ice-albedo feedback mechanism (Perovich and Richter-Menge, 2009), thermodynamic associations and biological processes as the impact of ultraviolet radiation on ice algal production (Mundy et al., 2005; Perovich, 1996). Changing optical properties do also effect satellite-based observations of the snow cover and properties of the underlying sea ice. Optical properties of sea ice are distinguished into inherent and apparent material properties. Inherent optical properties describe the radiative transfer in sea ice and snow at optical wavelengths, governed by two processes: scattering and absorption (Perovich, 1996, 2001) (Figure 3.1).

Scattering refers to the multiple deflection of radiation or energy from its normal pathway due to interactions with the matter. It is characterized by the scattering coefficient and a phase function. While the scattering coefficient is a measure of scattering and describes the subsequent energy dissipation, the phase function describes the angular redistribution of scattered light (Sturm and Massom, 2010).

Absorption describes the loss of energy and light as it propagates through an absorbing medium. It is a measure of the ability of a matter to absorb incident radiation, which is quantified per unit length by the absorption coefficient (Sturm and Massom, 2010). While absorption of sea ice and snow is strongly wavelength dependent and increases with increasing wavelength, scattering is assumed to be independent of wavelength since scattering inclusions, as air bubbles, brine pockets or solid impurities, are significantly

3 The impact of Arctic sea ice surface melt on transmitted heat fluxes

larger than the wavelength (Perovich, 1996, 1990). Therefore, scattering is affecting the magnitude whereas absorption entails the spectral distribution of the incident radiation. Combining scattering and absorption of light penetrating from the air/snow- or air/ice interface to the ice/ocean interface is referred to light attenuation, which is characterized by the *extinction coefficient* (Perovich, 1996).

The described inherent (microscopic) properties result in apparent (macroscopic) optical properties describing the radiation and energy flux as well as the morphology in and under sea ice. Albedo and light transmittance are referred as apparent optical properties and are well studied during the last decades (Hudson et al., 2013; Nicolaus et al., 2012, 2010b,a; Perovich and Polashenski, 2012; Perovich et al., 2011a; Perovich, 1996).

Albedo is defined as the fraction of incident solar radiation that is reflected from the respective medium. It is dependent on both the wavelength and prevalent surface conditions. The latter leads to variations in the total albedo of Arctic sea ice from 0.06 for open water, 0.15 to 0.4 for ponded ice, to 0.77 to 0.87 for snow-covered sea ice (Perovich, 1996).

Light transmission through sea ice is defined analogously to the albedo as the fraction of the incident irradiance that is transmitted through the ice (Perovich, 1990). It is also dependent on both, wavelength and surface conditions, and additionally on the physical composition of the ice and its snow cover as well as on the sea-ice thickness and snow depth.

All over, the snow cover plays a crucial role in the partitioning of solar radiation in the atmosphere-ice-ocean system. It doubles the albedo compared to bare sea ice (Grenfell and Maykut, 1977), while its (spectral) extinction coefficient are more than a magnitude larger than those for sea ice (Waren, 1982).

3.2.2 Surface energy budget of sea ice

The climate system components, named atmosphere, ice and sea ice, interact directly but also indirectly with each other by means of radiative transfer of energy. Figure 3.1 gives an overview on the important heat fluxes for the surface heat budget of sea ice.

The surface heat budget of sea ice is composed in general of radiative, turbulent, and conductive fluxes (Perovich et al., 2011b). Its balance at the air/ice- or air/snow interface determines the rate of surface sea-ice melt. In contrast, the energy balance at the ice/water interface describes the ice growth.

The surface energy budget is dominated by the *radiative fluxes* composed of solar shortwave radiation (spectral range of measured values in this thesis: 250 to 2500 Wm²) and longwave radiation. The amount of shortwave and longwave radiation reaching the surface is influenced by scattering, reflection, absorption, and emission at the cloud cover. Depending on the type and altitude of the clouds, the consequent decrease in shortwave and increase in longwave radiation gets more or less dominant. Thus, low clouds have a warm-

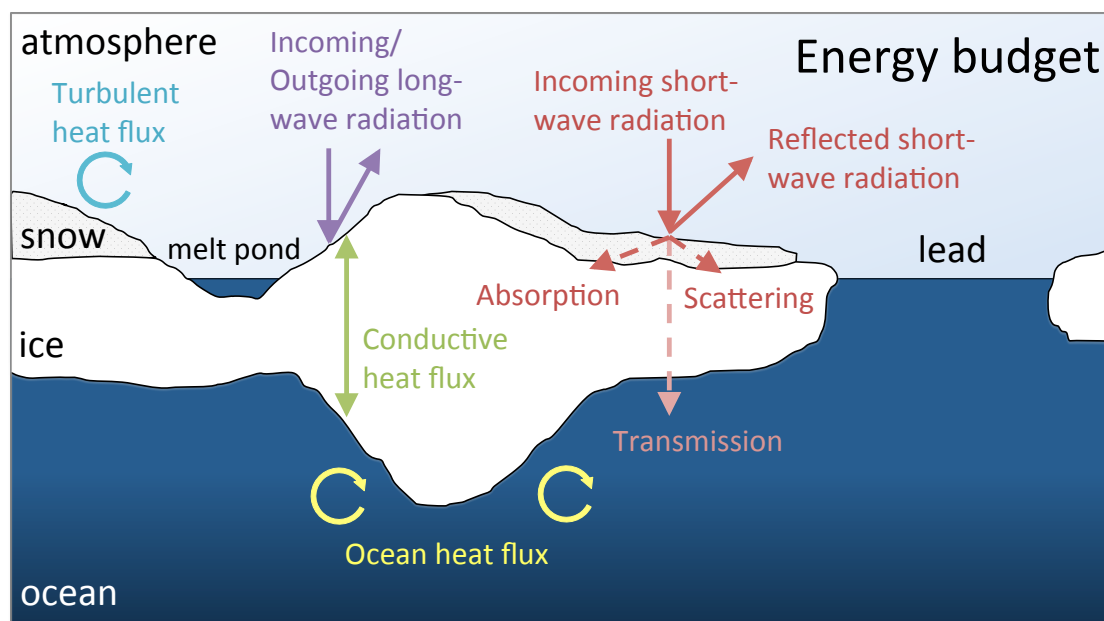


Figure 3.1: Schematic of the surface energy budget of sea ice.

ing effect whereas high clouds tend to cool the surface (Sedlar et al., 2011). In contrast, outgoing shortwave radiation is mostly affected by the surface albedo whereas outgoing longwave radiation is a function of surface temperature (Perovich and Richter-Menge, 2009).

Turbulent fluxes involve sensible and latent heat fluxes. They depend both on different atmospheric parameters as wind speed and air temperature. Moreover, sensible heat fluxes are associated with temperature differences between the air and underlying snow/ice interface whereas latent heat fluxes are associated with evaporation and sublimation over the ocean and snow/ice surface, respectively (Parkinson and Washington, 1979).

The *conductive heat flux* through the bulk of snow and ice is created by the difference between the colder air mass and the warmer upper ocean (Shokr and Sinha, 2015). It is therefore approximately proportional to the inverse of the ice thickness. Considering all mentioned heat fluxes and in addition the oceanic heat flux from the (warmer) ocean to the (colder) ice bottom, the resulting energy budget between atmosphere and ocean contributes to the mass budget of sea ice, which is described in detail in Section 2.

3.3 Method

Solar short-wave radiation fluxes (250 to 2500 nm, here also referred to as “light”) through sea ice are calculated daily, from 1 January 1979 to 31 December 2011, for the entire Arctic Ocean (north of 65° N). Building on the method and parameterization by Nicolaus et al.

3 The impact of Arctic sea ice surface melt on transmitted heat fluxes

(2013, 2012), which were limited to the snow-free summer season in 2011 without any seasonal cycle of surface properties, the parameterization of light transmittance through sea ice has been extended for all seasons. Thus, transmittance is now estimated as a function of surface (snow) melt/freeze state and melt pond concentration, in addition to the previous (only) sea-ice age dependence. The new parameterization was driven by satellite observations of daily sea-ice concentration and surface solar irradiance to calculate fluxes as performed in Nicolaus et al. (2013, 2012). All data sets are interpolated to a 10 km polar stereographic grid, using nearest-neighbor resampling. Although daily fluxes are calculated and available, only monthly means are shown and used to discuss the findings, because the main focus of this extended study is on seasonal changes and long-term trends.

For the main analyses, we exclude open water areas, as those would clearly dominate the transmitted heat flux signal (Perovich et al., 2007a). Therefore, we consider only fluxes through ice-covered areas, as these are crucial for the energy and mass balance of sea ice as well as for biological processes beneath the ice cover. The solar heat input to the open ocean also has an important impact on the ice–ocean system, but is a basic function of sea-ice concentration.

3.3.1 Solar heat flux equations

Solar heat input through sea ice into the ocean ($E_T(t, x, y)$) is calculated as the product of the downward solar radiation (E_d), the sea-ice concentration (C_i), and the total transmittance of pond-covered sea ice (τ_i) for each grid cell and each day, over the period 1 January 1979 to 31 December 1999:

$$E_T(t, x, y) = E_d(t, x, y) \cdot C_i(t, x, y) \cdot \tau_i, \quad (3.1)$$

with time (t) and position (x, y).

Since 1 January 2000, when satellite-derived melt-pond concentrations are available, the solar heat input through sea ice into the ocean (E_T) has been calculated as the sum of fluxes through bare ice (E_B) and melt ponds (E_P):

$$\begin{aligned} E_T(t, x, y) &= E_B(t, x, y) + E_P(t, x, y) \\ E_T(t, x, y) &= E_d(t, x, y) \cdot C_i(t, x, y) \cdot [1 - C_p(t, x, y)] \\ &\quad \cdot \tau_b(t, x, y) + E_d(t, x, y) \cdot C_i(t, x, y) \\ &\quad \cdot C_p(t, x, y) \cdot \tau_p(t, x, y), \end{aligned} \quad (3.2)$$

with the transmitted solar radiation at the bottom of the ice E_T , downward solar radiation E_d , sea-ice concentration C_i , melt pond fraction C_p , transmittance of bare sea ice τ_b , transmittance of melt ponds τ_p , time t , and grid cell (x, y).

To obtain the total solar heat input per unit area for a certain time period ($Q_T(x, y)$),

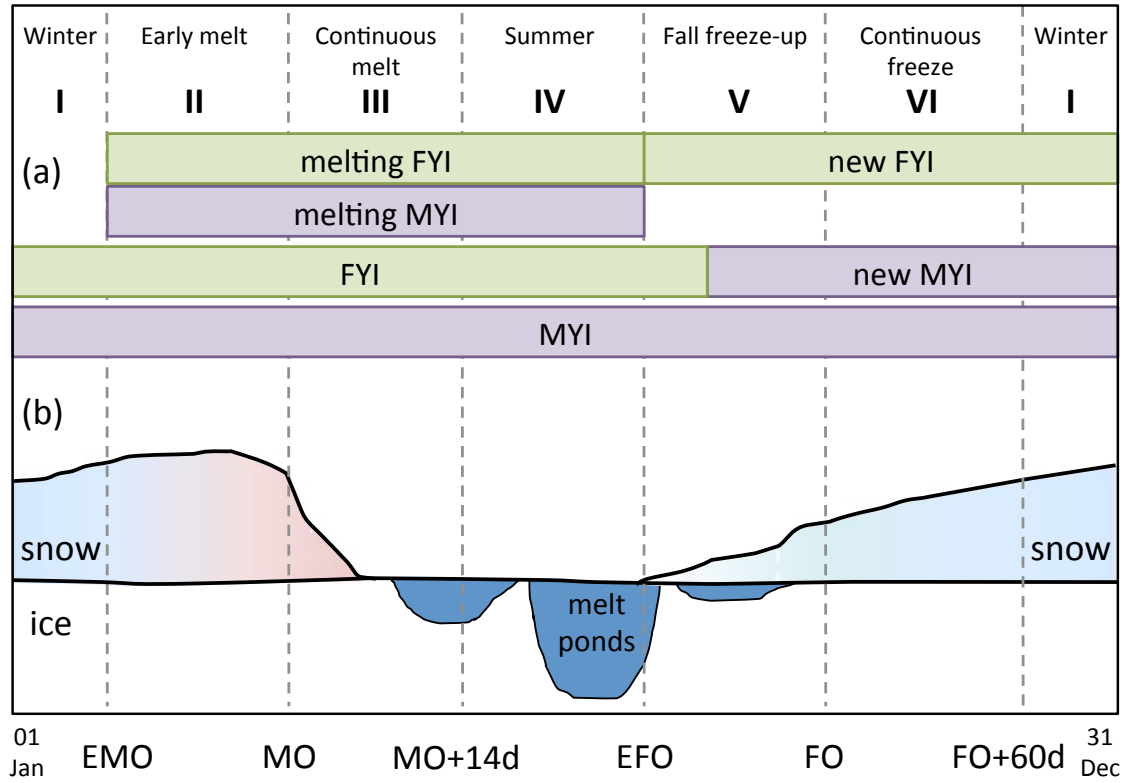


Figure 3.2: Classification of sea ice (a) types and (b) surface properties as used in this study. The timing of each phase results from the status of the sea ice. Depending on the season, different sea-ice types co-exist. Abbreviations: FYI: first-year ice; MYI: multi-year ice; EMO: early melt onset; MO: melt onset; EFO: early freeze onset; FO: freeze onset.

the heat flux is calculated for each grid cell and then integrated over the given time (Δt):

$$Q_T(x, y) = \sum E_T(t, x, y) \Delta t. \quad (3.3)$$

Spatial integration over the entire Arctic Ocean (north of 65°N) reveals the Arctic-wide total solar heat input Q_T .

Assuming sea ice is at its melting point, has a density ρ_{ice} of 917 kg m^{-3} , and has a latent heat of fusion L_{ice} of 0.3335 J kg^{-1} , and that there are no changes in long-wave, latent, and conductive heat fluxes, $Q_T(x, y)$ can be converted into a sea ice melt rate m_{eq} :

$$m_{\text{eq}} = \frac{Q_T(x, y)}{L_{\text{melt}} \cdot \rho_{\text{ice}}}. \quad (3.4)$$

3.3.2 Seasonality of surface properties and transmittance of Arctic sea ice

To calculate solar heat fluxes under Arctic sea ice for an entire year, the main challenge is to parameterize the seasonal evolution of $\tau_b(t, x, y)$. This is mainly achieved by merging the sea-ice age information (Maslanik et al., 2011, 2007) with the melt/freeze status (Markus et al., 2009, updated) into six surface types.

Definition of sea-ice types

Figure 3.2 shows the annual cycle of these six sea-ice classes together with surface properties of Arctic sea ice. These classes are introduced to avoid abrupt changes in the optical properties during the transition from spring to summer as well as from summer to fall. After early melt onset (EMO), *melting FYI* and *melting MYI* are introduced for sea ice completely melting during the summer melt. Therefore, it is necessary to classify each cell as either becoming ice free (sea-ice concentration of less than 15 %) or not. To do this, the ice concentration of each pixel is evaluated for all days until EFO. If the pixel becomes ice free, the last day of melting is stored for later calculations. According to Maslanik et al. (2011, 2007), *FYI* surviving the summer melt turns into *MYI* after week 36 of the year. As the immediate change in ice age tagging is not associated with an immediate change in sea-ice properties, we include an additional class of *new MYI* that turns into *MYI* at the end of the year. When sea-ice concentration reaches a value greater than 15 %, the pixel is classified as *new FYI*.

In the following, sea ice consisting of both bare sea ice and melt ponds is called pond-covered sea ice.

Transmittance of pond-covered sea ice

The seasonal evolution of surface properties and the transmittance of Arctic sea ice is divided into six different phases (note that there are both different ice types and different seasonal phases). The timing of these phases is based on the melt and freeze onset data established by Markus et al. (2009, updated). Our parameterization of seasonal variations in light transmittance considers the transmission through both sea ice and snow, and is mostly based on the results of two field campaigns that focused on the understanding of ice–ocean–atmosphere processes that control the partitioning of solar radiation between reflection, absorption, and transmittance: the Surface Heat Budget of the Arctic Ocean (SHEBA) experiment from 1997 to 1998 (Perovich, 2005), and measurements conducted on MYI within the Transpolar Drift, between 86.5 and 88.5° N, during the drift study of the schooner Tara from April to September 2007 (Nicolaus et al., 2010a). In addition, analyses from previous observations by Nicolaus et al. (2010b); Perovich et al. (1998); Perovich (1996) are used. Figure 3.3a shows the seasonal total transmittance of pond-covered sea ice (τ_i) for constant pond concentrations of 26 (FYI) and 29 % (MYI), respectively, used

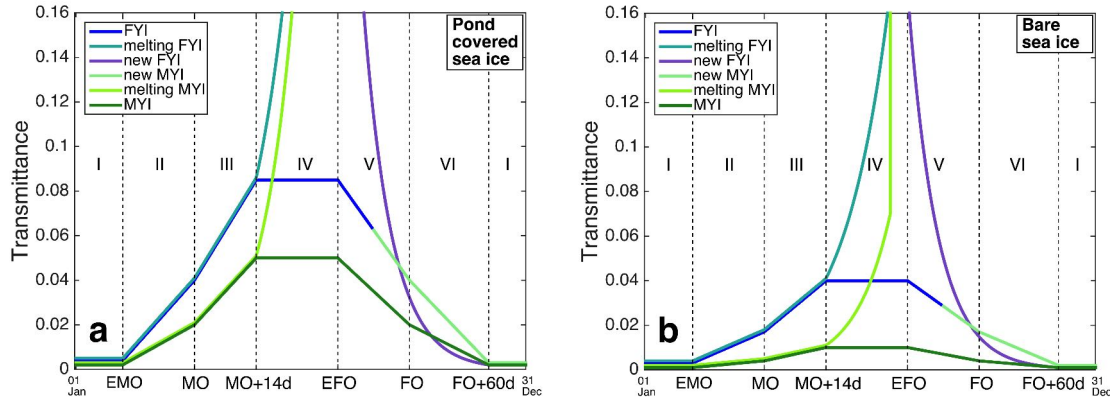


Figure 3.3: (a) Total transmittance of sea ice during each phase (see Figure 3.2). In this figure, melt pond concentrations of 26 % are assumed for first-year ice (FYI) and 29 % are assumed for multi-year ice (MYI). (b) Transmittance of bare ice during each phase (see Figure 3.2). Transmittance values for single ice classes are given in Table 3.1. The illustrated evolution of transmittance values is based on analyses from previous field campaigns and observations. Abbreviations: see Figure 3.2.

for the period 1979 to 2000, during which time there are no available satellite melt pond coverage observations. This combination of a given mixture of ponds and bare ice was used to develop the seasonal cycle of transmittance, as described in the next paragraphs. All transmittance values for the different phases are compiled in Table 3.1.

Phase I: winter (from FO + 60 days to EMO) Winter conditions are characterized by snow-covered sea ice without melt ponds. The snow cover is assumed to be cold, dry and optically thick, which means the snow determines the optical properties. Thus, radiative fluxes through sea ice are small. The best available transmittance observations for such conditions are those measured during the first days of the Tara drift, although it was already early April. Hence, transmittance was accordingly set to 0.002 (Nicolaus et al., 2012).

Phase II: early melt (from EMO to MO) EMO denotes the first significant change in optical properties. Snow depth decreases, and surface and sea-ice temperatures increase. Consequently, the snow becomes wet and is no longer optically thick. This phase also corresponds to formation of the first melt ponds. Here we assume a linear increase in τ_1 until MO.

Nicolaus et al. (2012) calculated a transmittance of 0.02 for MYI for the day of MO. Furthermore, Perovich and Polashenski (2012) reveal that the surface albedo of FYI is about half that of MYI at the same time. Adapting this albedo evolution to the transmittance, the transmittance of FYI is assumed to be 0.04 at MO.

3 *The impact of Arctic sea ice surface melt on transmitted heat fluxes*

Melting FYI and melting MYI After EMO, the continued melt of snow and sea ice strongly impacts light transmittance. Starting with the summer phase (Phase IV), we assume that the optical properties of melting sea ice differ from sea ice surviving the summer melt. In addition, differences between melting FYI and melting MYI are expected. Therefore, melting FYI and melting MYI are separated in the parameterization of τ_1 .

In order to describe these classes, laboratory studies by Perovich (1996) on the evolution of albedo during the initial ice growth phase were applied to the evolution of transmittance, assuming an inverse behavior of transmittance and albedo. Therefore, the increase in transmittance of seasonal sea ice can be described as roughly exponential (Perovich, 1996). Assuming the transition of transmittance from melting sea ice to the open ocean is the inverse of the albedo transition (Perovich, 1996), we use a transmittance of 0.4 for the last remaining sea ice. Thus, an exponential increase between the first and last day of melting for the corresponding pixel is fitted, and the maximum transmittance of sea ice is expected to be 0.4.

Phase III: continuous melt (from MO to MO + 14 days) After MO, snow is assumed to melt completely within 14 days (Nicolaus et al., 2006; Perovich et al., 2002), and pond cover fraction increases rapidly until the maximum pond cover is reached at the end of this phase (Nicolaus et al., 2010a). The transmittance continues to increase linearly until the beginning of summer (MO + 14 days).

Phase IV: summer (from MO + 14 days to EFO) During this phase, the sea-ice surface is characterized by strong sea-ice melt and culminates in the minimum ice concentration of each pixel. The surface is a mixture of bare ice and melt ponds with a constantly renewing surface scattering layer (Barber et al., 1998; Perovich et al., 2002). This implies small changes in the optical properties and light transmittance of the ice over time during Phase IV. Hence, τ_1 is assumed to be constant for sea ice that survives summer melt. Based on observed transmittance values of solar radiation through FYI and MYI during TransArc 2011 (Nicolaus et al., 2012), we use summer transmittance values of 0.04 for bare FYI, 0.01 for bare MYI, 0.22 for melt ponds on FYI, and 0.15 for melt ponds on MYI. These values are weighted according to melt pond fractions (Rösel and Kaleschke, 2012).

Phase V: fall freeze-up (from EFO to FO) Air and surface temperatures drop below 0°C, resulting in the initial occurrence of surface freezing. Subsequently, snow accumulation can begin and former melt ponds refreeze, but can still be recognized through the new snow cover. Thus, the transmittance is decreasing rapidly. Similar to Phase III, the transmittance of FYI decreases to 0.04 and, for MYI, to 0.02 until FO. Additionally, sea ice that survives the summer melt is promoted to 1-year older ice in weeks 36–37 according to Maslanik et al. (2007), and new ice forms. The transmittance of new first-year

ice evolves correspondingly to the melting sea-ice surface described above. From EFO until the beginning of winter (FO + 60 days), the strong growth of sea ice (e.g., increasing sea ice thickness) results in an exponential decrease in light transmission through newly formed FYI.

Phase VI: continuous freeze (from FO to FO + 60 days) This phase is characterized by continuous freezing, increasing snow accumulation towards an optically thick snow layer, and the gradual disappearance of melt ponds. In addition to new sea-ice formation, the existing sea ice is getting thicker and older, and deformation is increasing. Transmittance decreases back to 0.02 by winter. It is assumed that at the end of the freezing phase (FO + 60 days), the surface properties of all newly formed FYI can be considered to be equivalent. Afterwards, the accumulated optically thick snow layer again dominates the optical properties of FYI and MYI (Phase I).

Transmittance of bare ice and ponds

For the period after the year 2000, when satellite-derived melt pond products are available from Rösel and Kaleschke (2012), the transmittance values of bare ice (τ_b) and ponds (τ_p) are treated separately (Figure 3.3b). The modal transmittance of melt ponds is constant over the entire melt season. It is set to 0.22 for FYI and 0.15 for MYI, as measured during TransArc 2011 (Nicolaus et al., 2012). The seasonal evolution of transmittance for bare ice (τ_b) follows the transmittance for pond-covered sea ice (τ_i):

$$\tau_b(x, y) = \tau_i(x, y) \cdot \frac{\tau_b(\text{summer}, x, y)}{\tau_i(\text{summer}, x, y)}. \quad (3.5)$$

The values of $\tau_b(\text{summer}, x, y)$ and $\tau_i(\text{summer}, x, y)$ are the constant values during summer as given in Table 3.1. Thus, the ratio of both is constant for MYI (0.20) and FYI (0.46). Finally, those transmittance values are scaled with the pond concentrations, as given in Equation 3.2.

3.3.3 Deriving trends

Based on the calculated results of the solar heat input through sea ice into the ocean, trends are analyzed for the period 1979 to 2011. The trends (monthly and annual) are calculated by a linear least-squares fit of the total mean (monthly or annual) heat flux for each grid cell $Q_T(x, y)$. Resulting trends are normalized by trends in sea-ice concentration, because here we focus on radiative fluxes through the ice-covered part of the ocean. Otherwise, the results would depend strongly on regional and temporal trends in sea-ice concentration, because of the high transmittance (0.93) of open water. All trends were calculated for both the annual mean ice-covered area in 2011 and the monthly mean ice-covered area in 2011 (sea-ice concentration > 15 %) to allow for a representative comparison. Regions

3 The impact of Arctic sea ice surface melt on transmitted heat fluxes

Table 3.1: Transmittance values of different sea-ice and surface types. Abbreviations: FYI: first year ice; MYI: multi-year ice; Phase I: winter; MO: melt onset; Phase IV: summer; FO: freeze onset; Threshold: transition from open ocean to sea ice and vice versa.

	Phase I (winter)	At MO	Phase IV (summer)	At FO	Threshold
FYI, pond-covered sea ice	0.002	0.04	0.087	0.04	0.4
MYI, pond-covered sea ice	0.002	0.02	0.05	0.02	0.4
FYI, bare ice/snow	0.001	0.017	0.04	0.017	0.17
MYI, bare ice/snow	0.0	0.004	0.01	0.004	0.07
FYI, melt ponds			0.22		
MYI, melt ponds			0.15		
Open ocean			0.93		

that were not ice covered at any time in 2011 are excluded from the main analysis and discussion.

3.3.4 Input data sets

The following satellite and re-analyses data sets were used (Table 3.2):

1. Sea-ice concentration observations were obtained from the Special Sensor Microwave Imager (SSM/I/S) provided through the Ocean and Sea Ice Satellite Application Facilities (OSI SAF, product ID OSI-401, Andersen et al. (2007)). For this study, a combination of reprocessed data (1979 to 2007) and operational data (2008 to 2011) was used. Both data sets have systematic differences due to processing with a different set of tie point statistics for the ice concentration algorithm (Lavergne et al., 2010). However, within the documented uncertainties, both data sets build the best available and consistent time series of sea-ice concentration. There is no consistent uncertainty for the data product, but different approaches for determining uncertainties are described in Lavergne et al. (2010).
2. For sea-ice age, we used the updated data product by Maslanik et al. (2011, 2007). This product has been available since 1979, and is based on satellite-derived ice motion data calculated from different sensors using a Lagrangian feature tracking algorithm. Although this data product distinguishes ice ages between 1 and 10 years, here we only distinguish FYI and MYI (2 years and older), because all MYI is assumed to have similar optical properties. All data points with a sea-ice concentration of greater than 0 but without an assigned sea-ice age class were treated as FYI. Vice

Table 3.2: Data sources of the different parameters used in this study.

Parameter	Time period	Source
Sea-ice concentration	1979–2007	OSI SAF, reprocessed data
	2008–2011	OSI SAF, operated data (Andersen et al., 2007)
Sea-ice age	1979–2011	Maslanik et al. (2011, 2007)
Downward surface solar radiation	1979–2011	ECMWF (Dee et al., 2011)
Melt and freeze onset	1979–2005	SSMR
	2006–2010	AMSR-E
	2011	SSM/IS (Markus et al., 2009)
Melt pond fraction	1979–1999	Constant fraction as in 2011
	2000–2011	ICDC (Rösel et al., 2012)

versa, all data points with sea -ice concentration of greater than 15 % but which had an assigned sea-ice age class were treated as open water. Such modifications were necessary to obtain consistent data products from the different sources, indicating partially varying sea-ice extents. The ice age data set represents a 7-day average of either FYI or MYI without any uncertainty estimates. However, uncertainties in sea-ice concentration and drift will have an impact on the ice age data.

3. Downward surface solar radiation data were obtained four times per day from the European Centre for Medium-Range Weather Forecast (ECMWF) Era-Interim re-analyses (Dee et al., 2011; Lindsay et al., 2014). The data (four values per day) were averaged to daily means and have been available since 1979. Uncertainties for the data set are not reported.
4. Sea -ice surface characteristics were categorized by melt and freeze onset dates from passive microwave data (1979 to 2012) (Markus et al., 2009, updated). The data set distinguishes between the first occurrence of a melt event (early melt onset, EMO), the following continuous melt (melt onset, MO), the first occurrence of freeze-up conditions (early freeze onset, EFO), and the day of persistent freezing conditions (freeze onset, FO). The standard deviations, assumed as uncertainties, for the given dates are reported as $EMO \pm 3.6$ days, $MO \pm 3.7$ days, $EFO \pm 4.5$ days, and $FO \pm 4.0$ days (Markus et al., 2009, updated).
5. Melt pond fraction was used from Rösel et al. (2012), retrieved from the Moderate Resolution Imaging Spectroradiometer (MODIS) onboard NASA’s Terra and Aqua satellites. As this data set has only been available since 2000, melt pond fractions

3 The impact of Arctic sea ice surface melt on transmitted heat fluxes

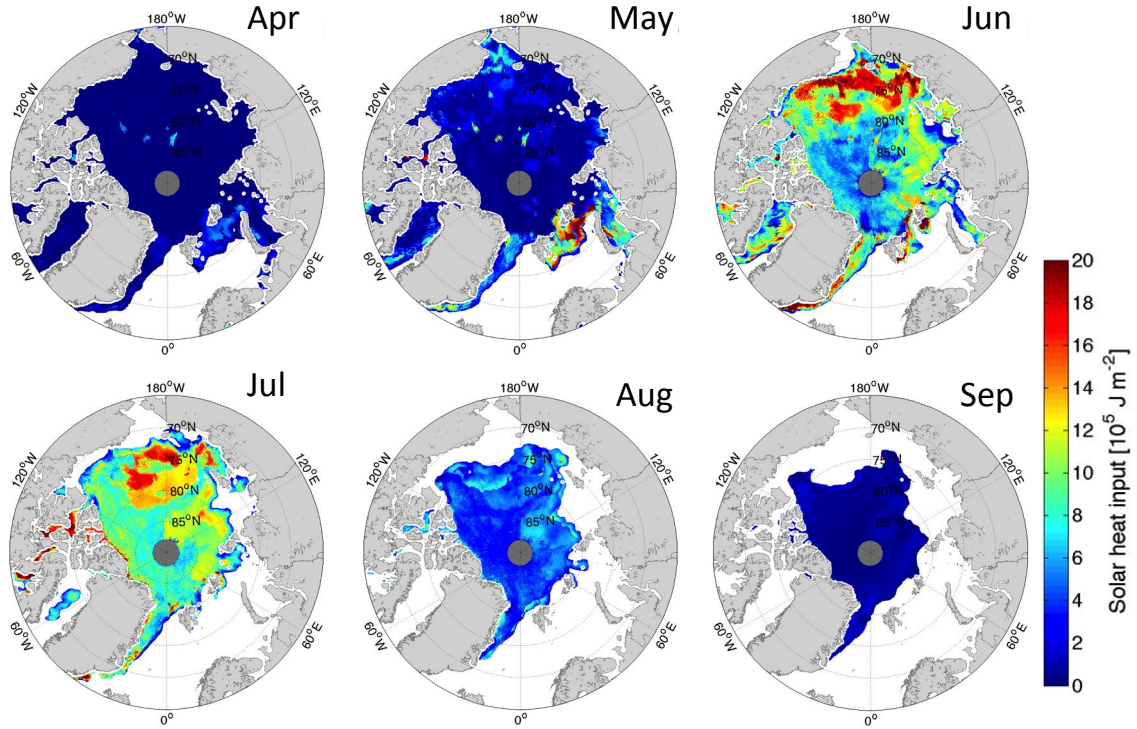


Figure 3.4: Monthly mean of total solar heat input ($Q_T(x, y)$) under Arctic sea ice (ice-covered areas only) for the year 2011.

from 1979 to 1999 were set to constant summer mean values of 26 % for FYI and 29 % for MYI, as given in Rösel et al. (2012) for August 2011. In order to maintain the consistency of the surface characteristics, all melt pond fractions before EMO are set to zero. The mean standard deviation from 2000 to 2011, assumed as uncertainty, is calculated as $\pm 3\%$ for FYI and MYI.

We do not include snow depth and sea-ice thickness as input data sets due to the lack of consistent high temporal resolution and long-term data products. Limitations of using sea-ice age as an indirect proxy for ice thickness and snow cover as well as potential other approaches for the estimation of transmitted heat fluxes are discussed below.

3.4 Results

3.4.1 Seasonal cycle of solar radiation under Arctic sea ice in 2011

Based on the availability of all input data sets and the seasonality of transmittance values, the solar heat input through sea ice into the ocean is analyzed from 1979 to 2011. Figure 3.4 shows monthly mean heat input ($Q_T(x, y)$, Equation 3.3) under Arctic sea ice (ice-covered areas only) from April to September 2011. The exemplary year of 2011 was selected to ensure a representative comparison with previous studies conducted in August 2011 by

Nicolaus et al. (2013, 2012). From October to March, the monthly mean solar radiation under sea ice was less than $0.2 \times 10^5 \text{ Jm}^{-2}$, with an Arctic-wide total under-ice heat flux (Q_T) of up to $0.4 \times 10^{19} \text{ J}$. Since this represents less than 1 % of the annual Arctic-wide heat flux of $53.3 \times 10^{19} \text{ J}$ (Equation 3.3), the months October to March are omitted from further analyses and discussion. In April, the mean heat flux increased to $0.4 \times 10^5 \text{ Jm}^{-2}$, with a maximum of 7 to $8 \times 10^5 \text{ Jm}^{-2}$; this amount of energy is equivalent to mean ice melt rates between 7 to 8 cm per month (Equation 3.4) in the marginal ice zone east of Spitsbergen. The transmittance triples from 0.005 in April to 0.015 in May, and together with increasing surface fluxes, the $Q_T(x, y)$ increased from $1.0 \times 10^{19} \text{ J}$ to $5.5 \times 10^{19} \text{ J}$ during this time. The Barents Sea showed a mean transmitted heat flux of $2.2 \times 10^5 \text{ Jm}^{-2}$ for the month of May, with a maximum value of $25 \times 10^5 \text{ Jm}^{-2}$, which corresponds to a maximum sea-ice melt of 25 cm per month. May to June showed the most pronounced monthly increases in $Q_T(x, y)$ of $9.3 \times 10^5 \text{ Jm}^{-2}$ and a transmittance of 0.054 for the entire Arctic. The maximum $Q_T(x, y)$ was $30 \times 10^5 \text{ Jm}^{-2}$ in June, with a corresponding maximum melt rate of approximately 30 cm per month. June also had the highest Q_T ($20.9 \times 10^{19} \text{ J}$), which was associated with the highest surface solar irradiance over the entire Arctic Ocean ($851 \times 10^{19} \text{ J}$). This increase in solar irradiance was linked to the beginning of the melt phase (mean MO on 30 May 2011) and the associated rapid snow melt. During this time, the difference between thin melting sea ice along the sea-ice edge and the persistent sea-ice cover became most obvious, e.g., in the Chuckchi and Beaufort seas. In July, Arctic-wide averaged $Q_T(x, y)$ reached its annual maximum of $9.8 \times 10^5 \text{ Jm}^{-2}$. This resulted primarily from the annual maximum in mean transmittance of 0.089, and led to a monthly flux Q_T of $18.4 \times 10^{19} \text{ J}$. The impact of the different optical properties (τ_i) of MYI and FYI became most obvious in July, because the difference in both values is at its maximum. In addition, the strong decrease in sea-ice concentration along the ice edge became more important for the under-ice heat fluxes, because light transmittance increased strongly in these regions. The August decrease in $Q_T(x, y)$ by more than 50 % to $4.4 \times 10^5 \text{ Jm}^{-2}$, along with only a slight reduction in transmittance to 0.084, can be explained by the strong decrease in surface solar irradiance ($679 \times 10^{19} \text{ J}$). These surface fluxes are only half of those calculated for previous months. August maximum $Q_T(x, y)$ reached up to $19 \times 10^5 \text{ Jm}^{-2}$. In September, the $Q_T(x, y)$ decreased further to $0.6 \times 10^5 \text{ Jm}^{-2}$, which can be related to a low transmittance of 0.039 and Q_T of $0.7 \times 10^{19} \text{ J}$.

3.4.2 Light transmission from 1979 to 2011

The new data set of $Q_T(x, y)$ allows quantification of annual budgets, regional differences, and decadal trends. Figure 3.5a shows the averaged annual solar heat input through sea ice into the ocean ($Q_T(x, y)$), and illustrates therefore the strong regional variability of $Q_T(x, y)$, ranging from 20 to 100 MJm^{-2} for the given period. This range in heat fluxes is equivalent to an ice melt rate of 24 to 120 cm yr^{-1} . The mean total solar heat input

3 The impact of Arctic sea ice surface melt on transmitted heat fluxes

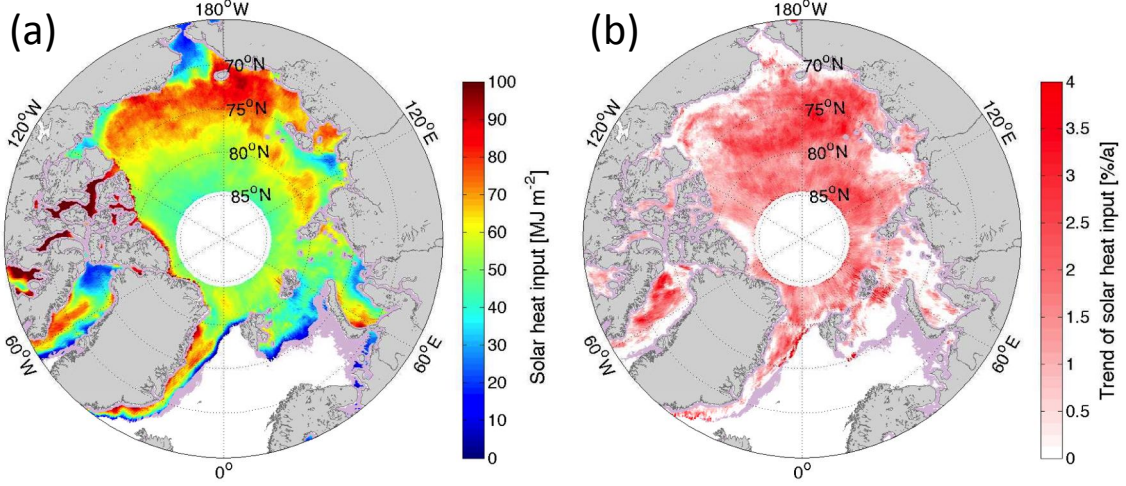


Figure 3.5: Annual total solar heat input ($Q_T(x, y)$) through Arctic sea ice. (a) Average and (b) trend from 1979 to 2011. The trend is normalized for the trend in sea-ice concentration. Purple shaded areas were not covered with sea ice during the maximum extent in all years.

transmitted through the considered sea-ice-covered area (Section 3.3.3) was 46 MJ m^{-2} . The maximum $Q_T(x, y)$ occurs at the edge of the marginal ice zone in the Canadian Arctic Archipelago (up to $110 \text{ MJ m}^{-2}/130 \text{ cm}$ melt per year) and the East Siberian and Chukchi seas (up to $80 \text{ MJ m}^{-2}/94 \text{ cm}$ melt per year). In contrast, excluding areas characterized by a strong spring sea ice retreat and a corresponding low sea-ice concentration, the minimum $Q_T(x, y)$ was found in the central Arctic, an MYI-dominated region of low transmittance.

The mean trend of $Q_T(x, y)$ was $1.5 \% \text{ a}^{-1}$ (excluding areas with a strong spring sea-ice retreat), with a maximum of $+4 \% \text{ a}^{-1}$ in the East Siberian Sea and the southern part of the North American and Russian Arctic Basin (Figure 3.5b). This trend translates to a 63% increase in the potential sea-ice melt over the 33-year observation period. This is likely due to the prolongation of the melt season in the same regions. According to a linear regression from 1979 to 2011 for the entire Arctic, the mean MO was 4 days earlier, shifting from day 145 (24 May) to day 141 (20 May). The strongest trend of $4.8 \times 10^{18} \text{ J a}^{-1}$ was found for June, followed by May and July with $1.8 \times 10^{18} \text{ J a}^{-1}$. August shows a comparably weak negative trend of $-0.2 \times 10^{18} \text{ J a}^{-1}$. Assuming an identical sea-ice extent in 1979 and 2011, the increase in the annual mean solar heat flux through sea ice (Q_T) amounts to $22.5 \times 10^{19} \text{ J}$ for the entire Arctic over the full study period. This corresponds to an average increase of 33%. Overall, 94% of the total annual solar heat input through Arctic sea ice was observed during the four key months: May to August. Furthermore, heat flux time series (annual, June, July) show an increasing variability after 1999 (Figure 3.6).

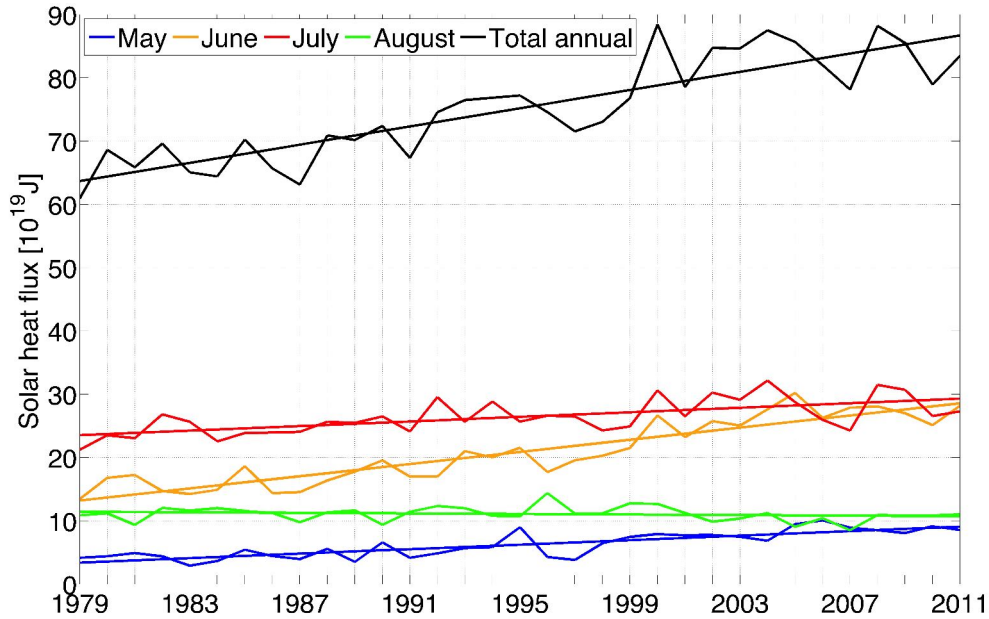


Figure 3.6: Arctic-wide total solar heat flux under sea ice (Q_T) (black) and monthly Arctic-wide solar heat input for May to August (colored) and its trend from 1979 to 2011. The data are corrected for the trend in sea ice concentration. Areas that were not ice covered at any time in 2011 or during a certain month in 2011 are excluded from the analyses.

3.5 Discussion

3.5.1 Seasonality and trends of transmitted fluxes

The total annual solar radiation under Arctic sea ice was estimated to be 53.3×10^{19} J in 2011. Based on this, May to August are the most important months for the radiative energy partitioning. During this period, 96 % (51.2×10^{19} J) of the total annual solar heat input is transmitted through the sea ice. Extending the period to April to September amounts to 99 % (52.9×10^{19} J) of the total annual flux being transmitted within only a 6-month period. Generalizing the monthly fluxes, the annual cycle can be summarized in three phases: (1) the heat input through snow and sea ice into the ocean is negligible between October and March, (2) surface solar radiation dominates the under-ice light conditions from April to June, because transmittance increases only slowly, while surface irradiance determines most of the observed changes and variability, and (3) during summer (July to September), energy fluxes depend mainly on the sea-ice type, showing large differences in transmittance between FYI and MYI.

Comparing our results to the development of the solar heat input into the ice presented by Perovich et al. (2011a, Figure 2), both the solar heat input to the upper ocean and

3 *The impact of Arctic sea ice surface melt on transmitted heat fluxes*

the solar heat input to the sea ice demonstrated a positive annual trend of 1 to 1.5 % yr⁻¹ during the last decades. The increasing energy in the ice and upper ocean might both lead to a stronger sea-ice melt. Therefore, the radiative heating of the upper ocean might contribute to a higher conductive ocean heat flux to the ice. This increase in bottom melt is affecting the sea-ice mass balance. An increasing light absorption of Arctic sea ice due to more seasonal ice and less multi-year ice was also found by Nicolaus et al. (2012).

The trend towards more light transmission through sea ice does not only impact the light conditions right at the bottom of the sea ice, but also affects the horizontal and vertical light field in the ice-covered ocean. More light at the bottom of sea ice will deepen the euphotic zone, as more light penetrates deeper into the ocean (Frey et al., 2011; Katlein et al., 2014). More light can contribute to an increase in mixed layer temperature, and provide more energy for primary production and biogeochemical processes in and beneath the sea ice. However, it has to be noted that an increase in light availability does not necessarily increase biological activity, and might also be harmful (Leu et al., 2010).

An increase in transmittance will accelerate internal and bottom melt, which in turn will reduce the thickness of sea ice and increase transmittance. That feedback process can trigger a transmittance-melt feedback.

All presented trends are normalized with the trend in sea-ice concentration (Section 3.3.3). Thus, changes related to physical properties of the sea ice are highlighted instead of changes related to a general sea-ice retreat. Fluxes through the ice-covered ocean will be of great importance, and are much more difficult to assess than fluxes through open water. However, including the trend in sea-ice concentration, the annual trend of transmitted solar heat fluxes to the upper ocean decreases from +1.5 to ± 1.1 % a⁻¹. The negative trend in the open ocean heat input is evident in areas of ice motion causing an increase in ice concentration, which was also shown in Perovich et al. (2011a, 2007b). This comparison emphasizes the dominance of the albedo feedback mechanism and the strong influence of the trend in sea ice concentration on the heat budget of the entire system.

Beyond this, it is also important to consider that the trends in sea-ice concentration differ significantly during different months. While it is largest (-0.1 % a⁻¹) in September, it is only -0.06 % a⁻¹ in June, and even positive in April and May ($+0.04$ % a⁻¹). This means that the effect of increasing transmission through open water is particularly strong in September, but less pronounced in June, when the highest absolute fluxes are observed, or in spring, when the impact on biological primary production is expected to be strongest (Wassmann and Reigstad, 2011).

3.5.2 Comparison with field data

Validation of the calculated trends and spatial variability is nearly impossible, as insufficient field data with adequate spatial and temporal coverage are available. However, some comparisons with time series of light transmission from different field studies may

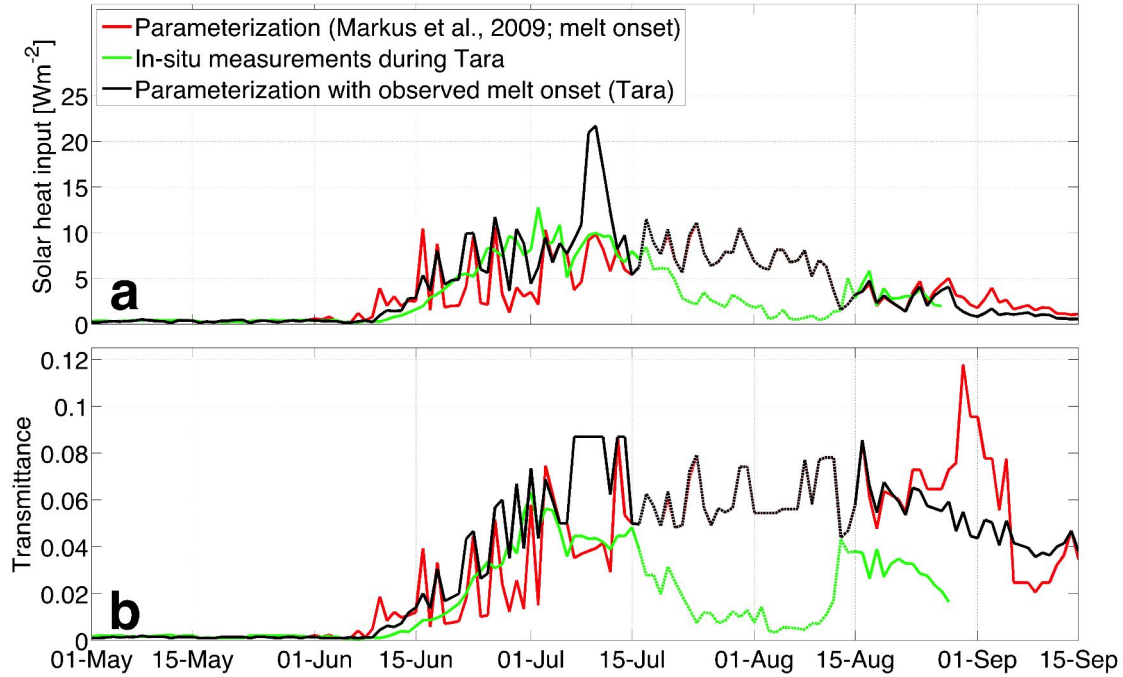


Figure 3.7: (a) Transmitted total solar heat input and (b) total transmittance during the drift of Tara in 2007 (Nicolaus et al., 2010b). Compared are in situ measurements (green) with the presented method (red), and the presented method, but using the observed dates for phase transitions (black). Between 16 July and 14 August (dotted lines), a comparison is not reasonable, since the sensor was strongly influenced by biological processes during Tara.

be performed to identify major uncertainties.

Here, we compare the surface and transmitted solar irradiance of the presented method with in situ measurements during the Transpolar Drift of Tara from 29 April to 28 August 2007 (Nicolaus et al., 2010a). Nearest-neighbor grid points within 0.5° of the daily Tara position were extracted from the presented data set and averaged. Figure 3.7a (red and green lines) shows a comparison of the time series for transmitted solar irradiance from both data sets. Until 8 June, the transmitted solar irradiance under sea ice varied only slightly, around 0.5 Wm^{-2} , for both the calculated and measured time series. Afterwards, until the end of June, the measured transmitted fluxes increased steadily towards 10 Wm^{-2} , whereas calculated fluxes were highly variable, with most values below 4 Wm^{-2} . Hence, the total solar heat input through the sea ice to the ocean from 1 May to 16 July 2007 was 21.4 MJ m^{-2} for the observed Tara data, whereas the calculated data resulted in a 17% lower total heat flux of 17.7 MJ m^{-2} . The calculated underestimation is equivalent to 1 cm of sea-ice melt for this period. During summer (16 July to 14 August 2007), under-ice fluxes cannot be reliably compared, since the sensor at the Tara study was strongly influenced by biological processes in ice and water, causing increased

3 The impact of Arctic sea ice surface melt on transmitted heat fluxes

absorption and reduced transmitted fluxes. Thus, the calculated fluxes were overestimated by 11.6 MJ m^{-2} , representing an equivalent sea-ice melt of 4 cm during summer.

After 14 August, the measured transmitted heat flux increased rapidly to about 6 Wm^{-2} , comparable to the calculated value. Finally, the decrease in solar elevation caused decreasing transmitted fluxes in both data sets, resulting in similar heat fluxes of $0.28 \times 10^3 \text{ MJ m}^{-2}$ after 14 August.

The main reason for these differences is the timing of the phases describing the surface characteristics. While both data sets have a coincident EMO on 9 June, large differences are evident for the later phase transitions: the observed MO at Tara was on 21 June, whereas the calculated MO for the center position was 17 days later on 8 July. Considering the eight neighboring cells results in a mean MO on 13 June. This shows that there is a difference of 25 days in MO for the 10 km grid. As presented above, the transmitted heat flux depends strongly on the timing of the different melt phases by Markus et al. (2009). EFO was observed on 15 August during Tara, whereas the satellite data maintain summer melt conditions until 14 September. However, the total solar heat input through sea ice was similar for both data sets. Thus, the solar radiation flux under Arctic sea ice depends strongly on the timing of EMO and MO, while the timing of EFO and FO seems to be of less importance, since the beginning of the melt season coincides with maximum surface solar heat fluxes. The timing of melt onset also has a large influence on the total amount of light absorption, as shown in Stroeve et al. (2014). Including the ongoing lengthening of the melt season by up to 2 weeks per decade (by a later EMO), Stroeve et al. (2014)) calculations suggest an albedo decrease of 9% per decade.

In a second validation step, the heat fluxes were re-calculated using the onset dates as observed during Tara instead of those by Markus et al. (2009) (Figure 3.7, black lines). This eliminated the impact of the onset dates on the results. Nevertheless, the calculated total solar heat input through sea ice still differed by 18% (25.4 MJ m^{-2}) from the Tara fluxes until 16 July (Figure 3.7a), due to an unexpected peak in $Q_{\text{T}}(x, y)$ in July. In addition, the calculated time series still showed large day-to-day variability, including much higher transmittance values than observed at Tara. The main reason for this is the combination of both sea-ice types (FYI and MYI), whereas the Tara floe consisted of MYI only. Consequently, the strong differences in optical properties of FYI and MYI, as parameterized here, strongly contribute to the overall energy budget. To overcome this problem, FYI/MYI fractions per grid cell (Kwok, 2004) could be used instead of the presented discrete distinction. However, such a data set is not yet available for the given time span.

Hudson et al. (2013) measured heat fluxes and calculated transmittance values of Arctic FYI in July/August 2012. However, a direct comparison of energy fluxes, as for the Tara measurements, is not possible, because the melt-pond concentration data set ends in December 2011. August transmittance in our study (0.087) is based on the observations by Nicolaus et al. (2012), which is only half of the 0.16 found by Hudson et al. (2013).

Hence, it may be assumed that heat fluxes through sea ice would be larger, based on those measurements. Differences between both studies mainly result from differences in sea-ice thickness during the respective campaigns as well as the different methods of quantifying transmittance (mean value vs. modal value) (Hudson et al., 2013).

3.5.3 Limitation

Measurements from ice-tethered profilers (ITPs) (Krishfield et al., 2008) could be used as an alternative approach to estimate uncertainties of the new parameterization. They allow quantification of the heat content of the uppermost ocean and its changes. However, such a comparison would require a significant extension of the present study, integrating radiation fluxes to larger depths and through open water. Similarly, the inclusion of a radiation transfer model is beyond the aim of this study. The advantage of this study is the rather simplistic approach based on a seasonal parameterization of under-ice fluxes applied to existing large-scale data products.

An improvement to this study would be the inclusion of sea-ice thickness (e.g., CryoSat-2, IceSat, OperationIceBridge) and snow depth (e.g., AMSR-E) observations from satellites. As with all other input data, the above-mentioned products need to be consistent over many years and reliable during all seasons. However, this is not the case yet, and even the most recent data sets have huge uncertainties or are not available after melt onset (e.g. Ricker et al., 2014), which is the most important time with respect to transmitted heat fluxes. Hence, these parameters are not applicable for such parameterizations yet. Instead, sea-ice age is used as a proxy for ice thickness and snow depth distribution. It also includes information about roughness and deformation of the sea-ice surface. These characteristics are crucial for the description of optical properties of sea ice.

In addition, including data sets of different model simulations, such as sea ice thickness, snow depth, and melt pond fraction (e.g. Flocco et al., 2012; Schröder et al., 2014), can be considered to be an alternative approach for the presented calculations.

Another uncertainty in the presented heat flux calculations results from constant values for the transmittance of melt ponds on FYI and MYI. Based on our existing data, it was not possible to include a seasonality in melt pond transmittances, which represents the different formation and evolution stages (Perovich and Polashenski, 2012). However, the applied transmittances of melt ponds are modal values of a distribution function (Nicolaus et al., 2012), representing a range of possible values. This has to be considered when comparing our fluxes to other observations or model results. Overall, we expect that the uncertainties resulting from the missing seasonal cycle will have a much smaller impact than the timing of melt onset, which is discussed in the next section.

3 The impact of Arctic sea ice surface melt on transmitted heat fluxes

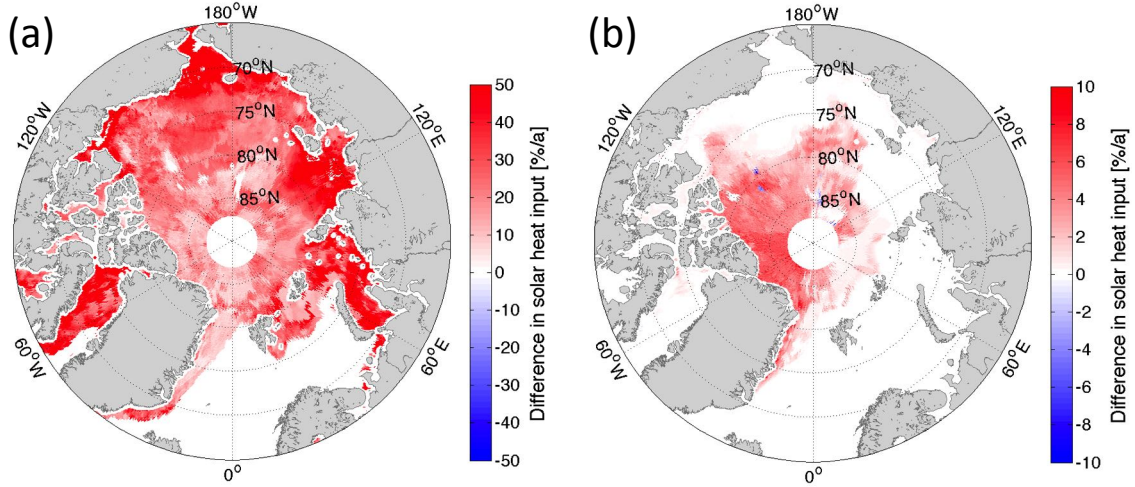


Figure 3.8: Changes in annual total solar heat input ($Q_T(x, y)$) through sea ice in 2011, resulting from a sensitivity study assuming an extended melt season. a) 14 days earlier early melt onset and melt onset, and (b) 14 days later early freeze onset and freeze onset than in the reference method, based on Markus et al. (2009).

3.5.4 Sensitivity studies

Based on uncertainties of the independent input variables (timing and length of the melt season, ice age, and melt pond fraction), several sensitivity studies have been performed to estimate the uncertainty for the presented parameterization.

The first study studies the effect of altering the timing and duration of the melt season on the solar heat input to the upper ocean. Three cases are discussed: shifting the melt season dates by (Case 1a) the average uncertainty of 4 days, as given by Markus et al. (2009), (Case 1b) 7 days based on the temporal resolution of ice age data (once per week) (Maslanik et al., 2011), and (Case 1c) (averaged) 14 days, as derived from comparisons with the Tara field data (Nicolaus et al., 2010a). Based on the observed ongoing trend towards a lengthening of the melt season, all sensitivity studies were only performed for earlier EMO and MO, and a later EFO and FO for the exemplary year of 2011.

Extending the melt season by 4 days (Case 1a) results in Arctic-wide mean EMO on 12 May and MO on 27 May. This affects most regions primarily during periods of high sea-ice concentration and large surface solar irradiance. It results in an increase in total annual solar heat input through sea ice to the ocean (Q_T) of 7%, from 53.3×10^{19} J to 57.0×10^{19} J, for the entire year of 2011. The strongest increase of 20% compared to the reference melt onset dates was found in May, while the strongest absolute increase of 1.9×10^{19} J was found in June.

Including 7 days earlier EMO and MO (8 May and 23 May, respectively) (Case 1b) result in an additional heat input of 5.9×10^{19} J (+11%) compared to the reference system for the total annual heat input to the upper ocean. Shifting the melt season another 7 days (Case 1c) backwards (1 and 16 May), the increase in Q_T is more than double compared to

Table 3.3: Annual Arctic-wide solar heat input (and relative changes) under sea ice (Q_T) in 2011 for the reference method and sensitivity study I: changes in melt season duration by a shift of 4 days (data uncertainty, Markus et al. (2009)), 7 days (estimated uncertainty due to the only weekly sea-ice age data by Maslanik et al. (2011)), and 14 days (derived from comparisons to field data; Nicolaus et al. (2010a)). All trends were only performed towards a prolongation of the melt season. All numbers are in 10^{19} J.

	Reference	Changing EMO and MO		
	system	−4 days	−7 days	−14 days
Apr	1.00	1.17 (+17 %)	1.19 (+19 %)	1.45 (+45 %)
May	5.53	6.64 (+20 %)	7.35 (+33 %)	10.5 (+90 %)
Jun	20.9	22.8 (+9 %)	24.0 (+15 %)	27.1 (+30 %)
Jul	18.4	18.7 (+2 %)	19.1 (+4 %)	19.7 (+7 %)
Aug	6.33	6.34 (0 %)	6.42 (+1 %)	6.48 (+2 %)
Sep	0.69	0.69 (0 %)	0.69 (0 %)	0.69 (0 %)
Jan–Dec	53.3	57.0 (+7 %)	59.2 (+11 %)	66.3 (+24 %)

	Reference	Changing EFO and FO		
	system	+4 days	+7 days	+14 days
Apr	1.00	1.00 (0 %)	1.00 (0 %)	1.00 (0 %)
May	5.53	5.53 (0 %)	5.53 (0 %)	5.53 (0 %)
Jun	20.9	20.9 (0 %)	20.9 (0 %)	20.9 (0 %)
Jul	18.4	18.4 (0 %)	18.4 (0 %)	18.4 (0 %)
Aug	6.33	6.46 (+2 %)	6.51 (+3 %)	6.68 (+5 %)
Sep	0.69	0.74 (+7 %)	0.81(+17 %)	0.97 (+41 %)
Jan–Dec	53.3	53.4(0 %)	53.6 (+0 %)	53.9 (+1 %)

the 7-day shift (Table 3.3, 66.3×10^{19} J). The pronounced increase is most evident in May, when 90 % more light transmission was found than in the reference system. The strongest absolute increase of 6.2×10^{19} J (transmittance from 0.054 to 0.067) was calculated for June. The spatial distribution in the impact of the 14-day earlier EMO and MO showed the largest increase in solar heat input to the upper ocean in the marginal ice zone, with increases greater than 100 % (Figure 3.8a).

Extending the melt season by 14 days later EFO and FO (Case 1c) (21 October and 2 November, respectively) result in a 1 % increase in Q_T from 53.3×10^{19} J to 53.9×10^{19} J (Figure 3.8b). Since the surface solar radiation is much less than between April and June,

3 *The impact of Arctic sea ice surface melt on transmitted heat fluxes*

the change at the end of the melt season is small during August and September (increase of 9 % from 7.02×10^{19} J to 7.65×10^{19} J). Seven-day or rather four-day (cases 1a and 1b) later EFO and FO have a negligible effect on the total annual transmitted heat flux of less than 1 %.

In a second sensitivity study, the influence of the ice type was quantified. As the sea-ice type data contain no uncertainty, the study is based on the ongoing trend towards a predominantly FYI-covered Arctic Ocean. The reference ice cover of 2011 consists of 56 % FYI and 44 % MYI in August 2011. Assuming that all sea ice in 2011 was MYI, the mean transmitted flux decreased by 34 % to 35.5×10^{19} J. In contrast, assuming that only FYI was present increased the mean transmitted flux by 18 %, to 62.7×10^{19} J. Hence, the transition from an MYI- to FYI-dominated Arctic sea-ice regime results in a further increase in solar heat flux under Arctic sea ice.

The third sensitivity study investigates the effects of melt pond fraction uncertainties. Here, we consider two cases: (Case 3a) Rösel et al. (2012) give a mean uncertainty of 3 %, and (Case 3b) we estimate an uncertainty of 20 % due to the neglected seasonal cycle. Adapting these assumptions, an increasing melt pond fraction of 3 % (20 %) results in an increase in the transmitted heat flux of 1 % (9 %).

Uncertainties in the solar surface radiation and sea-ice concentration are not analyzed through additional sensitivity studies, because they impact the results linearly (Equation 3.2).

3.5.5 Additional parameters influencing the Arctic under-ice light field

Optical properties of sea ice (and snow) are highly dependent on the prevalent surface properties, as e.g. the presence of snow and melt pond coverage, but also on direct physical properties, as e.g. sea-ice thickness and snow depth (Section 3.2.1). While the presented study uses sea-ice age as a proxy for sea-ice thickness and snow depth distribution to estimate Arctic-wide under-ice radiation fluxes, Katlein et al. (2015) investigate the influence of ice thickness and surface properties (albedo and melt pond coverage) on the spatial variability of the under-ice light field on different scales. Doing so, they measured spectral under-ice radiance and irradiance with radiation sensors mounted on a Nereid Under-Ice (NUI) underwater robotic vehicle which was operated during the expedition of the German research ice-breaker R/V Polarstern to the Aurora mount in the Arctic Ocean (83° N 6° W) in July 2014. They combined the optical under-ice measurements with three-dimensional under-ice topography (and derived sea-ice thickness) from the mounted multi-beam sonar and areal images from helicopter surveys to quantify surface conditions. The subsequent analysis is subdivided into surveys: One is containing a well defined 100-m-survey conducted at a constant depth of 5 m, referred in the following as pole survey. The second is a random 2 km long survey under the heterogeneous ice floe (whole survey). Results of the study show that overall 72 % of the variance in the spatially varying under-ice light field

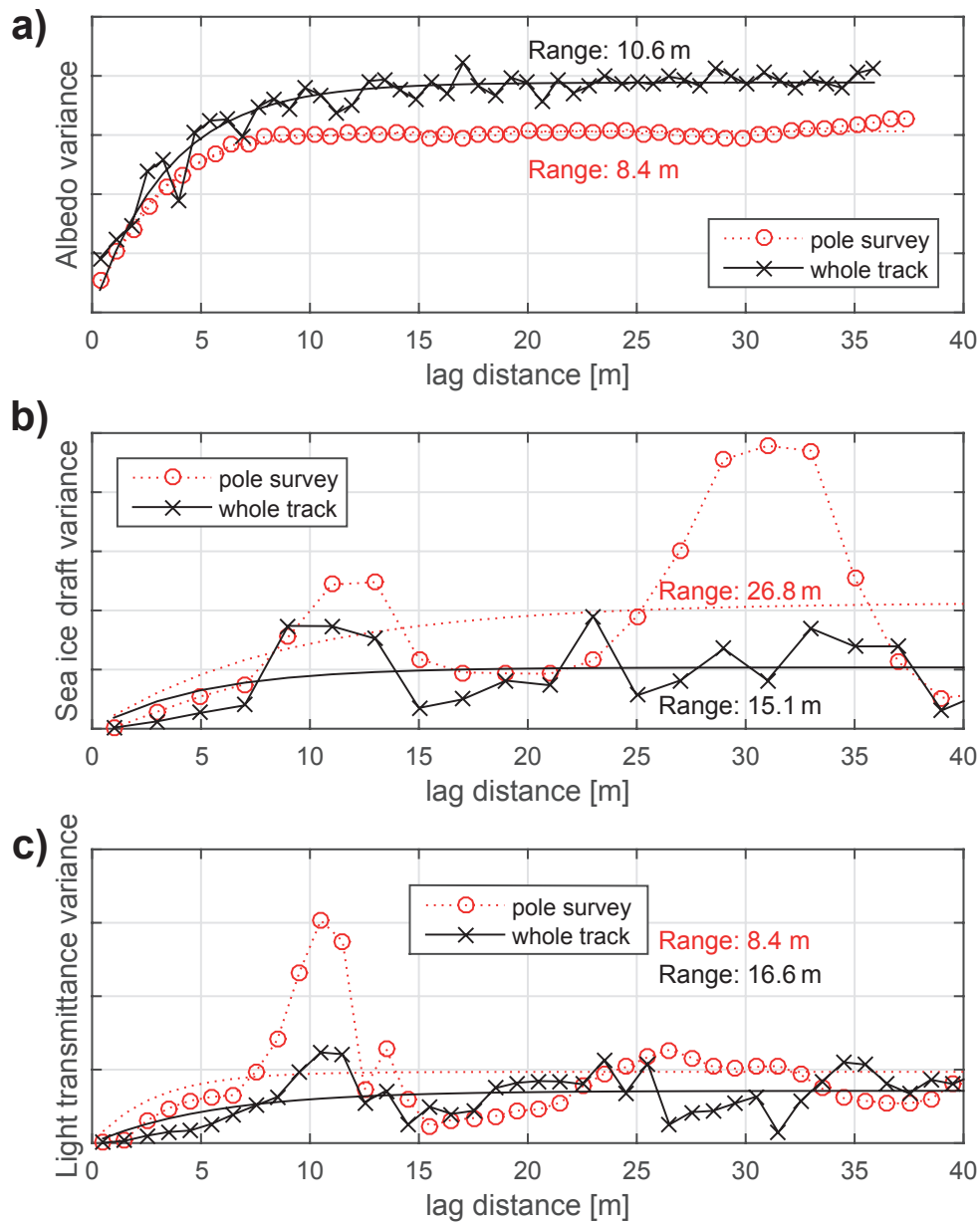


Figure 3.9: Variograms of (a) surface albedo, (b) sea-ice draft, and (c) light transmittance. Red lines indicate variograms obtained from the pole survey, while black lines are derived from the whole survey. Empirical variograms are shown with x as data marker, while unmarked lines are fitted theoretical exponential histograms. The range values obtained from the fitting are given as annotations in the same color as the corresponding curve. Variance is given in arbitrary units starting from zero. Figure provided by Katlein et al. (2015).

can be explained by ice draft and surface albedo, and thus the dominant melt pond coverage during spring/summer in the Arctic. The subsequent analysis of the spatial scales using variograms (Figure 3.9) reveal a similar characteristic length scale for surface albedo

3 *The impact of Arctic sea ice surface melt on transmitted heat fluxes*

variations and under-ice light variability of about 10 m, the typical length scale of melt ponds, considering small areas of less than 1000 m². These results are consistent with similar studies by Perovich et al. (1998) and Nicolaus et al. (2012). In contrast, the variability of the under-ice light regime on larger scales (length scale about 17 m) is mostly driven by variations in sea-ice thickness (length scale about 15 m), which in turn reflects dominant sea-ice properties as the variability in ice types and its deformation. Thus, the authors suggest the use of ice thickness to describe large-scale light transmission through Arctic sea ice. Nevertheless, this approach is only feasible for summer months and in upcoming model simulations as time series of ice thickness and snow depth are so far not consistent over many years and reliable in all seasons, as mentioned above (Section 3.5.3).

3.6 Summary and Conclusions

The presented parameterization for light transmission through Arctic sea ice in combination with satellite-derived time series observations and re-analysis data allowed the quantification of solar short-wave radiation fluxes through Arctic sea ice for the entire annual cycle over 33 years (1979 to 2011). The presented results suggest that 96 % of the total annual solar heat input through sea ice occurs over only 4 months (May to August), with the highest transmitted fluxes calculated for June. Over the time period 1979 to 2011, an increase in light transmission of 1.5 % yr⁻¹ with regional maxima of 4.0 % was found. Hence, the amount of short-wave radiation that may contribute to sea-ice bottom melt increased by 63 % over this 33-year period. The results of our sensitivity studies show that energy fluxes depend strongly on the timing of melt onset, sea-ice types (first- and multi-year ice), and melt pond fraction. These are the most critical parameters for the presented calculations, and describe the most critical uncertainties. The calculated trends are affected by most of these uncertainties.

This study considers the fluxes through ice-covered ocean regions only. This highlights the fact that changes in sea-ice properties have a large impact on the sea ice and upper ocean energy budget, and that this impact adds to the obvious increase in energy input resulting from the observed decrease in ice-covered areas (open ocean effect). However, the ongoing retreat of sea ice will cause additional increases in radiation fluxes into the Arctic Ocean. The additional heat will also contribute to an increase in heat stored in the ocean mixed layer, and will impact the melt season duration and timing, particularly during autumn freeze-up.

A comparison of trends in solar heat fluxes into the sea ice by Perovich et al. (2011a) with our calculated solar heat fluxes through sea ice suggests similar increases in transmitted and absorbed energy. This additional energy input into the sea ice and the upper ocean would also impact inner sea-ice structures as well as internal and basal melting. Studies from Perovich et al. (2011a) and Nicolaus et al. (2013, 2012) reveal that fluxes through open water clearly dominate the transmitted heat flux signal and, therefore, the effect of

sea-ice concentration becomes most obvious. Since our presented study focuses on changes in physical properties of sea ice and its effects, all calculated trends are corrected for the trend in sea-ice concentration, and fluxes through open water are neglected. Also, the effects of heat convection and advection as well as lateral heat fluxes are not discussed, due to the limited number of recent studies on that topic.

More investigations of bio-geo-physical interactions are needed to quantify better the effects of the changing physical environment on the ecosystem and element cycles, and vice versa. Additional work is also required to improve Arctic-wide snow depth and sea-ice thickness data products. Those products should provide a good description of surface properties during the spring–summer transition, when the largest uncertainties were found. Such time series might become available from new data products that merge observations from different satellites and sensor types (e.g., SMOS, CryoSat-2, AMSR-E), and potentially also numerical models. The non-existence of such reliable long-term and Arctic-wide data sets was the main motivation for developing the presented method, based on available parameters. Otherwise, the application of a radiation transfer model with adequate input (forcing) data would have been an obvious alternative.

4

Timing and regional patterns of snowmelt on Antarctic sea ice from passive microwave satellite observations

Results of the previous chapter identify and discuss dominant surface properties, and processes controlling the energy budget and its influence on, e.g., bottom melting rates of Arctic sea ice. It is shown that especially solar radiation transmitted through the sea ice to the upper ocean depends not only on the prevalent sea-ice type and melt pond coverage but in particular on the timing of the melt onset in the Arctic Basin. Compared to the distinct seasonal cycle of surface properties of Arctic sea ice, Antarctic sea ice is generally snow-covered throughout the year while the physical properties of the snowpack change substantially. It is therefore important to understand the mechanisms that drive the changing properties of the southern snowpack, both at different times of the year and in different regions.

In this chapter, we combine two approaches to observe both temporary surface snowmelt and (deep) continuous volume snowmelt using passive microwave satellite data. The former is achieved by analyzing diurnal variations in the brightness temperature, the latter by analyzing a brightness temperature ratio composed of different frequencies and polarizations. Moreover, we use both melt onset proxies to divide the entire Antarctic sea-ice cover into regions of characteristic surface melt patterns from 1988/1989 to 2014/2015. The results enable to improve the understanding of the atmosphere-ice-ocean interactions in the Southern Ocean, which are important for a better quantification of the energy and mass budgets of Antarctic sea ice.

This chapter is, with marginal changes, identical to the content published in Arndt et al. (2016).

4.1 Introduction

The energy fluxes through sea ice and its snow cover differ strongly between melting and freezing seasons (Arndt and Nicolaus, 2014; Perovich and Polashenski, 2012; Perovich et al., 2002). As Antarctic sea ice is covered with snow during most of the year (Massom et al., 2001), transitions between these seasons strongly affect snow-property and snow-volume changes. Snow metamorphism and an increasing liquid water content

4 Timing and regional patterns of snowmelt on Antarctic sea ice

in the snow pack at the spring-to-summer transition modify the surface energy budget by decreasing the surface albedo, causing increased absorption and transmission of solar radiation (Brandt et al., 2005; Massom et al., 2001). Surface and subsurface snowmelt processes initiate melt water penetration through the snowpack and the subsequent formation of superimposed ice at the snow/ice interface (Brandt and Warren, 1993; Haas, 2001). Moreover, it results in a decreasing snow depth. Internal snowmelt contributes to the sea-ice mass balance of Antarctic sea ice Eicken et al. (1994); Haas et al. (2001); Massom et al. (2001).

Passive microwave sensors can detect changes of the snow liquid water content as it leads to a substantial alteration of the microwave emissivity ε and hence of brightness temperature T_B (e.g. Foster et al., 1984; Ulaby et al., 1986). The seasonal evolution of snowmelt and the associated changes in T_B differ significantly between the Arctic and the Antarctic (Andreas and Ackley, 1982; Nicolaus et al., 2006; Willmes et al., 2014). On Arctic sea ice, the formation of liquid water during initial surface melt leads to increasing ε and T_B (Comiso, 1983; Drobot and Anderson, 2001). As soon as slush and/or melt water forms at the ice surface, T_B decreases again due to the high free-water content (Garrity, 1992). The subsequent widespread ponding is triggered by air temperatures remaining consistently above the freezing point (e.g. Flocco et al., 2012; Nicolaus et al., 2010a; Rösel and Kaleschke, 2012; Webster et al., 2015). Based on the distinct seasonal cycle of microwave signatures of Arctic sea ice, Belchansky et al. (2004); Livingstone et al. (1987); Markus et al. (2009) identified different stages of melt transition.

In contrast, snow on Antarctic sea ice generally persists year-round, but undergoes substantial seasonal changes in physical properties (Massom et al., 2001). The transport of cold, dry air masses from the continental shelf leads to a low relative humidity and weak surface snowmelt during austral spring (Andreas and Ackley, 1982). Instead, Eppler et al. (1992) and Willmes et al. (2009, 2006) describe diurnal thawing and refreezing of snow as measured by variations of surface microwave properties, which can be used to identify the onset of surface melt. The diurnal freeze-thaw cycles cause widespread layers of metamorphous snow with increased snow grain sizes, dense layers and superimposed ice, which forms at the snow/ice interface on Antarctic sea ice (Nicolaus et al., 2009).

Willmes et al. (2009) detected the snowmelt onset on Antarctic sea ice using differences in microwave brightness temperatures at 37 GHz, measured in the morning and evening, using a fixed threshold. However, the depth, at which diurnal freeze-thaw cycles are effective in the snow, differs regionally and temporally due to varying snow properties and atmospheric conditions. Hence, also snow layers below the penetration depth of the 37 GHz channel need to be monitored. We therefore investigate the additional use of the 19 GHz channel which provides more detailed information on the stage of subsurface melt processes because of the larger penetration of longer microwaves into the snowpack (Abdalati and Steffen, 1997; Ashcraft and Long, 2003).

The aim of this study is to determine the timing of snow melt onset, to distinguish

dominant surface melt processes, i.e. temporary and continuous melt, and to analyze their regional characteristics. To do this, we use locally-determined thresholds for the identification of freeze-thaw cycles, and include an additional microwave parameter that is considered indicative of strong and continuous melt. We analyze microwave brightness temperature time series from 1988/1989 to 2014/2015, to study the long-term variability in snowmelt processes and their spatial distribution. These spatio-temporal characteristics of snowmelt on Antarctic sea ice can contribute to a better understanding of the uncertainty and variability of sea-ice concentration and snow-depth retrievals in regions of high sea-ice concentrations (Andersen et al., 2007; Comiso et al., 1997; Markus et al., 2006).

4.2 Melt transition retrieval from passive microwave data

4.2.1 Background

The seasonal variability in the physical properties of snow has strong effects on its microwave properties. The microwave emissivity, ε , of snow and the measured microwave brightness temperature, T_B , are functions of frequency, f , and polarization, p . They are related by

$$T_B(f,p) = \varepsilon(f,p) \cdot T_S, \quad (4.1)$$

where T_S is the effective physical temperature of the emitting body (Ulaby et al., 1986).

Dry snow appears almost transparent to microwave frequencies below approximately 30 GHz, which means that the measured T_B is mainly influenced by the upper ice layer. Signals acquired at higher frequencies have lower penetration depths and are therefore partly or entirely influenced by the snow properties, even when the snow is dry (the penetration depth into dry snow at 37 GHz is about 0.5 m, Garrity (1992)). When snow starts to melt, surface scattering increases and volume scattering decreases (Mätzler and Hüppi, 1989). As the liquid water content of the snowpack increases, the water absorbs more microwave energy, which causes the snowpack’s microwave emissivity to increase (Abdalati and Steffen, 1997; Tedesco, 2015). Abdalati and Steffen (1995) show that the associated T_B increase is more pronounced at horizontal than at vertical polarization. This polarization difference diminishes with increasing snow wetness due to changes in dielectric properties at the air/snow interface. Moist snow affects the brightness temperature at all frequencies as well as its penetration depth. For liquid water contents larger than 2%, Ulaby et al. (1986) determined a reduction in penetration depth to about 2 cm at 37 GHz, and to 8 cm at 19 GHz.

Comparing surface melt processes of Arctic and Antarctic sea ice, significant differences are obvious between both hemispheres (Nicolaus et al., 2006). In contrast to the Arctic, no persistent and large-scale formation of liquid water in the snowpack occurs in the

4 Timing and regional patterns of snowmelt on Antarctic sea ice

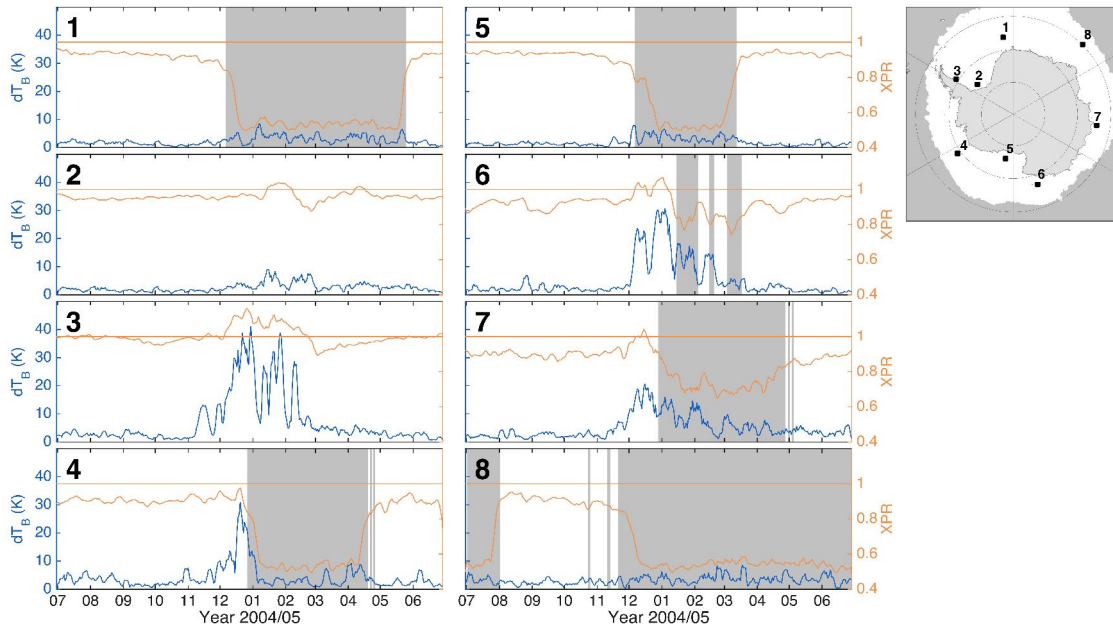


Figure 4.1: Example time series of diurnal variations in brightness temperature (dT_B , blue) and the cross-polarized ratio (XPR, orange) for 8 locations in the Antarctic sea-ice area (upper right panel), July 2004 to June 2005. Grey-shaded areas indicate a sea-ice concentration below 70%. In the upper right map, the white areas indicate the maximal sea-ice covered area of the previous year.

Antarctic (Drinkwater and Liu, 2000). As soon as the spring-summer transition starts, the snow surface melts during the daytime (causing higher values of T_B) and refreezes during the nighttime (causing a decrease of T_B). Consequently, Willmes et al. (2009) relate the observed diurnal brightness temperature differences to temporary thawing and refreezing of snow. Due to the frequent diurnal freeze-thaw cycles, snow grain sizes increase, and extensive snow metamorphism begins. This metamorphism decreases the microwave emissivity and thus T_B , in contrast to the increase of these parameters for Arctic sea ice since the liquid water content increases drastically as soon as surface melt starts (Markus et al., 2009).

4.2.2 Melt onset proxies from passive microwave data

Diurnal variation of brightness temperature (dT_B)

Willmes et al. (2006) identified the onset of summer melt on Antarctic sea ice by combining passive-microwave observations and field measurements during the Ice Station POLarstern expedition (ISPOL, summer 2004/05, Hellmer et al. (2006)). By analyzing time series of the absolute difference between the two diurnal T_B values from ascending and descending satellite passes (dT_B , 37 GHz, vertically polarized) they found an increase of dT_B once the temporary snowmelt onset at the snow surface started. Their algorithm defines the

onset of summer conditions typical for the Weddell Sea as the first date at which the dT_B exceeds a fixed threshold of 10 K for at least 3 consecutive days.

Here, we show that the characteristics of the seasonal dT_B evolution (blue curves in Figure 4.1) differ mainly in (1) timing and magnitude of the absolute maximum of the dT_B values (in the following denoted as peak value), and (2) the length of the period with increased dT_B values as compared to the pre-summer season (the period with the highest peaks, here denoted as peak broadness). E.g., Location 7 indicates a peak value of 26.0 K, whereas dT_B rises up to 41.1 K at Location 3. Furthermore, the peak broadness differs from one month, e.g. at Location 4, in areas of dropping sea-ice concentration (SIC), up to 4 months, in all-year ice-covered areas such as Location 3. These regional differences in the peak value and peak broadness of the summer dT_B evolution will be considered in our approach of snowmelt onset detection by locally-determined thresholds of dT_B .

Cross-polarized ratio XPR

Combining T_B at different frequencies and polarizations allows distinguishing different stages of the melt progress. Ashcraft and Long (2003) introduced ratios of T_B from various SSM/I channels to characterize surface and subsurface melt. The use of ratios has the advantage of reducing the effects of physical temperature changes. Their analyses reveal that the combination of the horizontally polarized brightness temperature at 19 GHz ($T_B(19H)$) and the vertically polarized brightness temperature at 37 GHz ($T_B(37V)$) is most sensitive to both surface and subsurface melt. In the context of the present paper this ratio is introduced as the cross-polarized ratio XPR:

$$XPR = T_B(19H) \cdot T_B(37V)^{-1}. \quad (4.2)$$

When melt water drains from the upper snowpack to deeper layers, the emissivity of the 19H channel increases and even exceeds the emissivity of the 37V channel (Abdalati and Steffen, 1997). Hence, the XPR can be used as indicator for snow soaked from above by melting water. Even though the studies by Abdalati and Steffen (1997) and Ashcraft and Long (2003) were performed on Greenland ice sheets, the microwave response to changes in surface snow properties can be assumed to be comparable to snow on (Antarctic) sea ice. However, for sea ice, one needs also to take into account a possible flooding of the snow/ice interface (e. g. in case of too heavy snow load) that influences the measured XPR value (see Section 4.4.1), and in some cases the influence of the sea ice below.

In Figure 4.1 two different regimes of XPR (orange curves) can be separated. One regime (locations 1, 4, 5, and 8) is characterized by XPR values less than 0.95 throughout the year indicating significant drops and rises with decreasing and increasing SIC. The second regime (locations 2, 3, 6, and 7) shows larger variations and XPR values that eventually exceed 1 between December and January. For Locations 3, 6, and 7 this XPR increase

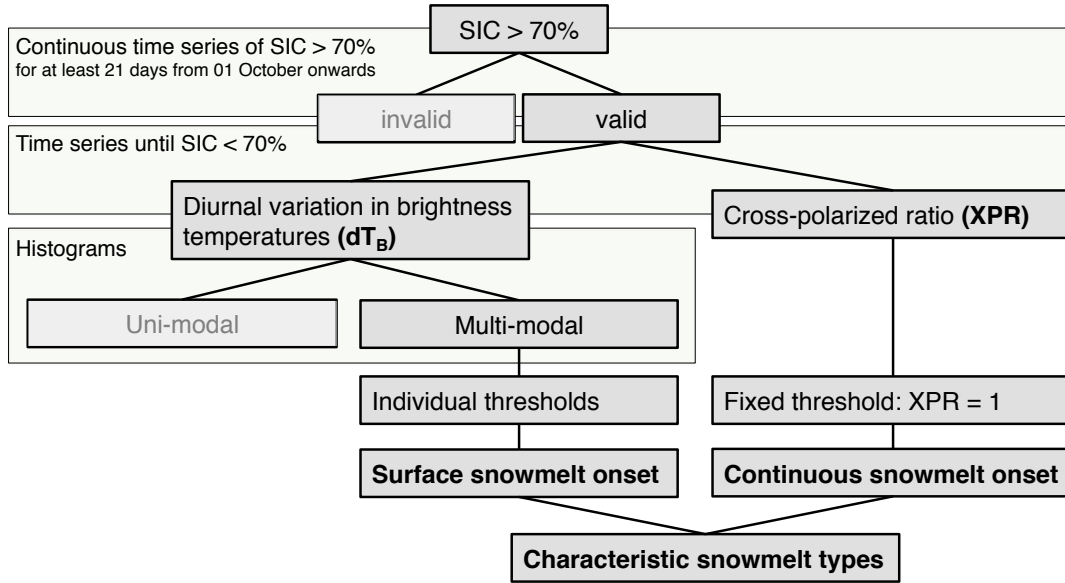


Figure 4.2: Flowchart of the snowmelt onset retrieval algorithm based on sea-ice concentration (SIC) and brightness temperature (T_B) data.

seems to be associated with an increasing dT_B . For Location 3, XPR exceeding 1 just occurs shortly before the strong increase of dT_B . In contrast, Location 2 reveals a sharp increase in XPR mid of January without preceding strong diurnal freeze-thaw cycles.

If the detected XPR values are above 1, the emissivity at 19H is larger than at 37V. We associate this with melt water draining into the lower snowpack and define a threshold of $XPR = 1$ as an indicator for the onset of continuous snowmelt on Antarctic sea ice.

Even though strong and continuous melt is rarely observed as stated by Willmes et al. (2009), we intend to use this parameter here to complement our observations of freeze-thaw cycles by identifying regions where continuous melt does in fact occur. Compared to the diurnal freeze-thaw cycles that mainly influence physical snow properties at the surface and thus, e.g., alter the amount of reflected and absorbed radiation (energy budget), the continuous snow melt might cause a loss in snow volume related to changes in the mass budget of the snowpack.

4.2.3 Melt transition retrieval

Figure 4.2 outlines the methodology to derive the timing of snowmelt onset with a regionally adaptive approach. We minimize the effects of open water on the T_B signal by including only grid cells where SIC is equal or larger than 70% for at least three weeks from 1 October onwards. The following analysis is applied for every grid cell until the sea-ice concentration drops once below 70%. In a next step, a 5-day running mean is applied to each grid-cell T_B time series. From the T_B data obtained at 37V, we calculate dT_B and

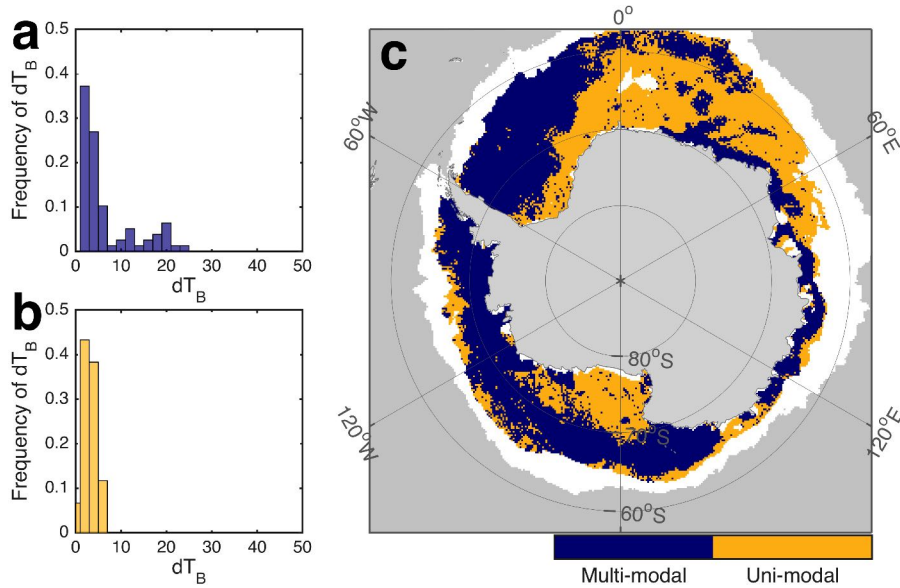


Figure 4.3: One example grid cell of (a) multi-modal and (b) uni-modal distribution of dT_B and (c) its spatial distribution for the example melt season 2004/2005. The histograms contain only values for sea-ice concentrations $> 70\%$ from 1 October to 31 January. The white areas indicate the maximum sea-ice area of the previous winter.

derive its histogram for each grid cell (bin width 2 K) over the expected melting season. An example is shown in Figure 4.3a and b. The derived histograms can be subdivided into uni-modal and multi-modal distributions. We define a mode as a local maximum bounded by at least one lower bin on each side. A multi-modal distribution has to reveal at least two of these modes. If a mode exceeds a proportion of 90% of all included data points, the distribution is defined as uni-modal. The multi-modal distributions (Figure 4.3a, c; blue) reflect the different melt stages of snow and the associated differences in freeze-thaw cycle strengths. Data points with a uni-modal distribution, and thus predominantly low dT_B values (Figure 4.3b, c; orange) are neglected in the analysis of diurnal freeze-thaw cycles, as they do not reveal the characteristic diurnal surface variations. In the next step, we define the individual dT_B -threshold criterion for the detection of temporary snowmelt applying an iterative threshold selection algorithm (Ridler and Calvard, 1978) to the pixels with multi-modal dT_B distribution. Finally, the *Temporary Snowmelt Onset* (TeSMO) is defined as the first time when dT_B exceeds the respective local threshold for at least 3 consecutive days during the expected melting season from 1 October to 31 January (e.g. Figure 4.4b).

The *Continuous Snowmelt Onset* (SMO) is detected independent of the previous described Temporary Snowmelt Onset. For its retrieval we apply the same SIC constraint as for the TeSMO (compare Figure 4.2). Again, a 5-day running mean is applied to each XPR time series, respectively, to reduce the effect of noise and outliers. Subsequently,

4 Timing and regional patterns of snowmelt on Antarctic sea ice

SMO can be determined in areas with an XPR exceeding 1 for at least 3 consecutive days. The first of the three days is interpreted as the day of melt onset. In case, we observe an earlier SMO than TeSMO, we neglect the later as we interpret it as a pre-melt stage of SMO (e.g. Location 3, Figure 4.1).

4.2.4 Data sets

Our analysis is based on the Level-3 Equal-Area Scalable Earth-Grid (EASE-Grid) Brightness Temperature data set, provided by the US National Snow and Ice Center (NSIDC) Armstrong et al. (1994). Daily brightness temperatures (T_B) at vertical and horizontal polarization are derived for July 1987 to June 2015 for 4 channels (19 GHz, 22 GHz, 37 GHz, and 85 GHz) from ascending and descending orbits on a 25-km grid. In our study we employed the 19 GHz and 37 GHz channels as explained above. During this period, data of four different SSM/I sensors were used: F8 from July 1987 to December 1991, F11 from December 1991 to 1995, F13 from May 1995 to December 2008, and F17 from December 2006 onwards. Willmes et al. (2009) specified the differences in dT_B during the overlap periods to be negligible. The reason is that dT_B represents a 12-hour variation of measured raw brightness temperatures and is therefore less sensitive to small inter-sensor differences between the ascending and descending nodes. All daily brightness temperature data are interpolated to a 25 km SSM/I polar stereographic grid, using nearest-neighbor resampling.

Bootstrap sea-ice concentration (SIC) data from Nimbus-7 SMMR and DMSP SSM/I-SSMIS Passive Microwave Data product were used to define the areas with $SIC > 70\%$ for which the algorithm is valid (Section 4.2.3) (Comiso, 2000). The data are available daily from late 1978 to 2014 on a 25 km SSM/I polar stereographic grid. During this period, the same four different SSM/I sensors were as for the brightness temperature data set (F8, F11, F13, F17) and can be used without any further inter-sensor adjustment (Comiso and Nishio, 2008). The time period from January 2015 onward is covered by the near-real-time DMSP SSMIS Daily Polar Gridded Sea Ice Concentration data product (Maslanik and Stroeve, 1999).

4.3 Results

4.3.1 Spatial variability of snowmelt patterns

Figure 4.4 shows the obtained individual dT_B transition thresholds (Figure 4.4a) and the associated Temporary Snowmelt Onset (TeSMO, Figure 4.4b) as well as the Continuous Snowmelt Onset (SMO, Figure 4.4c) for the melt season 2004/2005, respectively. The example year of 2004/2005 was chosen to ensure the best possible comparison with the previous study by Willmes et al. (2009). The white areas cover the previous winter's maximum sea-ice extent, and indicate locations that do not fulfill the requirements for

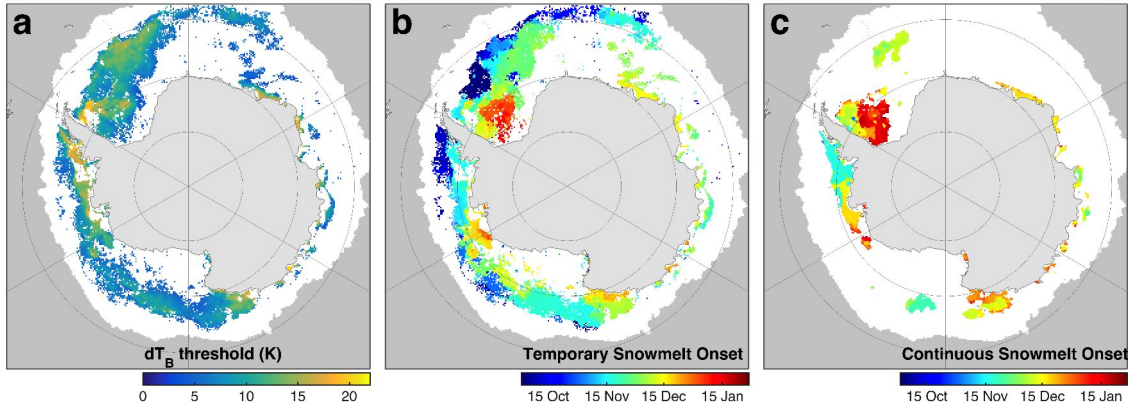


Figure 4.4: (a) Individual transition threshold dT_B , (b) Temporary Snowmelt Onset, and (c) Continuous Snowmelt Onset for the melt transition 2004/2005. The white areas indicate the maximal sea-ice-covered area of the previous winter.

melt-onset detection (Section 4.2.3). For the following description and analysis, we divided the Antarctic sea-ice area in five areas: Indian Ocean (20°E to 90°E), Western Pacific Ocean (90°E to 160°E), Ross Sea (160°E to 130°W), Bellingshausen and Amundsen Seas (130°W to 60°W), and Weddell Sea (60°W to 20°E) (Gloersen et al., 1992) (Figure 2.5).

The individual transition thresholds dT_B cover a range from 3 to 22 K with a modal value of 6 K and a mean of 8.9 ± 3.6 K for the melt season 2004/2005. The distribution of dT_B thresholds shows substantial spatial variability. The Ross Sea tends to have lowest thresholds, between 3 and 10 K, indicating least pronounced melt-freeze cycles. Also parts of the eastern Weddell Sea and pack ice area in the Indian Ocean reveal low dT_B values. In contrast, the highest transition thresholds (up to 22 K) are found in the Amundsen and Weddell Seas. In addition, high dT_B values are common for most of the land-fast sea ice on the coast of East Antarctica.

Based on these individual thresholds, the derived TeSMO shows a latitudinal dependence, with an earlier melt onset in the marginal sea-ice zone, and melt spreading southwards as the summer progresses. During the melt season 2004/2005, the average TeSMO for the entire Antarctic occurred on 20 November, ranging from 10 November in the Bellingshausen and Amundsen Seas to 5 December in the Western Pacific Ocean. The latest TeSMOs occurred in the southwestern Weddell Sea and at the coast of the eastern Ross Sea in the beginning of January. The latitudinal dependence of SMO is difficult to analyze because of the relatively small areas affected by this type of melt. The regional dependence might be connected to local weather phenomena as well as peculiarities in snow and ice properties. During the melt season 2004/2005, SMO occurred, on average, 17 days later than TeSMO, in an interval from 30 November (Bellingshausen and Amundsen Seas) to 23 December (Weddell Sea). Spatial variations in the derived local thresholds and retrieved melt onset dates are discussed in Section 4.4.1.

4 Timing and regional patterns of snowmelt on Antarctic sea ice

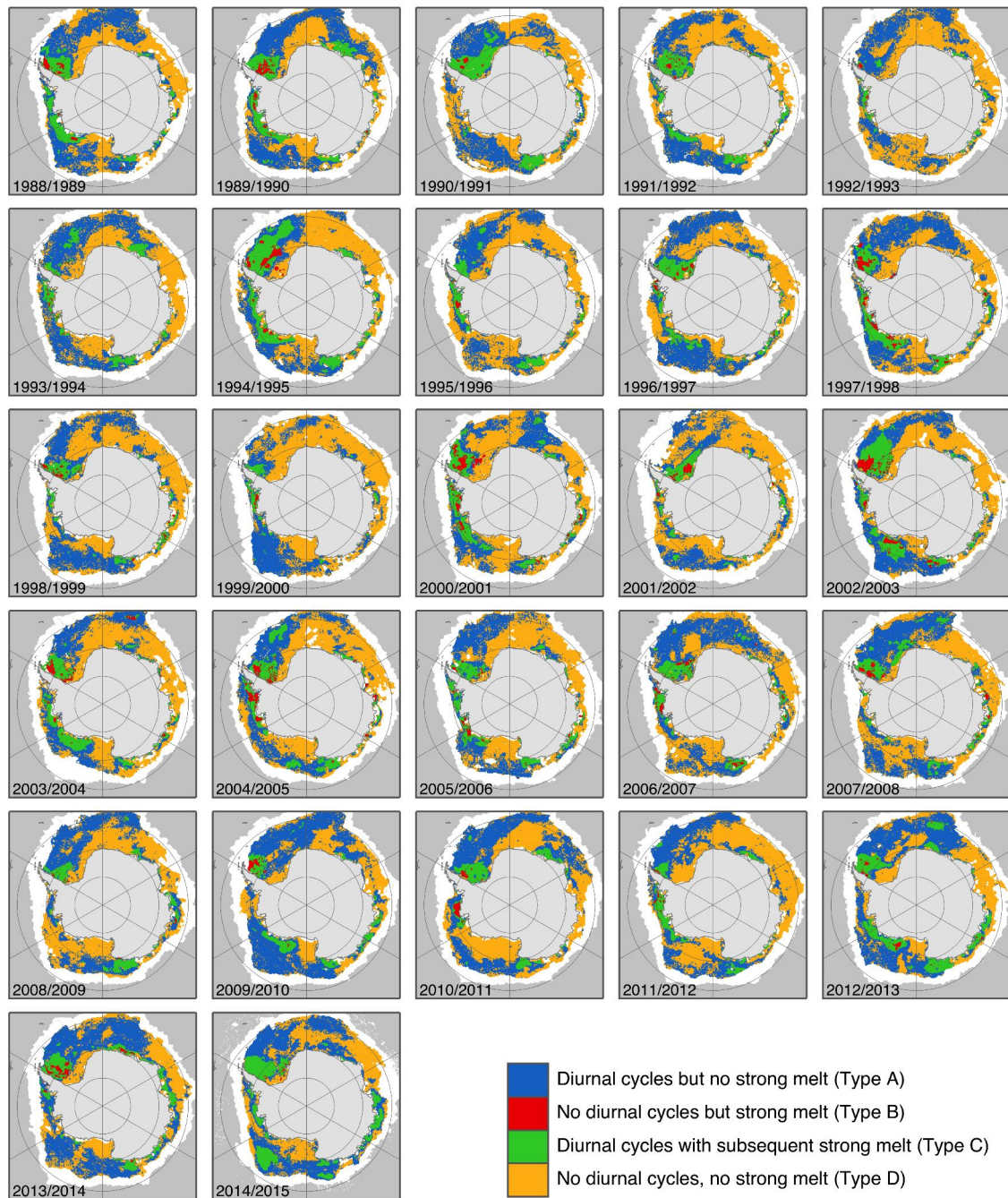


Figure 4.5: Classification of Antarctic sea ice into four characteristic snowmelt types for the seasons from 1988/1989 to 2014/2015. The white color represent unclassified zones, and indicates the maximal sea-ice-covered area of the previous winter.

4.3.2 Characteristic regions and surface melt types

To link the two stages of snowmelt onset described above with different snow surface characteristics of Antarctic sea ice, we distinguish four ice zones based on their typical

melt signatures (Figure 4.5): diurnal freeze-thaw cycles in the surface snow layer only (Type A), immediate continuous snowmelt throughout the snowpack (Type B), diurnal surface freeze-thaw cycles followed by continuous melt (Type C), and no observed melt at all (Type D). A fifth category is marked as “not classified” (Figure 4.5, white areas). The results are shown for each year of the available time series from 1988/1989 to 2014/2015.

On average, about 12% of the classified sea-ice area reveals diurnal freeze-thaw cycles with subsequent continuous melt (Figure 4.5, Type C: green). This surface type prevails in the western Weddell Sea, the eastern West Pacific sector, and on the land-fast sea ice in the East Antarctic. It is characterized by freeze-thaw cycles at the surface resulting in melt water penetration to deeper layers, which eventually soaks the entire snowpack

Areas with freeze-thaw cycles starting early in the season, but without a subsequent detection of continuous melt, are observed in the outflow area of the Weddell Gyre in the northern Weddell Sea, as well as in the northern Amundsen and Ross Seas (Figure 4.5, Type A: blue). This surface type usually has early and weak surface melt and dominates the Antarctic sea-ice area covering about 39% of the classified sea-ice area.

Unlike the two latter surface types, where we observe at least short periods of characteristic freeze-thaw cycles during summer, small areas of the Antarctic sea ice (less than 2%) reveal continuous melt with no refreezing events (Figure 4.5, Type B: red) or delayed increase in freeze-thaw cycles compared to the continuous (deep) melt onset (Figure 4.1, Location 3).

Major parts of the Indian and Western Pacific Oceans, as well as the southeastern Weddell Sea and central Ross Sea (in total 48% of the classified sea-ice area), reveal neither diurnal freeze-thaw cycles at the snow surface nor continuous melt (Figure 4.5, Type D: yellow). Some of these sea-ice regions may already disintegrate by break-up or lateral and bottom melt, before significant surface melt can take place. In others of these regions, our detection criteria may not be sufficiently sensitive to possible melt onset.

The eastern Weddell Sea is dominated by the pre-dominant clockwise sea-ice drift related to the Weddell Gyre (Schmitt et al., 2004) and the interaction with the adjacent Filchner Trough (Nicholls et al., 2009). The southern Ross Sea is most commonly affected by katabatic winds from the shelf ice leading to the formation of the coastal Ross Sea Polynya. These interactions between ocean, sea ice and atmosphere lead for both the Weddell and Ross Sea to a repeated formation of new thin ice (Smith et al., 1990). Consequently, these areas of newly formed ice are snow-free, or are covered only by a thin snow layer. Thus, the received microwave signal is dominated by the sea-ice surface and its characteristics. Also the highly dynamic ice conditions due to the sea-ice production in these regions prevent the detection of melt based on dT_B and XPR.

The surface and snow layer properties of large areas of pack ice in the Indian and Western Pacific Oceans are affected by a highly dynamic ice regime and the thin snowpack (less than 20 cm, Worby et al. (2008)). The marginal ice zone is dominated by formation of ice and the penetration of ocean waves into the ice. Snow layers are thin and may get wet

4 Timing and regional patterns of snowmelt on Antarctic sea ice

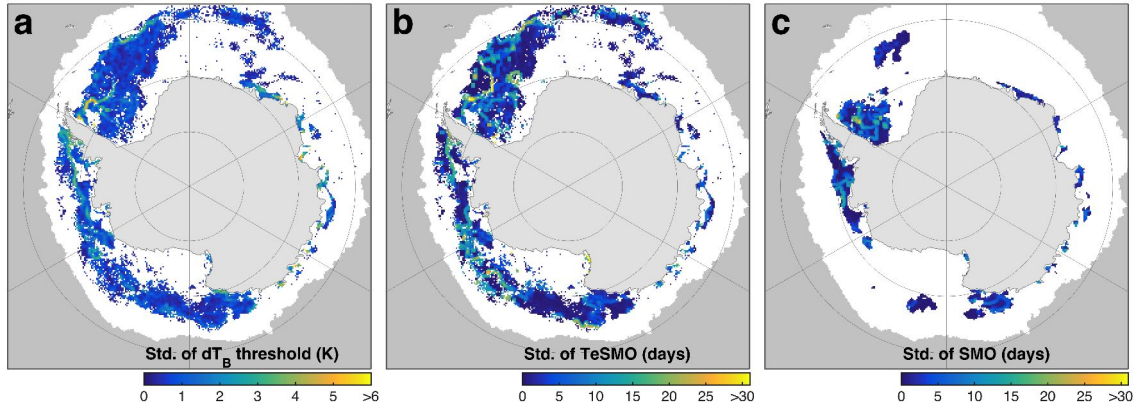


Figure 4.6: Derived standard deviations (Std.) derived from overlapping windows of 3×3 cells for (a) the individual transition threshold dT_B , (b) the Temporary Snowmelt Onset (TeSMO), and (c) the Continuous Snowmelt Onset (SMO) for the melt transition 2004/2005. The white areas indicate the maximal sea-ice-covered area of the previous winter.

due to potential flooding caused by the penetrating ocean waves. In some cases, the snow may be heavy enough to lower the ice surface below water level. Hence, also in this case, the use of dT_B and XPR is not suitable for the detection of melt onset (see Type D). In addition, the marginal ice zone is influenced by the Antarctic Circumpolar Current, which causes continuous sea-ice divergence and disintegration, resulting in enhanced bottom and lateral melt in the area once the cooling from the atmosphere has finished.

4.4 Discussion

4.4.1 Limitations and uncertainties

The spatial homogeneity of melt patterns is derived from the standard deviation of a grid cell and its eight neighbors (i.e. in an overlapping window of 3×3 cells) for the data products dT_B threshold, TeSMO, and SMO (see Figure 4.6). This approach gives a measure for local signature variations in an area of 75-by-75 km. As possible reasons for variations, we consider also small-scale snowdrift and sea-ice drift in addition to different snow properties and ice conditions (e.g. sea-ice age classes). The influence of sea-ice drift is not included in our approach, since no adequate data products are existent. However, if these data would be available, we expect improvements primarily in the marginal ice zones and less for the inner pack ice.

For the example year of 2004/2005, the mean variation of TeSMO over the 3×3 grid cell boxes is 4.5 days, with 69 % of all variations smaller or equal to 5 days and a modal value of 1 day (Figure 4.6b). The respective dT_B threshold reveals a mean spatial variation of 0.9 K (Figure 4.6a) whereas the modal value is between 0.5 and 0.6 K. The highest variations

in TeSMO and dT_B (up to 30 days/ 6.3K) are found between zones of different melt regimes in the Weddell Sea (Figure 4.4 and 4.5). Spatial variations of SMO show a mean of 3.6 days, with 52 % of all derived variations smaller or equal to 2 days (Figure 4.6c).

The more heterogeneous distribution of TeSMO compared to SMO may be linked with the sensitivity of both parameters to snow depths: Because of the smaller penetration depth of the 37 GHz channel, the retrieval of TeSMO is more strongly affected by localized processes on the snow surface, such as for instance snow drift, whereas SMO, which is derived from the XPR including the 19 GHz brightness temperature, is influenced by the deeper snow layers, where continuous snowmelt is mainly triggered by solar radiation and related cloud effects (i.e. changes in long-wave radiation) which is spatially less variable than, e. g., snow drift patterns on the surface.

We assume that the observed TeSMO and SMO patterns indicate the influence of a number of different snow and ice parameters (e.g. sea-ice/snow age), and processes. The sea-ice concentration range that we accept for our retrievals varies between 70 % and 100 %. Due to the ice drift, the distribution of open water and sea ice in a given area changes within hours to days. The drift causes also a re-distribution of snow zones with different properties (e. g. depth). In addition we have to consider the uncertainties in the retrieval of the melt onset (see below).

An overall quantification of uncertainties of the presented method is not possible, since measurements providing daily air temperatures close to the snow/ice surface are not available. Since our method requires that dT_B and XPR exceed their respective threshold for at least three consecutive days, we might miss shorter melt events actually taking place earlier. This discrepancy may account for several days in the worst case.

Moreover, the brightness temperature and the retrieved melt onset data may be biased due to the presence of open water areas. Table 4.1 gives an overview about the influence of the chosen threshold in sea-ice concentration on the retrieved TeSMO and SMO. Since open water blurs the microwave signal and thus, e.g. diminishes the diurnal variations at the snow surface, the defined melt criteria are fulfilled slightly later in areas of less sea-ice concentration. Thus, we can conclude from this sensitivity study that areas of sea-ice concentration close to 70 % may be biased towards a later melt onset, whereas in completely ice-covered areas an earlier melt onset can be expected. Overall, the Bellingshausen and Amundsen Seas show the highest influence of the chosen sea-ice concentration threshold on the derived melt onset dates with a difference of up to 7 days in the presented study (Table 4.1), which might be connected to the comparable narrow and highly variable sea-ice band in the area. Taken the entire Antarctic sea-ice area into account, the influence is rather small since TeSMO and SMO vary by 1 and 4 day(s), respectively.

Another limiting factor of the presented study is flooding of Antarctic sea ice. In our retrieval of melt onset, we do not consider situations in which a relatively thick snow cover on relatively thin ice may lead to a negative freeboard and thus, to flooding of the ice. While the bottom snow layer is soaked with water, the snow surface, and thus the detection

4 Timing and regional patterns of snowmelt on Antarctic sea ice

Table 4.1: Sensitivity study on different sea-ice concentration thresholds for the retrieval Temporary Snowmelt Onset (TeSMO) and Continuous Snowmelt Onset (SMO) for the melt transition 2004/2005. Numbers are given as the spatial mean for the respective region (days after 1 October). Calculations were only performed for grid cells, which are covered by the analysis for all five sea-ice concentration thresholds.

Sea-ice concentration >	TeSMO/SMO (Days after 1 Oct)				
	50 %	60 %	70 %	80 %	90 %
Indian Ocean	52/78	51/77	51/76	51/75	50/75
Western Pacific Ocean	71/81	71/80	71/79	71/77	70/76
Ross Sea	49/70	49/69	48/68	48/67	46/63
Bellingshausen and Amundsen Seas	42/63	42/62	41/61	39/59	36/56
Weddell Sea	61/84	61/84	60/84	60/84	58/84
All areas	56/76	56/76	54/75	54/75	52/75

of temporary snowmelt, may still be unaffected. Nevertheless, as the penetration depth of microwave signals at 37 GHz is up to 50 cm for dry snow (Garrity, 1992), the soaked bottom layer may lead to changes in the brightness temperatures, which would result in the retrieval of (continuous) snowmelt onset dates that are too early.

4.4.2 Comparison of surface melt patterns with field data and previous studies

Comparison with autonomous measuring systems

A validation of the characteristic surface patterns (Figure 4.5) and their spatial variability (Figure 4.4) with field observations is almost impossible since field data with adequate spatial and temporal resolution and coverage are not available. Alternatively, comparisons with numerical simulations of snow cover properties could be performed, but currently no reliable simulations of snow properties and snow depth evolutions are available for the Weddell Sea. Here, we compare data from autonomous Snow Buoys to assess our results at least for parts of the Weddell Sea during summer 2014/2015, when these data are available.

Snow Buoys (Met Ocean, Canada) are autonomous platforms deployed on sea ice. Four ultra sonic sensors measure the distance to the snow surface that is then transformed to snow depth. In addition, each buoy measures air temperature and surface pressure. Here, we use data from four of these Snow Buoys: 2014S9, 2014S10, 2014S11, and 2014S12 (hereafter only S9 to S12, <http://data.seaiceportal.de/>). The buoys were deployed in the southern Weddell Sea in January/February 2014, and obtained continuous and consistent

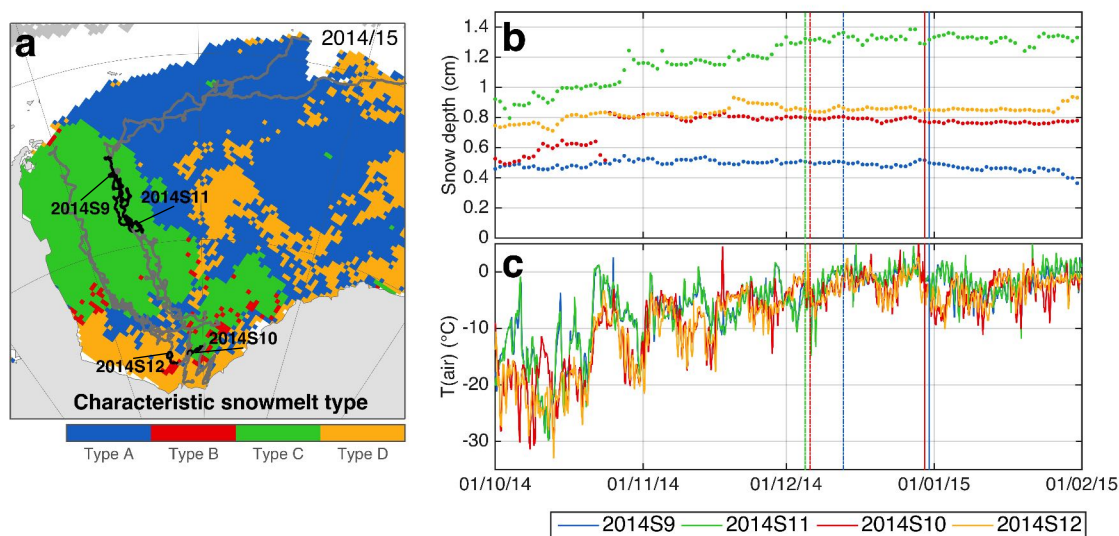


Figure 4.7: (a) Snow Buoy tracks plotted on the characteristic snowmelt type for the melt transition 2014/2015. The black segments indicate the buoy drift during the expected melt season 2014/2015 (1 October 2014 to 31 January 2015), while the grey parts show the drift patterns during the freezing season. (b) Daily averaged snow depth, and (c) air temperature for all four buoys during the expected melt season 2014/2015. Dotted vertical lines indicate the extracted TeSMO, solid lines the extracted SMO for the respective buoys.

measurements all through the austral summer 2014/2015. Figure 4.7a shows the drift trajectories of all four buoys, also indicating the regional spread of the measurements due to the individual drift trajectories. The black segments represent the drift path during the melt season 2014/2015, from October 2014 to January 2015. To our knowledge, this data set is the only one showing temporal changes of snow conditions over an entire summer, simultaneously for different locations in the Southern Ocean. Nearest-neighbor grid points of the daily buoy positions were extracted from our snowmelt data sets (TeSMO and SMO) for the following comparison. Snow depths from the buoys are given as a daily average of all four sensors of the respective buoy (Figure 4.7b).

Comparing all four buoys, differences between S10 and S12, located in the southeastern Weddell Sea during summer 2014/2015, and S09 and S11, drifting through the northwestern Weddell Sea during summer, become obvious. S9 and S11 stay in an area of temporary melt at the snow surface with subsequent continuous melt (Figure 4.7a, Type C, green), whereas the surrounding of buoy S12 is supposed to have neither temporary melt nor continuous deep melt (Type D, yellow). The surface characteristics in the surrounding sea-ice area of S10 are quite patchy and do therefore allow only for the determination of temporary melt for the buoy from our analysis (05 December 2014, Figure 4.7b,c, dotted vertical line).

4 Timing and regional patterns of snowmelt on Antarctic sea ice

While the air temperatures of S9 and S11 exceed 0°C in the end of December as well as the end of January (Figure 4.7c), the snow depth measurements indicate no significant snow loss during the expected melt period (Figure 4.7b): The snow depth at S09 is stable around 0.5 m until the continuous snowmelt (SMO) is detected and it decreases by approximately 0.1 m, whereas snow depth at S11 increases until the beginning of temporary melt (TeSMO) and afterwards varies around the seasonal maximum of 1.3 m. In contrast, S10 shows an increase until mid of October (mainly due to one strong snow fall event of 20 cm) and thereafter very stable snow conditions around 0.8 m, whereas S12 reveals a generally low variability in snow depth over the entire melt period between 0.7 and 0.9 m.

Generally, air temperatures above the freezing point become more dominant after the detected temporary melt onsets for the respective buoys. The apparent change between thawing (temperatures above the freezing point) and re-freezing (temperatures below the freezing points) is the main characteristic of the described temporary melt.

Considering both, the characteristic snowmelt type and the time series of snow depth and air temperature for all four buoys, we notice that also continuous (deep) snowmelt is not necessarily associated with an immediate decreasing snow depth. In the vicinity of buoy S9 and S11, we expect perennial sea ice (Nghiem et al., 2016) and thus a multi-year snowpack on top. The latter is characterized by layers of highly compacted and metamorphic snow with internal ice layers (Nicolaus et al., 2009). If the described continuous melt onsets and thus the liquid water content in the deeper snowpack increases, the compacted layers of the multi-year snowpack are stable enough to prevent a drop in snow depth. Thus, changing physical properties of snow on Antarctic sea ice related to the onset of melt processes do not necessarily translate into changes in snow depth.

Comparison with previous studies

Instead of using fixed thresholds for the diurnal brightness temperature variations, as suggested by Willmes et al. (2009), our study on surface snowmelt onset retrieval is based on local transition thresholds. Despite this major difference, both studies reveal a comparable latitudinal sequence of snowmelt onsets, from early onset (mid of October) in the marginal ice zone to a later onset (mid January) in the south (Figure 4.4, Section 4.3.1). On average, our Temporary Snowmelt Onset (TeSMO) is 16 days earlier than the one found by Willmes et al. (2009). The difference is due to fixing the threshold to 10 K, which is significantly higher than the median threshold of 6 K in our study. Thus, Willmes et al. (2009) detect surface melt only after several freeze-thaw cycles and significant metamorphism of the snowpack.

Studies on scatterometer data, e.g. by Haas (2001), reveal areas of strong intensities of the backscattered radar signal, associated with the formation of superimposed ice on perennial sea ice. These occur mainly in the northwestern Weddell Sea (67 to 69°S / 51 to 57°W), in the coastal area of Bellingshausen Sea (e.g. 71.3°S / 95.3°W) as well as in the east-

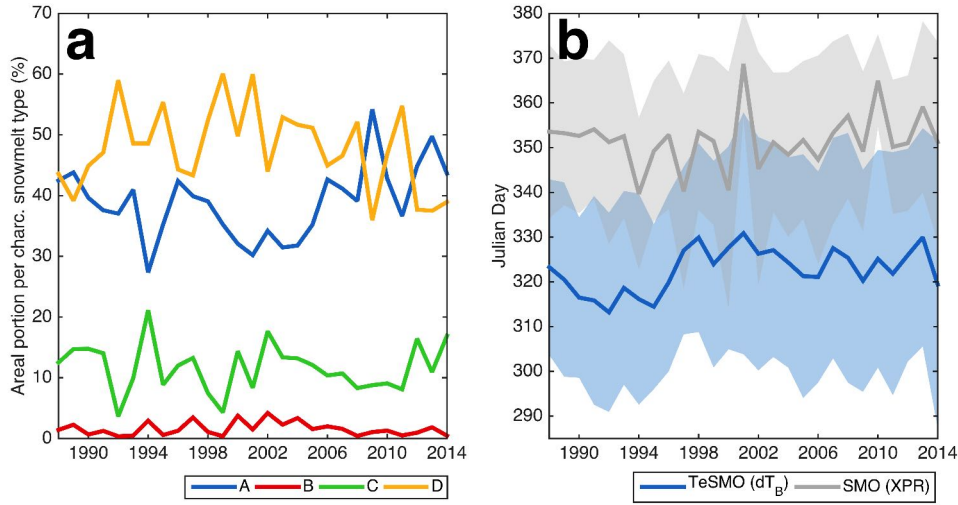


Figure 4.8: (a) Extent of melt types, as classified in this study (Figure 4.5, Section 4.3.2): Type A: Diurnal cycles but no continuous melt. Type B: No diurnal cycles but continuous melt. Type C: Diurnal cycles with subsequent continuous melt. Type D: No diurnal cycles and no continuous melt. (b) Dates of Temporary Snowmelt Onset (TeSMO) and Continuous Snowmelt Onset (SMO). Solid lines: Antarctic-wide mean, shaded area: Antarctic-wide standard deviation.

ern Ross Sea (67.5 to 68.5°S/ 152 to 157°W). Superimposed ice forms due to enhanced snowmelt and saturation of snow with melt water, but also flooding of sea ice might contribute to superimposed ice formation. Our analysis reveals that diurnal freeze-thaw cycles with subsequent melt in deeper snow layers (Figure 4.5) prevail for the areas in which the pronounced rise of the backscattering is observed by Haas (2001). Thus, our results support the assumption that in the areas mentioned above, continuous snowmelt causes melt water percolation and formation of superimposed ice.

4.4.3 Decadal variability of snowmelt patterns

We consider the main advantage of our results in the fact that they provide a large-scale overview on the spatial distribution and frequency of the different types of snow melt onset on Antarctic sea ice. Previous studies of changes in the Antarctic sea-ice area indicate an overall increase in sea-ice extent (SIE) since the late 1970s (Cavaliere and Parkinson, 2008; Stammerjohn et al., 2012; Turner et al., 2015; Zwally et al., 2002). However, one needs to consider regional differences. On average, SIE increased by 3.9% per decade in the Ross Sea whereas a decrease of 3.4% per decade is observed in the Bellingshausen and Amundsen Seas (Turner et al., 2015). These differences are associated with alterations in ice season duration (time period between sea-ice advance and retreat) (Stammerjohn et al., 2012): since 1979/1980, the Ross Sea ice season has lengthened by 25 ± 4 days whereas the Bellingshausen and Amundsen Sea ice season has decreased by 31 ± 10 days.

4 Timing and regional patterns of snowmelt on Antarctic sea ice

Averaged over all Antarctic sea ice, the seasonal sea-ice regime indicates that the ice season is getting longer by up to 20 days per decade.

Figure 4.8a shows the time series of the spatial extent of the different surface melt types observed from 1988/1989 to 2014/2015, as described above. All four types have no significant trend, but a large inter-annual variability. The highest range of variation of up to 25% in the areal proportion per snowmelt type is observed for areas with diurnal freeze-thaw cycles but no strong melt (Type A, blue) and areas revealing neither diurnal freeze-thaw cycles at the snow surface nor continuous melt (Type D, yellow).

The temporal evolution of TeSMO and SMO does also show no significant trend (Figure 4.8b). During the entire period of 27 years, the average TeSMO for the entire Antarctic occurred on 16 November, ranging from 9 November (2009) to 26 November (2001).

Thus, there is no direct link between snowmelt processes and the temporal evolution of sea-ice concentration and extent during the last decades. Instead, variations in weather patterns (Matear et al., 2015; Nghiem et al., 2016) during spring might well pre-condition the snow surface and processes in deeper snow layers (e.g. snow metamorphism) leading to an either accelerated or delayed melt progress. Consequently, we see, e.g., in the southern Weddell Sea a clear transition between areas of diurnal freeze-thaw cycles with subsequent continuous melt (Figure 4.5, Type C, green) in the western part and areas with neither temporary nor continuous melt (Type D, yellow) in the eastern part for most of the time whereas Type D is almost completely absent for 1990/1991, 1996/1997, 2001/2002 and 2010/2011.

4.5 Summary and Conclusions

We developed a new method to detect snowmelt on Antarctic sea ice, which is based on using individual local thresholds applied to the diurnal variation dT_B of the microwave brightness temperatures at 37 GHz (temporary snowmelt onset). We use the cross-polarized ratio (XPR) that combines brightness temperatures at 37 GHz V-polarization and 19 GHz H-polarization to generate a complementary data set of intermittent and continuous melt onset. These melt onset indicators are applied to determine characteristic surface melt patterns on Antarctic sea ice.

Our analysis reveals four surface regimes with substantial differences in their melt characteristics: (Type A) $38.9 \pm 6.0\%$ of all detected melt events are characterized by diurnal freeze-thaw cycles resulting in temporary surface snowmelt but no continuous melt; (Type B) less than 2% reveal continuous melt only; (Type C) $11.7 \pm 4.0\%$ of all events reveal diurnal surface freeze-thaw cycles leading to subsequent continuous strong melt; (Type D) for $47.8 \pm 6.8\%$ no significant temporary or continuous surface melt characteristics are observed at all. Areas characterized by freeze-thaw cycles are more extensive than areas of continuous melt.

The retrieved melt onset dates using per-pixel thresholds consider regional differences

in the amplitudes of diurnal freeze-thaw cycles connected to different snow surface properties during the spring-summer transition. With our flexible transition threshold and its modal value of 6 K, compared to the fixed threshold of 10 K by Willmes et al. (2006), we enable to detect the first occurrence of temporary surface melt, which might be missed to some extent by the fixed-threshold algorithm. The results of the new algorithm are compared with snow depth data from autonomous monitoring systems (snow buoys) drifting through the Weddell Sea during spring-summer transition 2014/2015. The results show uncertainties in the local point-to-point comparison due to, e.g. local snowdrift events and snow metamorphism, whereas snowmelt processes on a broad-scale (i.e. 100-1000 km) can be described by the retrieved melt onset data products.

We apply our algorithm for deriving spatial distributions of the different surface melt types on an SSM/I time series from 1988/1989 to 2014/2015, and determine decadal variabilities in the timing of the melt onsets for freeze-thaw cycles and for continuous snow melt. Previous studies have shown an increasing sea-ice extent, sea-ice concentration, and ice season duration in certain regions of the Antarctic sea ice during the last decades (Stammerjohn et al., 2012; Turner et al., 2015), whereas the spatial extent of the four different surface types and the derived melt onset dates do show strong inter-annual variations but no significant trend between 1988/1989 and 2014/2015.

Since diurnal freeze-thaw cycles cause rounding and growth of snow grains (Willmes et al., 2009), their onset has a major impact on local optical properties of the snow surface, e.g. albedo and absorption, and thus on the energy budget of Antarctic sea ice. The newly derived continuous snowmelt onset has important implications for the estimation of the sea-ice mass budget. Our analysis indicates that continuous snowmelt takes place often in areas with superimposed-ice formation (Haas, 2001). As superimposed ice significantly contributes to the sea-ice mass balance (Eicken et al., 1994; Haas et al., 2001), our derived data product of the continuous snowmelt onset (types B and C) may be helpful for delimiting positions and extent of superimposed ice formation. The comparison with Snow Buoy data suggests that also continuous melt processes in the perennial snowpack does not necessarily translate into changes in snow depth but might rather affect the internal stratigraphy and density structure of the snowpack.

The presence of liquid water in the snowpack has an impact on sea-ice concentration retrieval (e.g. Comiso et al., 1992), and limits snow depth retrieval based on microwave radiometry (Cavalieri et al., 2012).

5

Retrieval of seasonal snowmelt stages on Antarctic sea ice from satellite scatterometer observations

Results of the previous chapter identify major melt characteristics in the upper Antarctic snowpack retrieved from passive microwave satellite observations. It is shown that the temporary snowmelt is driven by diurnal thawing and refreezing at the snow surface, while continuous melt is rarely observed in deeper layers.

In this chapter, in order to resolve also seasonal melt stages in the lower snowpack and at the snow/ice interface, a similar snowmelt onset retrieval method as for the passive microwave satellite observations is applied to satellite scatterometer observations. Data from the satellites ERS-1/2, ASCAT and QSCAT are merged to provide a decent time series. Combining the results of this study with the achievements from passive microwave satellite observations enables to determine different processes modifying the physical properties of the whole snow column, which are relevant for an improved understanding and quantification of observed changes in the energy and mass budgets of Antarctic sea ice.

5.1 Introduction

The sea-ice cover in the Southern Ocean experienced large seasonal and inter-annual changes during the last decades (Parkinson and Cavalieri, 2012; Stammerjohn et al., 2012; Turner et al., 2015). The strong seasonal variability has a crucial impact on processes and interactions between atmosphere, sea ice and ocean, and is therefore a key component driving the polar marine ecosystem (Massom and Stammerjohn, 2010). The presence of snow on the ice dramatically alters these exchange processes (Massom et al., 2001). As Antarctic sea ice is snow-covered throughout the summer, the seasonal transition from freezing to melting conditions, and vice versa, strongly affects the snow properties and snow volume (Massom et al., 2001; Jeffries et al., 1997). The widely thick snowpack depresses the sea ice below the water level resulting in potential surface flooding and subsequent refreezing of slush at the snow/ice interface (Eicken et al., 1994; Haas et al., 2001; Nicolaus et al., 2009). This process is referred to as flood-freeze cycling (Fritsen et al., 1998) leading to the formation of snow-ice which, however, contributes significantly to the sea-ice mass budget of particularly first-year ice in the Southern Ocean (Eicken et al., 1994, 1995; Haas et al.,

5 Seasonal snowmelt from scatterometer observations

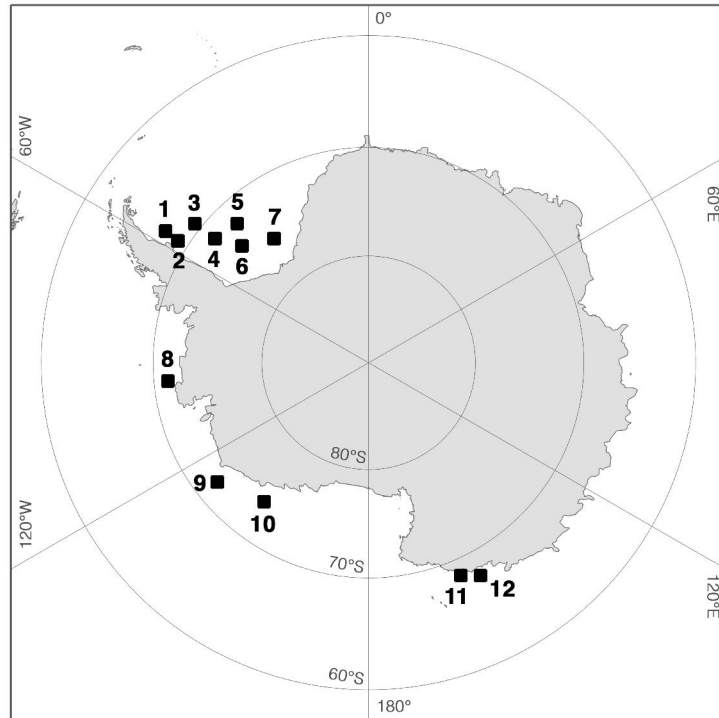


Figure 5.1: Map of the Antarctic showing the 12 study locations on perennial sea ice according to Haas (2001).

2001; Jeffries et al., 1997; Nicolaus et al., 2009). In addition, diurnal freeze-thaw cycles in the upper snow layer and subsurface snowmelt processes initiate the percolation of (fresh) melt water through the snowpack, and thus the subsequent formation of superimposed ice at the snow/ice interface (Arndt et al., 2016; Haas et al., 2001, 2008; Nicolaus et al., 2009; Willmes et al., 2009).

Microwave observations are sensitive to the dielectric properties of sea ice and snow, related to the changing amount of liquid water in the entire column, and thus to the described melt processes of the prevalent snowpack (Arndt et al., 2016; Haas et al., 2001, 2008; Nicolaus et al., 2009; Willmes et al., 2009). Therefore, passive microwave instruments, such as the Special Sensor Microwave/Imager (SSM/I), have been utilized to retrieve intermittent and continuous snowmelt in upper snow layers during the spring-summer transition on Antarctic sea ice (Arndt et al., 2016; Eppler et al., 1992; Willmes et al., 2006, 2009). Since the studies are based on satellite observations at frequencies between 19 and 37 GHz, they are assumed to detect changes in the upper snowpack.

In contrast, scatterometer observations at lower frequencies allow resolving seasonal changes of physical properties in deeper snow layers or rather at the snow/ice interface (Haas, 2001). Since snow metamorphism initiates the change towards large-grained, polyg-

5.2 Snowmelt retrieval from satellite scatterometer data

onal granular textured and salt-free (snow) grains, the microwave volume- and surface scattering intensity of the sea-ice surface significantly increases (Colbeck, 1997; Onstott and Shuchman, 2004). Thus, studying primarily perennial sea ice, Haas (2001) related the seasonal cycle of the sea-ice radar backscatter (σ^0) in most of the chosen regions to the widespread occurrence of superimposed ice formation. However, the study is restricted to the time period between 1991 and 1999 and only 12 regions on perennial sea ice (Figure 5.1).

It is therefore the aim of this study to extend not only the existing time series but also the spatial coverage of the retrieval of snowmelt stages in the lower snowpack. To do this, an Antarctic-wide analysis of the seasonal cycle of backscatter signatures is performed, obtaining both, the distinct backscatter spring rise and potentially preceding temporal rises indicating the initial thaw stage in the lower snowpack or even at the snow/ice interface. From the previous study, the described backscatter rise is reported predominantly on perennial sea ice. Since no adequate sea-ice type data product is available so far, one must assume large uncertainties from the given approach in areas of expected seasonal sea ice. To quantify those, the retrieved snowmelt onsets are compared with snowmelt onset dates in the upper snowpack, retrieved from passive microwave observations. Moreover, combining both melt retrievals allows to describe seasonal evolution of snow properties throughout the vertical profile of the snowpack.

To study also long-term variabilities in the lower snowpack, scatterometer data from the European Remote Sensing (ERS)-1/2 platforms and the subsequent missions of QuikSCAT (QSCAT) and the Advanced Scatterometer (ASCAT) are combined to provide a time series from 1992 to 2015. Since the instruments differ in particular in their signal frequencies (ERS-1/2 and ASCAT: 5.3 GHz; QSCAT: 13.4 GHz), an additional comparison of the respective overlap periods is performed and discussed.

The identification of different snowmelt stages in the upper and lower snowpack can contribute to an improved quantification of the energy and mass budget changes of the ice-covered Southern Ocean. The knowledge gain on expected layering due to inner snow transition and melt processes might also increase the understanding of the uncertainty and variability of space-borne retrievals of sea-ice concentration, snow depth and sea-ice thickness.

5.2 Snowmelt retrieval from satellite scatterometer data

5.2.1 Data sets

All presented data sets were obtained from the NASA Scatterometer Climate Record Pathfinder (SCP) project, sponsored by NASA (<http://www.scp.byu.edu/>). For the following analysis, all data are interpolated to a 25 km SSM/I polar stereographic grid, using nearest-neighbor resampling.

The scatterometer data from the European Remote Sensing (ERS)-1/2 platforms are 6-day averages of vertical co-polarized C-Band (5.3 GHz, wavelength of 5.7 cm) backscatter in order to cover the polar oceans and maintain a reasonable stability of the successive backscatter map (Ezraty and Cavanié, 1999). The backscatter is normalized to an incident angle of 40° and is projected onto a polar stereographic grid with a pixel size of about 25 km-by-25 km across the swath width of about 500 km. ERS-1 was operational from 1991 to 1996, while ERS-2 continued the time series until 2001.

The subsequent mission of QuikSCAT (QSCAT) acquired measurements from 1999 to 2009. Compared to the ERS missions, QSCAT operated in higher frequencies (13.4 GHz, Ku-Band), equivalent to shorter wavelengths (2.2 cm). In this study, the QSCAT product is utilized using all passes in both polarizations (vertically and horizontally co-polarized) normalized to a 40° incident angle (Scatterometer Image Reconstruction, SIR, Long et al. (1993)). The SIR algorithm enhances the spatial resolution of the daily data product to 4.45 km.

Finally, the Advanced Scatterometer (ASCAT) was launched in 2006 on the MetOp-A and MetOp-B satellites. The scatterometer is an upgraded successor of the above mentioned scatterometers onboard of the ERS-1/2 platforms. Thus, the pulses are also emitted in C-Band at 5.6 GHz in vertical co-polarization (VV). In this study, the similar SIR product is utilized, as done for the QSCAT data, with a spatial resolution of 4.45 km. Due to a lower spatial coverage of ASCAT, the data are given as 2-day averages.

Bootstrap sea-ice concentration (SIC) data from Nimbus-7 SMMR and DMSP SSM/I-SSMIS Passive Microwave Data product were used to define the areas with $SIC > 70\%$ for which the retrieval algorithms are valid (Section 5.2.2) (Comiso, 2000). The data are available daily from late 1978 to 2015 on a 25 km SSM/I polar stereographic grid. During this period, data of four different SSM/I sensors were used (F8 from July 1987 to December 1991, F11 from December 1991 to 1995, F13 from May 1995 to December 2008, and F17 from December 2006 onwards), and can be used without any further inter-sensor adjustment (Comiso and Nishio, 2008).

5.2.2 Methods

In the following, two methodologies to derive the timing of snowmelt processes on Antarctic sea from scatterometer observations are outlined. The effects of open water on the microwave signal (σ^0) are minimized by including only grid cells, where the sea-ice concentration is equal or more than 70% for at least three weeks from 1 October onwards. The following analysis is applied for every grid cell until the sea-ice concentration drops below 70%. In a next step, the analysis distinguishes between time series of daily mean, σ^0 , and its diurnal variation, $d\sigma^0$. The latter is defined as the absolute difference between the two diurnal σ^0 values from morning and evening satellite passes.

5.2 Snowmelt retrieval from satellite scatterometer data

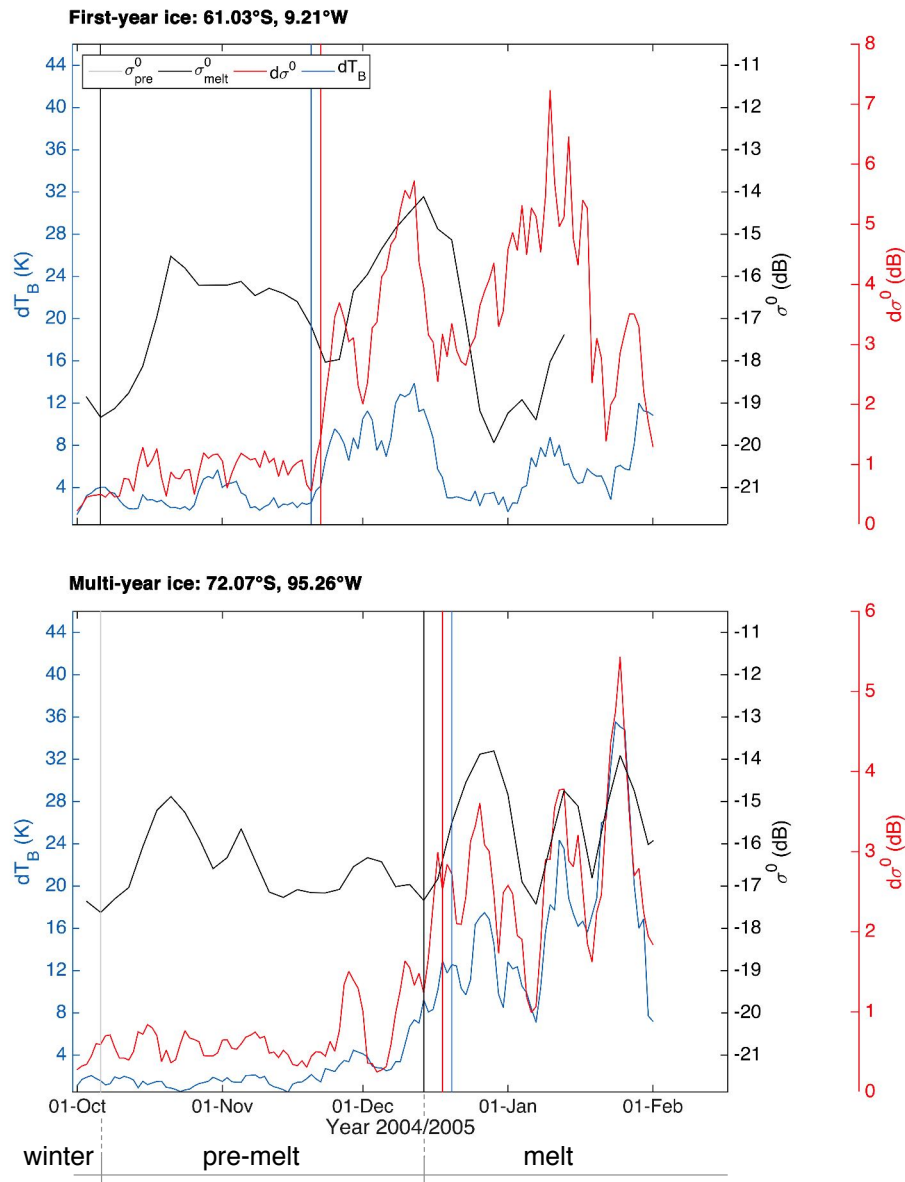


Figure 5.2: One example time series of the daily backscatter σ^0 , its diurnal variations $d\sigma^0$, and the diurnal variation in passive microwave brightness temperatures dT_B for first-year ice (upper panel) and multi-year ice (lower panel; Location 9, Figure 5.1) during the melt season 2004/2005. The gray, black, red and blue vertical line denotes the retrieved snowmelt onset dates from σ^0 , $d\sigma^0$ and dT_B , respectively. The time prior to the pre-melt onset is referred to as winter, between pre-melt and melt onset as pre-melt stage, and after the melt onset as melt season.

Transition retrieval from daily time series of σ^0

The seasonal cycle of surface properties of Antarctic perennial sea ice is evident in its backscatter time series with higher backscatter in summer than in winter (Haas, 2001). Figure 5.2 (lower panel) illustrates therefore the sharp spring increase in σ^0 while the change back to autumn/winter conditions proceeds much slower. In contrast, the backscatter time series of seasonal sea ice (Figure 5.2, lower panel) shows no comparable seasonal cycle as for the perennial sea ice. Since no adequate sea-ice type data product is available so far, we nevertheless apply the following approach for the entire Antarctic sea ice. Hence, for areas of expected first-year ice one must assume larger uncertainties for the detection of the snowmelt onset, compared to areas of perennial sea ice.

For a consistent continuation of the time series of melt stages on Antarctic sea ice retrieved by Haas (2001), the QSCAT and ASCAT data are sampled down to the temporal resolution of the ERS data (6-day means). In a next step, local maxima and their preceding local minima are tracked from three-point running means of each σ^0 timeseries. Subsequently, the analysis distinguishes between pre-melt conditions associated with changing physical properties in the lower snowpack and the actual snowmelt onset. The first local maximum succeeding the prior minimum after 1 October with a minimum difference between both of 2 dB is described as the pre-melt stage of the snowpack. Therefore, the preceding minimum is defined as pre-melt onset (σ_{pre}^0 , Figure 5.2). In contrast, the local maximum succeeding the prior minimum with a minimum difference of 3 dB describes the actual spring rise. Thus, the preceding minimum is defined as the snowmelt onset (σ_{melt}^0 , Figure 5.2).

In the following, the time prior to the pre-melt onset is referred to as winter, between pre-melt and melt onset as pre-melt stage, and after the melt onset as melt season (Figure 5.2).

Melt transition retrieval from diurnal variations of σ^0

Willmes et al. (2009) described the onset of snow surface melt of Antarctic sea ice related to dominant diurnal freeze-thaw cycles in the surface layer. Analyzing the time series of the absolute difference between two diurnal brightness temperature values (dT_B), they found an increase in dT_B once the temporary snowmelt begins at the snow surface.

Since the QSCAT data are also available twice a day, the backscatter time series can be utilized to derive diurnal variations in the snowpack of Antarctic sea ice. Therefore, we use the regionally adaptive approach by Arndt et al. (2016) to identify the snowmelt onset during austral spring. After applying a 5-day running mean to each $d\sigma^0$ time series between 1 October and 31 January, its histogram for each grid cell with a bin width of 0.5 dB is derived, respectively. An example is given in Figure 5.3. The histograms are subdivided into uni-modal and multimodal distributions, while a mode is defined as a local maximum bounded by at least one lower bin on each side. Multimodal distributions (Figure 5.3a and c, blue) reflect the different melt stages of the snowpack, including the

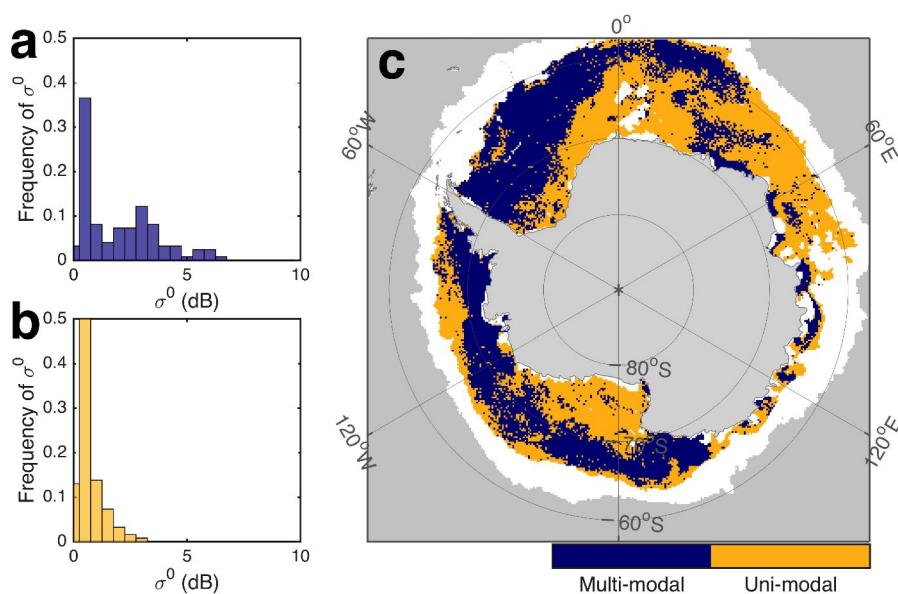


Figure 5.3: One example grid cell of (a) multimodal (Location 9, Figure 5.1) and (b) uni-modal distribution of $d\sigma^0$, and (c) its spatial distribution of the example melt season 2004/2005. The histograms contain only values for sea-ice concentrations $< 70\%$ from 01 October to 31 January. The white areas indicate the maximum sea-ice area of the previous winter.

associated differences in the strength of the mentioned freeze-thaw cycles, and are defined as a distribution of at least two modes. If a single mode exceeds a proportion of 90% of all included data points, it is attributed to uni-modal distributions (Figure 5.3b and c, orange). The latter are neglected in the following analysis, as they do not reveal the characteristic diurnal variations in the Antarctic snowpack. In a next step, an iterative threshold selection algorithm (Ridler and Calvard, 1978) is applied to the $d\sigma^0$ time series of each grid cell with a multimodal distribution to derive individual transition thresholds. Finally, the snowmelt onset from diurnal variations of σ^0 is defined as the first time when $d\sigma^0$ exceeds the respective local threshold for at least 3 consecutive days (Figure 5.2).

5.3 Results

5.3.1 Study locations

Figure 5.4 shows the time series of the backscatter coefficients for the 12 study locations indicated in Figure 5.1. All regions show a distinct seasonal cycle with a sharp increase during spring conditions and a subsequent slow backscatter decrease towards autumn/winter conditions. Weaker increases in backscatter precede the spring rise (Figure 5.2) while backscatter drops also occasionally interrupt it. On average, the backscatter rises from the winter minimum of -16.4 dB to the summer maximum of -11.4 dB for the 12 indi-

5 Seasonal snowmelt from scatterometer observations



Figure 5.4: Time series of backscatter signals from 1992 to 2014 in the regions shown in Figure 5.1. The time series are composed from ERS-1/2, QSCAT and ASCAT data while from 2001 onwards the data are down-sampled to 6-day means according to the ERS data before. The purple and blue lines denote the snow pre-melt (σ^0_{pre}) and melt onset (σ^0_{melt}) retrieved from daily time series of σ^0 , respectively. The red triangle indicates the melt onset retrieved from its diurnal variations ($d\sigma^0$). The green and yellow triangles denote the Temporary Snowmelt Onset (TeSMO) and Continuous Snowmelt Onset (SMO) from passive microwave observations according to Arndt et al. (2016).

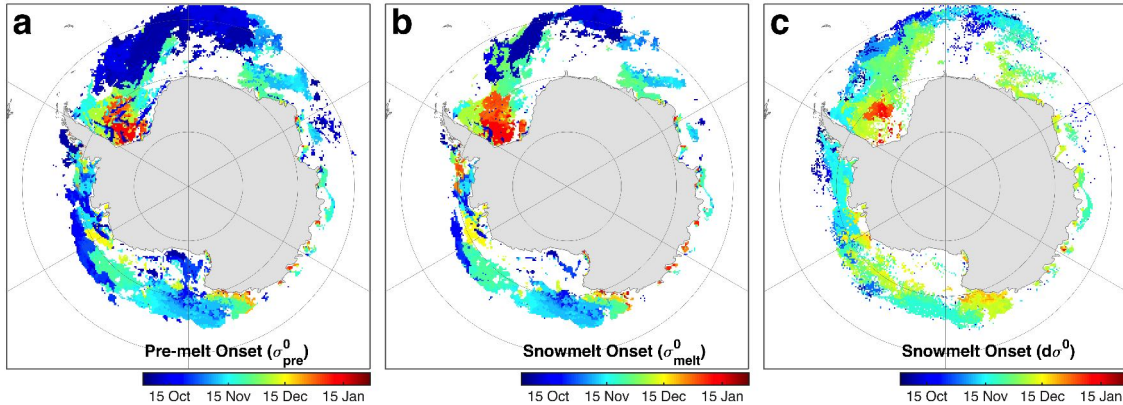


Figure 5.5: (a) Initial transition onset (σ_{pre}^0) and (snow) surface melt from (b) daily (σ_{melt}^0) and (c) diurnal variation data from active microwave observations ($d\sigma^0$) for the melt transition 2004/2005.

cated regions. The northwestern Weddell Sea (regions 1-3) as well as the Bellingshausen (region 8) and Ross Seas (regions 11 and 12) reveal the most pronounced amplitude of the backscatter seasonal cycle. In contrast, the difference between summer and winter backscatter is weakest for the central and southeastern Weddell Sea (regions 5-7). In addition, Figure 5.4 illustrates the retrieved snowmelt onset dates from satellite scatterometer (Section 5.2.2) and passive microwave data (Arndt et al., 2016) between 1992/1993 and 2014/2015. On average, the initial slow backscatter rise is on 29 November, 11 days prior to the actual melt retrieved from rapid rising daily backscatter and its diurnal variations (10 December). Melt onsets from diurnal variations in passive microwave observations start on average on 12 December and the subsequent continuous melt on 24 December for the 12 regions. Regions in the southeastern Weddell Sea (regions 5-7) and western Amundsen Sea (region 10) reveal frequently no distinct pre-melt or melt phases during the spring-summer transition (Figure 5.4).

5.3.2 Spatial variability

Figure 5.5 shows the retrieved pre-melt onset (σ_{pre}^0 , Figure 5.5a), the snowmelt onset from daily backscatter (σ_{melt}^0 , Figure 5.5b), and the snowmelt onset from diurnal variations of the backscatter ($d\sigma^0$, Figure 5.5c) for austral summer 2004/2005. The example year of 2004/2005 was chosen to ensure the best possible comparison with the previous study by Arndt et al. (2016) on melt transition retrieval from passive microwave observations.

During the austral summer 2004/2005, the pre-melt stage occurred between 6 October and 5 December with a mean onset date on 3 November. The subsequent retrieved melt onset from the daily backscatter signal (σ_{melt}^0) occurred, on average, 8 days later, in an interval from 6 October to 26 December. Both transition onsets reveal a strong latitudinal dependence with early transitions in the marginal-ice zone, and transition spreading southward as summer progresses. Latest onset is observed in the southern Weddell Sea around

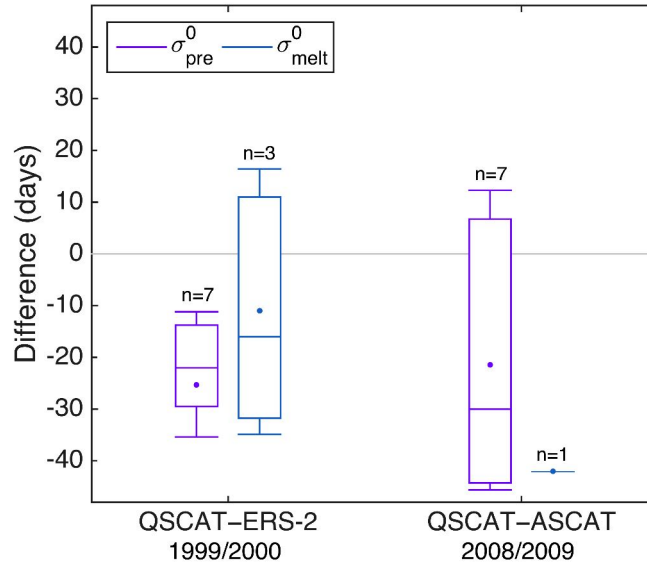


Figure 5.6: Difference between (pre-) melt onset dates retrieved from Ku-Band and C-Band for the 12 study locations for the overlap periods 1999/2000 and 2008/2009, respectively. Negative (positive) differences indicate an earlier (later) transition from Ku-Band. Boxes are the first and third quartiles while the whiskers display the 20- and 80-percentile. Dotes indicate the mean, dashes the median. n gives the number of respective data points constituting each dataset for the shown melt stage.

10 January. The retrieved snowmelt onset from diurnal variations in the backscatter signal shows a comparable latitudinal dependence with a weaker annual spread (1 month). Here, the averaged melt onset for the entire Antarctic occurred on 22 November, ranging from 30 October to 10 December. Again, the southern Weddell Sea reveals the latest onset around 8 January.

5.4 Evaluation of transitions from satellite scatterometer observations

5.4.1 Inter-comparison of active microwave observations

To investigate the differences between backscatter time series from lower (ERS-2/ASCAT, C-Band) and higher signal frequencies (QSCAT, Ku-Band), a comparison of the retrieved snow pre-melt and snowmelt onset for the overlap period of the sensors in 1999/2000 and 2008/2009, respectively, is performed. While Figure 5.6 shows the differences between Ku-Band and C-Band for the 12 study locations (Figure 5.1), Figure 5.7 illustrates the Antarctic-wide point-point comparison for both overlap periods, respectively. Due to the different backscatter signals and its seasonal changes of seasonal and perennial sea ice, the

5.4 Evaluation of transitions from satellite scatterometer observations

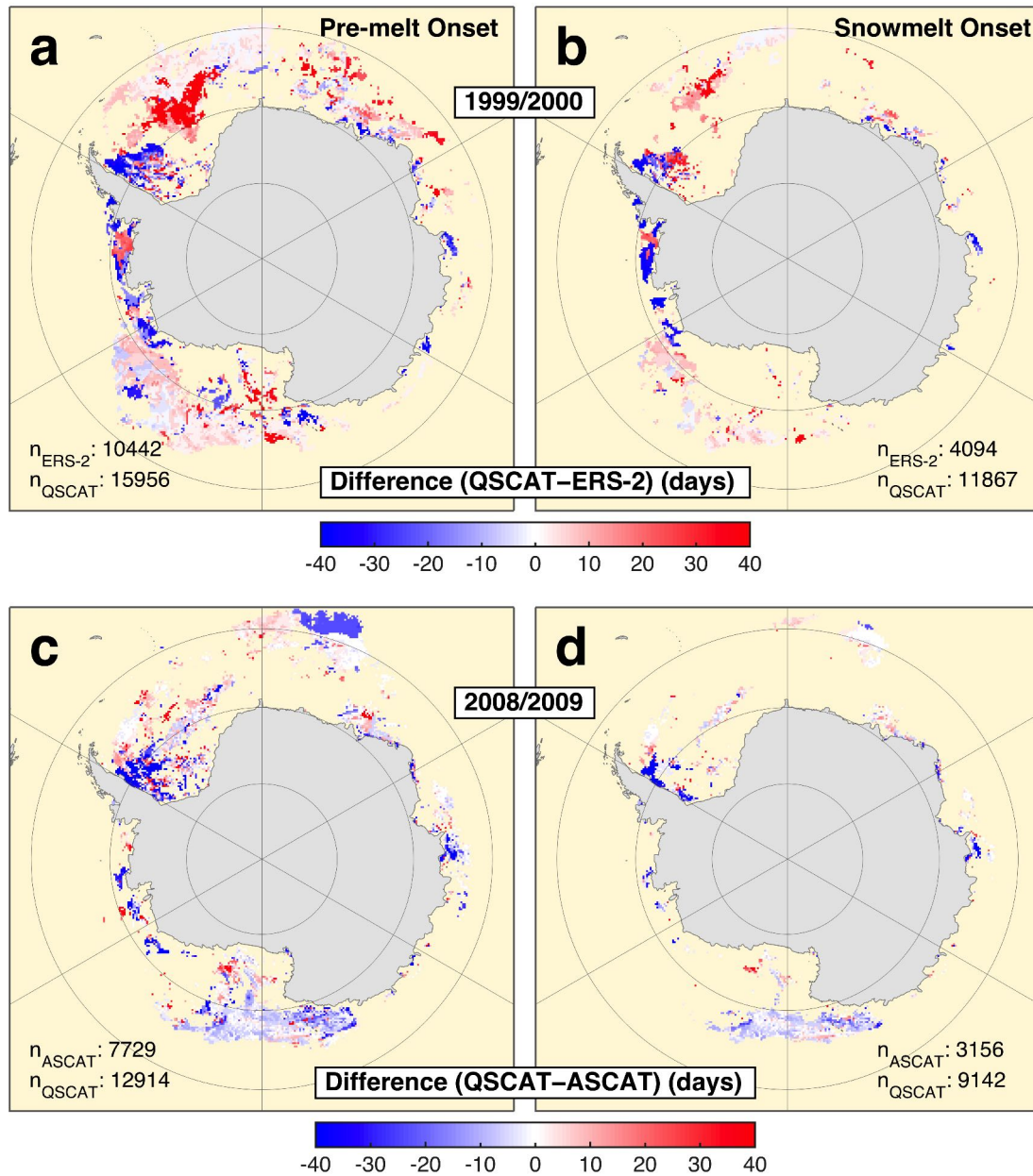


Figure 5.7: Point-to-point difference between melt onset dates retrieved from Ku-Band and C-Band covered by both retrievals in (a,b) 1999/2000 and (c,d) 2008/2009, respectively. Differences are calculated for the (a,c) pre-melt and (b,d) snowmelt onset for both years. The blue (red) color indicates an earlier (later) transition from Ku-Band. n gives the number of respective data points constituting each dataset for the shown melt stage.

following discussion focuses on expected perennial sea-ice areas only.

Comparing signal from QSCAT and ERS-2 shows primarily earlier transition dates from Ku-Band than from C-Band on perennial sea ice in the western Weddell Sea and

the Bellingshausen and Amundsen Seas, with a mean difference of 17 (20) days for the pre-melt (melt) onset (Figure 5.7). While 55% of the differences are smaller than 10 days for the pre-melt stage, it is only 48% of the differences for the melt stage. Considering the study locations only (Figure 5.6), shows similar tendencies towards an earlier pre-melt (melt) retrieved from Ku-Band than C-Band by 25 (11) days. However, especially in the Weddell Sea, transition time differences (concerning both overlap periods, Figure 5.7) can be more than one month, and show substantial spatial variations, as also shown in the wide spread of the calculated differences for the study locations (Figure 5.6).

The primarily earlier melt onset retrieval on perennial sea ice from Ku-Band compared to C-Band is most likely attributed to its different penetration depths into the snowpack and related differing sensitivities. Perennial sea ice is expected to be rather solid and cold preventing energy and brine fluxes from the upper ocean through the ice to the snow/ice interface, and vice versa. Additionally, a highly layered and metamorphous snow cover on top strengthens the isolation of the ice from atmospheric influences. The latter leads to seasonal changes of physical properties in the upper snowpack, which occur later in deeper layers or even at the snow/ice interface. Thus, due to their longer wavelength, C-Band sensors are expected to respond later on internal snowpack changes on perennial sea ice, compared to Ku-Band sensors.

5.4.2 Limitations of the assembled time series of satellite scatterometer observations

Comparing the area-wide transition retrievals from Ku-Band and C-Band signals, the most significant difference is the number of grid cells covered by the respective transition retrieval. Thus, the retrieval from Ku-Band data covers between 1.5 and 3 times more grid cells than from C-Band data, most notably for the actual snowmelt onset. This is mainly attributed to the chosen minimum difference of 2 and 3 dB between the local maximum and the preceding minimum to derive the pre-melt and snowmelt onset, respectively. Due to the longer wavelength and associated weaker volume scattering in the snowpack, backscatter coefficients from C-Band signals have a weaker amplitude of the seasonal cycle than backscatter coefficients from Ku-Band signals, which are therefore more sensitive to small-scale changes in the snowpack related to melt processes (Figure 5.4). The mean amplitude between the seasonal minimum and maximum is 13.35 dB for the QSCAT time period, while it is 7.66 and 9.35 dB for ERS and ASCAT, respectively, for the 12 study locations. One should therefore consider to adjust the chosen thresholds for the minimum difference between local minimum and maximum for different sensor frequencies. In order to generalize the entire algorithm, it would also be possible to consider overall relative thresholds compared to the actual absolute thresholds used in the presented study. Doing so, the annual amplitude of the backscatter seasonal cycle could be chosen as relative ratio for every grid cell. Moreover, the analysis must be differentiated for seasonal and

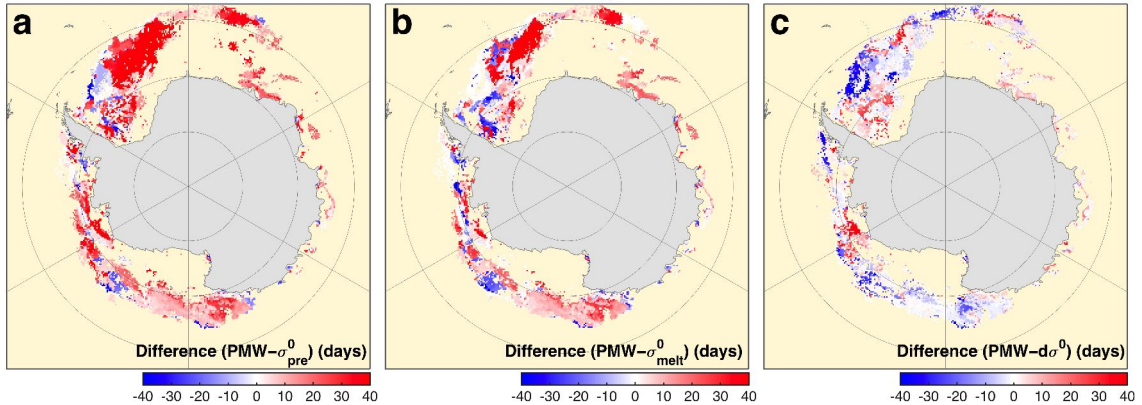


Figure 5.8: Point-to-point differences between transition dates retrieved from passive microwave observations and (a, b) daily backscatter signals (σ_{pre}^0 , σ_{melt}^0) and (c) diurnal variations ($d\sigma^0$) in 2004/2005. The red (blue) color indicates an earlier (later) transition from active microwave observations.

perennial sea ice, in order to minimize the uncertainties for Antarctic-wide calculations.

5.4.3 Comparison with melt transition from passive microwave data

In order to further investigate the differences between satellite scatterometer and passive microwave observations, Figure 5.8 shows a point-to-point comparison of the retrieved snowmelt onset dates for austral summer 2004/2005, while Figure 5.9 shows the mean differences for all 12 study locations on perennial sea ice from 1992/1993 to 2014/2015.

Figure 5.8a indicates that 85 % of the grid cells show an earlier pre-melt onset from time series of scatterometer observations than from diurnal variations in the passive microwave observations. Areas of earlier snowmelt onset from scatterometer observations are found primarily in West Antarctica. While the mean (median) snowmelt onset difference between passive microwave and scatterometer observations is 18 (13) days, only 14 % of the differences are smaller than 5 days, and 34 % are smaller than 10 days. The smallest differences are most notably in the northern Ross Sea, while biggest differences are detected in the expected seasonal sea-ice regime in the northern Weddell Sea.

Comparisons between the σ_{melt}^0 onsets from scatterometer observations and diurnal variations in the passive microwave observations show the same tendencies but with smaller differences. Thus, 16 % of the differences are smaller than 5 days, while 39 % are smaller than 10 days. This translates in a mean (median) difference of 11 (8) days. An earlier (later) snowmelt onset retrieved from scatterometer observations, compared to passive microwave observations, is observed primarily in seasonal (perennial) sea ice. This is most likely attributed to the different frequencies of passive microwave (37 GHz) and scatterometer signals (5.3 and 13.4 GHz), and associated deeper penetration depth of the scatterometer signal. Seasonal sea ice is expected to be rather warm, causing a larger brine volume at the snow/ice interface, associated with a strengthening of the basal layer

5 Seasonal snowmelt from scatterometer observations

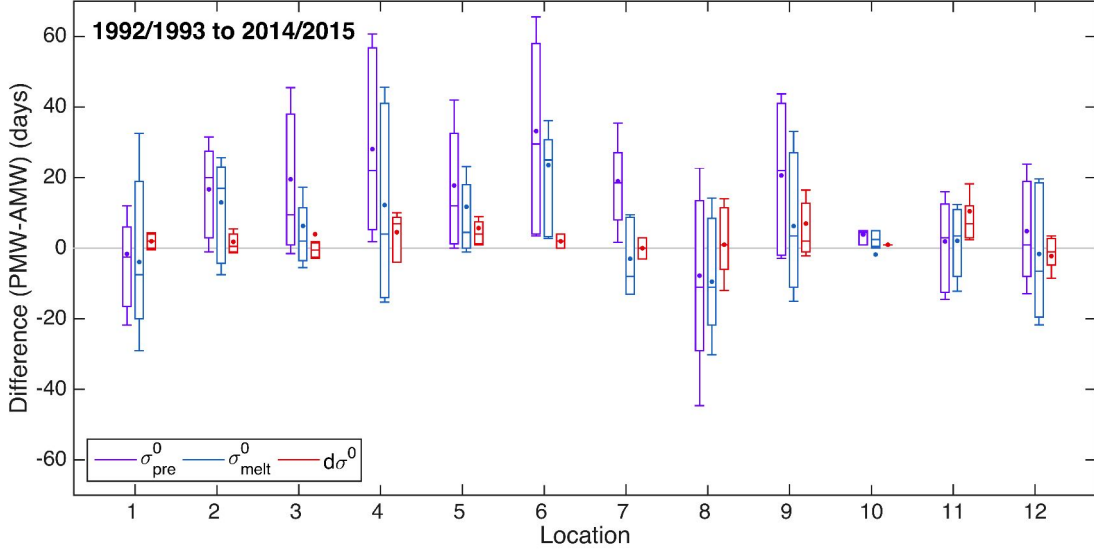


Figure 5.9: Mean differences between retrieved snowmelt onset from passive microwave (PMW, Temporary Snowmelt Onset, according to Arndt et al. (2016)) and scatterometer observations (active microwave observations, AMW) for the 12 study locations (Figure 5.1). Snowmelt onsets from daily backscatter signals (σ_{pre}^0 , σ_{melt}^0) are retrieved from 1992/1993 to 2014/2015, while the retrieval from diurnal variations in σ^0 ($d\sigma^0$, red) is only feasible from 2000 to 2008. Boxes are the first and third quartiles while the whiskers display the 20- and 80-percentile. Dotes indicate the mean, dashes the median. Positive (negative) differences indicate an earlier (later) transition from scatterometer observations.

volume scattering already early in the season (Yackel et al., 2007). Thus, scatterometer observation reveal earlier pre-melt and actual melt stages of snow on seasonal sea ice related to the brine increase. However, one must consider that the (pre-) melt onset retrieval on seasonal sea ice from scatterometer observations is subject to an unknown extent of uncertainties, and therefore the comparison needs to be handled carefully.

In contrast, perennial sea ice is expected to be colder and more solid, compared to seasonal sea ice. During the melt season, diurnal freeze-thaw cycles lead to a snow grain growth in the upper snowpack, and thus to an enhanced snow metamorphism. The changing size of snow grains is observed earlier by sensors with shorter than with longer wavelengths. Thus, scatterometers signals, with longer wavelengths, are expected to respond slightly later to this internal snowpack changes on perennial sea ice than the studied brightness temperatures (Arndt et al., 2016).

The point-to-point comparison of the retrieved melt onset from diurnal variations in both the passive microwave and scatterometer observations reveal opposing results compared to the previous ones. Both the mean and median of the differences are close to 0 days, indicating that almost half of the retrieved melt onset dates from scatterometer observations occur later compared to the passive microwave retrieval. Those are primarily

5.4 Evaluation of transitions from satellite scatterometer observations

found on seasonal sea ice, as shown in Figure 5.8c. This is expected, since the warm seasonal sea ice allows for an increased thermodynamic influence of the upward ocean heat flux on the dielectric properties of the snow/ice interface already during winter conditions (Yackel et al., 2007). The consequential warm snow/ice interface weakens the amplitude of the diurnal thawing and refreezing from above during pre-melt/melt conditions (Barber et al., 1995; Yackel et al., 2007). Hence, the increasing diurnal variations in the snowpack during the spring-summer transition seem to start slightly later in deeper snow layers (retrieved from scatterometer) than in the upper snowpack (retrieved from passive microwave observations). In contrast, the scatterometer responds slightly earlier on diurnal variations on perennial sea ice, compared to passive microwave observations (Figure 5.8c and 5.9). This might be related to the radiation budget of the snow surface: During spring, the shortwave solar radiation increases rapidly, warming not only the upper snowpack but also deeper layers. Nevertheless, the snow surface is expected to emit big amounts of longwave radiation (Perovich and Richter-Menge, 2009). Consequently, the available energy at the atmosphere/snow interface is insufficient to form liquid water. Due to less longwave radiation emission in deeper snow layers, the incoming solar radiation might induce the formation of liquid water during daytime. These differences in emitted longwave radiation in different snow layers might lead to earlier diurnal thawing and refreezing cycles in the deeper snowpack compared the upper snowpack, and therefore to an earlier detection from scatterometer than passive microwave observations.

Overall, one must consider, that the differences between the retrieved onset of diurnal variations from scatterometer and passive microwave observations are small (Figure 5.8c and 5.9), and do therefore complement each other.

5.4.4 Time series of transition dates

In order to compare the time series of the scatterometer observations with passive microwave observations for the Southern Ocean, Figure 5.10 shows the seasonal transitions from both instruments from 1992/1993 to 2014/2015. Melt transitions from diurnal variations in the daily backscatter signal and brightness temperatures show a good agreement. Also the Antarctic-wide mean snowmelt onsets from daily backscatter coefficients reveal the same tendency as the retrieved snowmelt onset dates from passive microwave observations (TeSMO). Thus, none of the given snowmelt onsets show a significant temporal trend, while all do show similar inter-annual variations. The largest differences are generally found during the Ku-Band record, with the largest inconsistency found in 2001 and 2006, when the median snowmelt onsets from σ_{pre}^0 and σ_{melt}^0 occur 16 and 22 days earlier, respectively (Figure 5.9). During the time period of C-Band observations, the differences are smaller. For the years 1993/1994 to 1996/1997 during the ERS-1/2 period, and 2011/2012 and 2014/2015 during the ASCAT period, TeSMO is derived even earlier than σ_{melt}^0 . This is consistent with the discussions in Section 5.4.1 and 5.4.2. Thus, the

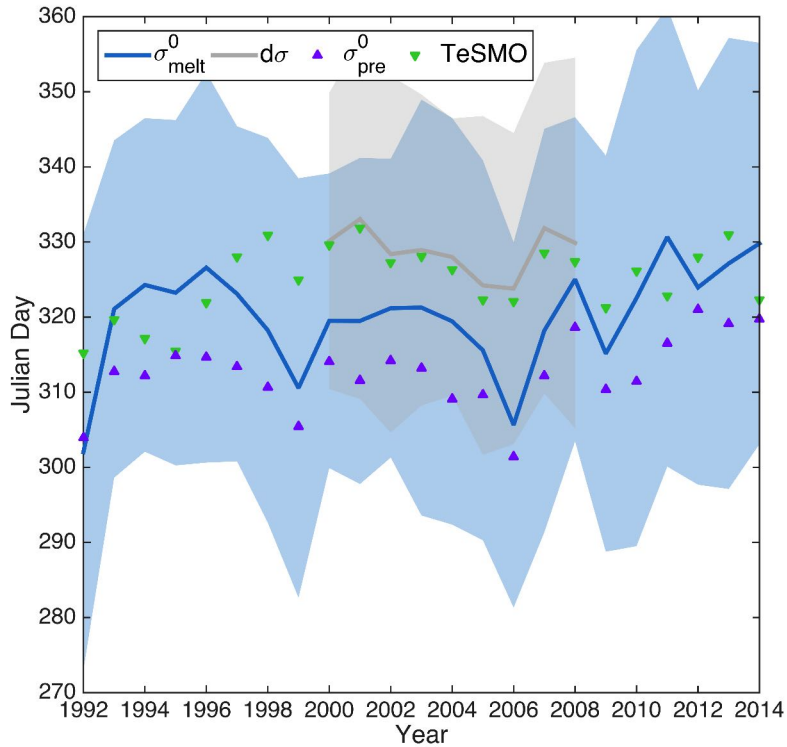


Figure 5.10: Time series of retrieved spring-summer transition from daily backscatter signals (σ_{melt}^0 , blue) and its diurnal variations ($d\sigma^0$, gray) from 1992/1993 to 2014/2015. Solid lines denote the Antarctic-wide mean, shaded areas the respective Antarctic-wide standard deviation. Initial transition means (σ_{pre}^0) and transition means from passive microwave observations (Arndt et al., 2016) indicating the Temporary Snowmelt Onset (TeSMO) are depicted as purple and green triangles, respectively.

weaker seasonal cycle in the backscatter coefficients from C-Band signals results in a delayed determination of transition onsets in the Antarctic snowpack. Again, even though all retrieved melt onsets show a similar inter-annual progress, one must consider possible uncertainties, especially in the retrieved pre-melt and melt onset dates from daily backscatter time series on seasonal sea ice.

5.5 Summary and Conclusions

In this study, a newly developed method is presented, which allows to utilize the distinct annual cycle of the scatterometer observations in order to describe seasonal melt processes in the lower snowpack of the ice-covered Southern Ocean. While the rapid spring rise in the backscatter signal is related to snowmelt and intense superimposed ice formation at the snow/ice interface, preceding temporal rises indicate pre-melt conditions related to

initial transition of physical properties in the lower snowpack. Both transitions lead to an increase in volume and surface scattering, shown as spring and summer maxima in the backscatter time series.

Results of the presented study reveal that, on average, both transition onsets are 8 days apart. The additional analysis of the diurnal variation in the scatterometer observations allows to describe the characteristic temporary snowmelt on Antarctic sea ice, occurring another 8 days later.

To account for long-term changes, the algorithm is applied to scatterometer observations acquired from 1992 to 2015, combining satellite-based mission of ERS-1/2, QSCAT and ASCAT. Previous studies on snowmelt onsets from passive microwave observations have shown no relations between the ongoing evolution of Antarctic sea ice and the timing of snowmelt processes (Arndt et al., 2016). This is also shown by the temporal evolution of seasonal snowmelt processes from scatterometer observations, which shows also only strong inter-annual variations, instead of a significant trend.

The comparison of transitions from scatterometer and passive microwave observations indicates spatially varying differences. While the warm seasonal sea ice, associated with a large brine volume at the snow/ice interface, leads to an early increase in the daily backscatter (earlier (pre-)melt onset), it diminishes the scattering difference between spring thawing and refreezing in the snowpack, associated with a delayed transition onset, compared to the one from passive microwave observations. Since signals with longer wavelengths respond later to snow grain growth and related snow metamorphism due to diurnal thawing and refreezing processes during austral spring/summer, the scatterometer observations reveal a later (pre-)melt of snow on the cold and solid perennial sea ice. In contrast, diurnal variations in the snowpack are observed slightly earlier from scatterometer than passive microwave observations, which might be related to differences in the emitted longwave radiation in different snowpack depths. The overall good agreement between snowmelt onsets from diurnal variations in brightness temperature (passive microwave observations) and backscatter coefficients (active microwave observations) allows for future application of temporary snowmelt processes of higher spatial resolution.

Overall, one needs to consider, that the presented method on snowmelt onset retrieval from backscatter time series is essentially valid for applications on perennial sea ice, but less for seasonal sea ice. It is therefore suggested to distinguish the algorithm for seasonal and perennial sea ice. In addition, we observe a weaker annual amplitude of the backscatter signal for C-Band than for Ku-Band due to different wavelengths. Thus, C-Band signals respond weaker to seasonal changes in the snowpack, compared to Ku-Band signals. Instead, the retrieval algorithm covers for Ku-Band signals between 1.5 and 3 times more grid cells than for C-Band, due to the fixed threshold between local minimum and maximum of the respective backscatter signal. It is therefore suggested to consider relative thresholds for the retrieval algorithm for future applications instead of the absolute ones used so far. However, for perennial sea ice, the retrieved snowmelt onsets from

5 *Seasonal snowmelt from scatterometer observations*

different frequencies agree fairly well, indicating a robust time series.

Thus, the results of the presented study on scatterometer observations do both extend and approve the achievements from the previous study on passive microwave observations. Hence, it underlines that scatterometer observations are more sensitive to (pre-)melt processes at the snow/ice interface, as e.g. superimposed ice formation, and are therefore strongly linked to changes in the oceanic heat flux of the Southern Ocean and related basal melting. In contrast, passive microwave data allow to describe melt processes at the snow/atmosphere interface and in the inner snowpack associated with increasing fresh water content and snow metamorphism. Thus, it is worth combining passive microwave scatterometer observations to determine different processes modifying the physical properties of the Antarctic snowpack in different vertical layers.

6

Influence of surface properties on light transmission through Antarctic sea ice

In Chapter 4 and 5 characteristic sea-ice and snow surface properties of Antarctic sea ice are identified, which are discussed in the context of their evolution during the seasonal cycle. It is shown that the year-round persistent Antarctic snow cover contributes significantly to the sea-ice mass balance due to the resultant widespread surface flooding and related snow-ice formation.

In this chapter, the described snow and sea-ice surface properties of Antarctic sea ice are related to its optical properties and the associated impact it has, not only on the mass but especially on the energy budget of the ice-covered Southern Ocean. Doing so, results of a case study of spectral solar radiation measurements under Antarctic pack ice with an instrumented Remotely Operated Vehicle (ROV) in the Weddell Sea in September 2013 are presented. In order to identify the key variables controlling the spatial distribution of the under-ice light regime, under-ice optical measurements are exploited in combination with the simultaneous characterization of surface properties, such as sea-ice thickness and snow depth.

Results of the study are discussed in context of recent studies on the spatial variability of the Arctic under-ice light field (Chapter 3) focusing on the distinctly different dominant sea-ice and snow surface properties between the northern (strong surface melt and summer melt ponds) and southern (year-round snow cover and strong surface flooding) hemisphere sea-ice cover.

This chapter is - with marginal changes - identical to the content submitted in Arndt et al. (under review).

6.1 Introduction

Snow on sea ice plays a crucial role for interactions between the ocean and atmosphere within the polar climate system and is a key driver of polar marine ecosystem function, especially in the year-round snow-covered Antarctic sea-ice zone (Massom et al., 2001; Massom and Stammerjohn, 2010). Snow contributes substantially to the sea-ice mass balance of Antarctic sea ice as the heavy snow load depresses the ice below the water level, causing flooding and the formation of snow-ice during the subsequent refreezing

of the formed slush (Arrigo, 2014; Eicken et al., 1994; Haas et al., 2001). In addition, superimposed ice, forming during summer when percolating melt water refreezes at the snow/ice interface, adds to the sea-ice mass (Haas, 2001; Nicolaus et al., 2003). The snow cover also determines the surface energy budget of the ice-covered ocean by influencing the amount of shortwave radiation being reflected, absorbed, and transmitted into the upper ocean (Brandt et al., 2005; Massom et al., 2001). Snow extinction coefficients are more than one order of magnitude larger than those of bare sea ice, and snow albedo can be almost twice as large as that of ice (Grenfell and Maykut, 1977; Perovich, 1996).

The horizontal and vertical distribution of solar radiation under sea ice impacts not only the physical properties but also biological processes and bio-geochemical fluxes in the sea ice and the uppermost ocean (Arrigo et al., 2012; Fritsen et al., 2011; Perovich, 1996, 2007). Due to their different spectral absorption characteristics, snow, sea ice, sea water, biota, sediments, and other impurities affect the spectral composition of the light penetrating from the atmosphere into the ocean (Belzile et al., 2000; Mundy et al., 2005; Perovich, 1996; Uusikivi et al., 2010). The spectral composition of transmitted under-ice irradiance measurements has been used to estimate biota (e.g. ice algal biomass as Chlorophyll *a*, Chl *a*) and snow depth in Arctic sea ice (Campbell et al., 2015; Mundy et al., 2007). The latter is also of high interest in Antarctic pack ice, since comprehensive snow measurements from space and/or in situ measurements are lacking. In a recent study, Melbourne-Thomas et al. (2015) applied normalized difference indices of under-ice irradiance spectra to develop algorithms to estimate snow depth in Antarctic pack ice.

Optical properties of Arctic sea ice, in particular the effects of spatial variations of snow and sea-ice surface properties on the under-ice light regime, are relatively well studied (Frey et al., 2011; Katlein et al., 2015; Light et al., 2008; Nicolaus et al., 2012; Perovich, 1996; Perovich et al., 1998). Investigations of the under-ice light regime in the ice-covered Arctic Ocean have been carried out as either local point measurements using radiometers mounted to retractable L-shaped arms or with instrumented Remotely Operated Vehicles (ROV) which allow investigations on larger spatial scales ($> 1000 \text{ m}^2$) (Nicolaus et al., 2012; Perovich, 1996; Perovich et al., 2011a). The results reveal strong correlation between the spatial variations in light transmittance of Arctic sea ice, and the prevalent ice type (first-year/ multi-year ice) and its surface properties (e.g. melt pond coverage, snow cover), respectively. On large scales the ice thickness distribution is the main driver of the spatial variability in the under-ice light field (Katlein et al., 2015). Using these relationships, Arndt and Nicolaus (2014) were able to derive a seasonality for under-ice radiation for the Arctic Ocean based on ice type and surface characteristics.

In contrast, the information on the optical properties of Antarctic sea ice, especially free-drifting pack ice, remains extremely sparse (Fritsen et al., 2011; Michael and Higgins, 2014). To our knowledge, point measurements of under-ice irradiance spectra (L-arm measurements) were collected during the Winter Weddell Outflow Study (WWOS) in the Weddell Sea in austral summer 2006 (Lemke, 2009) followed by two Sea Ice Physics and

Ecosystems Experiment voyages (SIPEX1 and SIPEX-2) in East Antarctica in austral spring 2007 and 2012 (Meiners et al., 2016; Worby et al., 2011).

In this case study, we present the first data on the spatial variability of sea-ice physical parameters and their influence on solar radiation under Antarctic pack ice. Under-ice solar radiation was measured with an ROV instrumented with a radiometer and sensors supporting under-ice navigation. In order to identify key processes controlling the spatial distribution of the under-ice light field in an area of approximately 100m-by-100m, we combine under-ice optical measurements with coincident characterization of the surface properties, such as sea-ice thickness and snow depth. Results are discussed in context of recent studies on the spatial variability of the Arctic under-ice light field focusing on the distinctly differing surface properties between the northern (e.g. summer melt ponds) and southern (e.g. year-round snow cover, surface flooding) hemisphere sea-ice covers.

6.2 Data and Methods

6.2.1 Study site and measurements

ROV measurements were carried out during the expedition ANT-29/7 of the German ice-breaker R/V Polarstern during the ‘Winter studies on sea ice and key species’ (WISKEY) project in the northern Weddell Sea (Figure 6.1) (Meyer and Auerswald, 2014). The described sea-ice floe was surveyed during the second ice camp at about 60.78°S and 26.36°W. Measurements with an ROV were carried out from 18 to 26 September 2013 on a 100m-by-100m grid during 17 dives. The sea-ice surface conditions were stable during this period, which allows merging all under-ice measurements into one dataset for the following analyses (Figure 6.2). The ROV was instrumented with an upward-looking RAMSES-ACC (Advanced Cosine Collector) spectral radiometer (Trios GmbH, Rastede, Germany) to measure down-welling planar under-ice spectral irradiance (320 to 950 nm) and an upward-looking Valeport VA500 altimeter to measure the distance between the ROV and the bottom of the sea ice. The ROV position was determined using a long baseline positioning system (LBL) consisting of a Woods Hole Oceanographic Institution (WHOI) FSK micro-modem equipped with an ITC 3013 transducer (mounted on the ROV) and interrogating four Benthos XT-6001 transponders (15 m depth) which were coupled to surface GPS units and spaced around the survey site in a rectangle with 400 m side length (e.g. Williams et al., 2013). The surface GPS units were also used for precise co-registration of temporally displaced surface measurements using GPS equipped snow- and total-ice-thickness instruments, i. e. accounting for ice-floe drift and rotation in-between ROV- and surface measurements (e.g. Williams et al., 2013). Incident solar irradiance was measured synchronously with a reference RAMSES-ACC sensor next to the ROV grid on the sea-ice surface. Surface measurements of sea-ice thickness and snow depth were conducted after the ROV measurements to avoid disturbance of the snow cover.

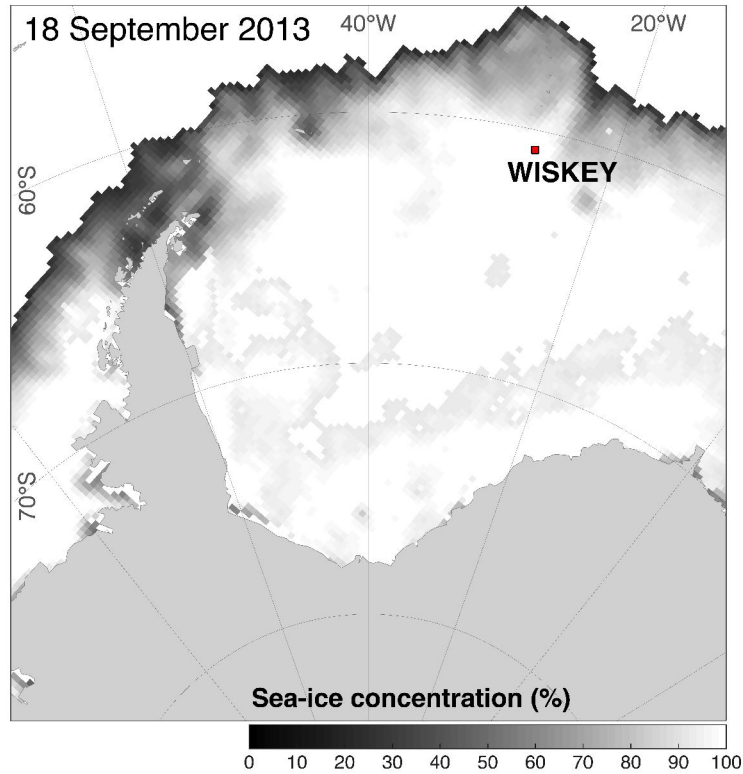


Figure 6.1: Ice-station location sampled during voyage ANT-29/7 (PS81, WISKEY) with R/V Polarstern in the Weddell Sea from 18 to 26 September 2013. The background image shows the sea-ice concentration on 18 September 2013 provided by www.meereisportal.de.

For all presented broadband values, the hyper-spectral measurements were integrated over the range of Photosynthetically Active Radiation (PAR) from 400 to 700 nm after interpolation to a spectral resolution of 1 nm (Nicolaus et al., 2010b). Details on the processing of the optical data and the calculation of the transmittance as a ratio of under-ice irradiance and incoming solar irradiance are described in Nicolaus et al. (2010b) and Nicolaus and Katlein (2013). Instead of correcting all under-ice irradiance data to the ice-ocean interface, only data points with a maximum ROV-ice distance of 2 m were taken into account. This resulted in a total of 4586 valid under-ice irradiance and light transmission spectra. To account for multiple sampling due to overlapping ROV tracks and position errors, all data were re-gridded by averaging all measurements taken within a grid cell of 2m-by-2m. All grid cells overlap for 1m translating to an effective grid resolution of 1 m (running mean).

In addition to the optical measurements with the ROV, total sea-ice thickness (sea-ice thickness plus snow depth) was measured on the entire ice floe and particularly on the ROV survey grid with a ground-based multi-frequency electromagnetic induction instrument (GEM-2, Geophex Ltd.) (Hunkeler et al., 2016). The instrument was mounted

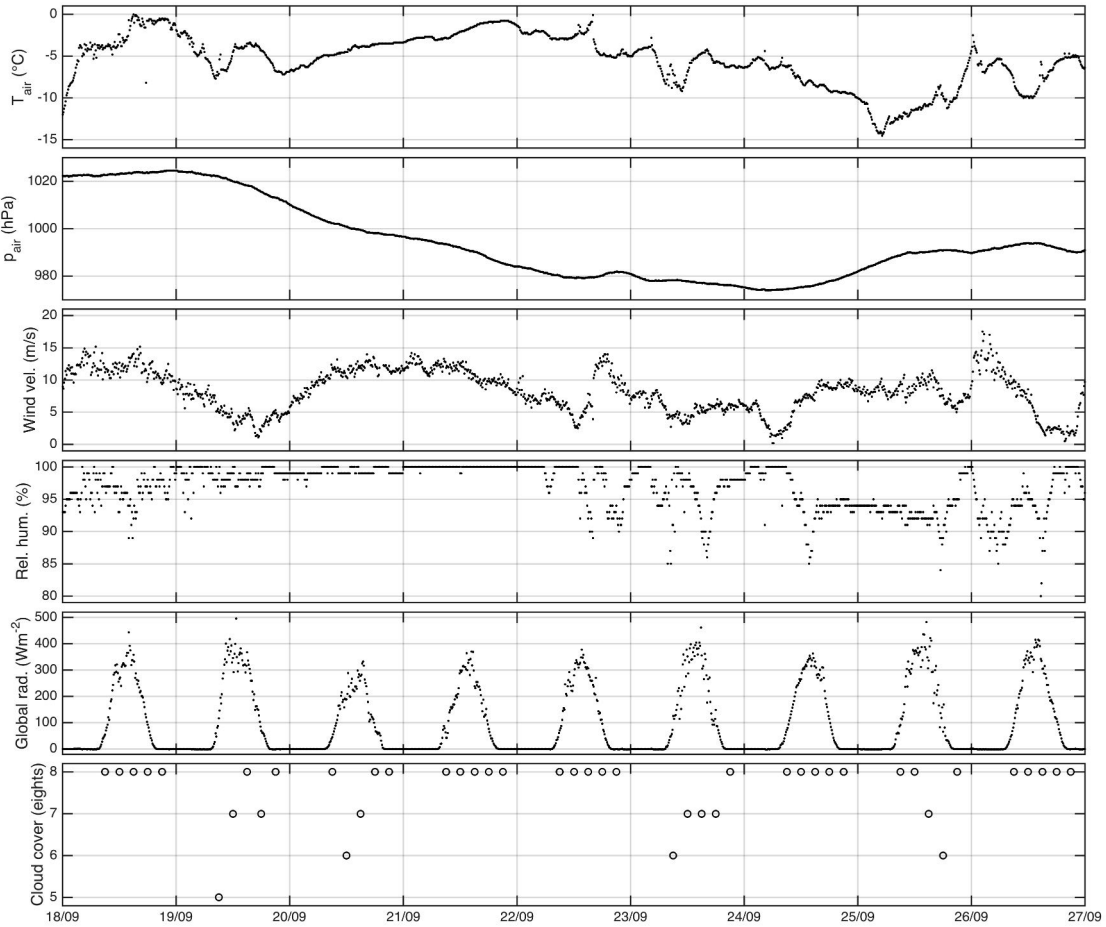


Figure 6.2: Weather conditions during the ice camp on the voyage ANT-29/7 (PS81, WISKEY) with R/V Polarstern in the Weddell Sea from 18 to 26 September 2013 (König-Langlo, 2016).

on a modified plastic sled and pulled over the snow surface. A GPS-equipped Magna Probe (Snow Hydro, Fairbanks, AK, USA) was operated simultaneously in order to obtain snow depth along the GEM-2 tracks. Snow depth measurements were taken every 1.5 to 2.5 m along the track. Sea-ice thickness was then calculated as the difference of total sea-ice thickness and snow depth. Both sea-ice thickness and snow depth measurements were interpolated to the locations of the under-ice measurements using nearest-neighbor resampling.

6.2.2 Data analyses

Ice freeboard and flooding

Ice freeboard, F , is controlled by the difference between sea-ice buoyancy and snow load. Especially for the ice-covered Southern Ocean, two typical states of sea ice must be dis-

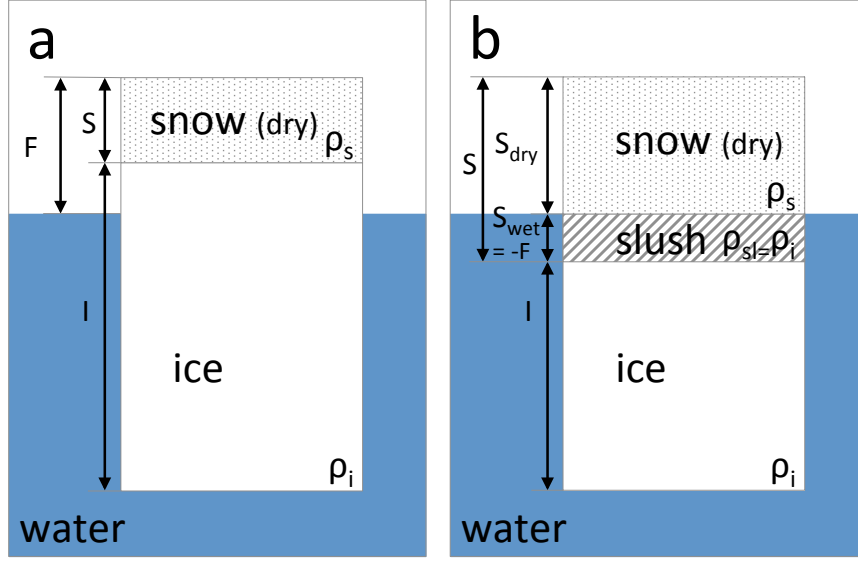


Figure 6.3: Two typical states of Antarctic sea ice. (a) Positive freeboard with the snow/ice interface above the sea level. (b) Negative freeboard with the snow/ice interface below the sea level. The flooded snow (slush) is referred to as (negative) freeboard and is assumed to have the same density as sea ice.

tinguished, one with the snow/ice interface above the sea level (positive freeboard, Figure 6.3a), and the other with the snow/ice interface below the sea level (negative freeboard, Figure 6.3b). For the case of a positive freeboard (Figure 6.3a), the ice buoyancy of floating sea ice is defined by the density of sea ice, ρ_i , the density of seawater, ρ_w , and the sea-ice thickness, I , while the snow load is calculated from the density of snow, ρ_s , and the snow depth, S (Lange et al., 1990; Sturm and Massom, 2010). Assuming a hydrostatic equilibrium for a floating snow-covered sea-ice floe, ice freeboard, F , can be calculated by

$$F = \frac{I \cdot (\rho_w - \rho_i) - S \cdot \rho_s}{\rho_w}. \quad (6.1)$$

A negative freeboard is associated with flooding at the snow/ice interface leading to the formation of slush and snow-ice at the snow/ice interface (Figure 6.3b), which can therefore be assumed to have the same density as sea ice (Knight, 1988). Therefore, as soon as F gets negative (Equation 6.1), the slush layer thickness, and thus the freeboard is calculated as

$$S_{wet} = -F = S + \frac{I + S}{1 + \frac{\rho_s}{\rho_w - \rho_i}}. \quad (6.2)$$

In this study, constant densities for seawater, sea ice and snow of 1023.9, 915.1 and 300 kg m^{-3} are assumed, respectively (Yi et al., 2011).

Extinction coefficients

Extinction coefficients describe the attenuation of light penetrating from the air-snow/ice interface to the ice-ocean interface due to scattering and absorption (Perovich, 1996). Bulk extinction coefficients, κ_d , were calculated spectrally-resolved from light transmittance, T, and total sea-ice thickness, I+S,

$$\kappa_d(\lambda) = -\frac{\ln(T(\lambda))}{I+S}. \quad (6.3)$$

To investigate the difference of light attenuation characteristics of snow and sea ice, we fitted a multiple exponential model to estimate single ice and snow extinction coefficients, κ_{ice} and κ_{snow} , dependent on the respective ice thickness, I, and snow depth, S

$$\tau(I, S, \lambda) = \exp(-\kappa_{ice}(\lambda) \cdot I) \cdot \exp(-\kappa_{snow}(\lambda) \cdot S). \quad (6.4)$$

Taking into account an additional flooding layer at the snow/ice interface, and therefore extending the multiple exponential model towards a third component for flooded snow (slush), κ_{slush} , leads to

$$\tau(I, S, F, \lambda) = \exp(-\kappa_{ice}(\lambda) \cdot I) \cdot \exp(-\kappa_{snow}(\lambda) \cdot S) \cdot \exp(-\kappa_{slush}(\lambda) \cdot |F|). \quad (6.5)$$

To solve Equation 6.4 and for the attenuation coefficients, the *Curve fitting* toolbox of the statistical software *matlab* was used by applying a multiple non-linear least-square regression algorithm. Uncertainties are given as a function of the accuracy of the retrieved sea-ice thickness, which is given as 0.1 m for the used GEM-2 (Hunkeler et al., 2015).

Normalized difference index (NDI)

Normalized difference indices, NDIs, of under-ice irradiance spectra have been used to investigate the relationship between e.g. snow depth and transmitted spectra under sea ice. Following Mundy et al. (2007), NDIs were calculated for all wavelength combinations (400 to 700 nm) of λ_1 and λ_2 from transmitted under-ice irradiance spectra, $E_d(\lambda)$, through the entire snow and ice column, according to

$$\text{NDI} = \frac{E_d(\lambda_1) - E_d(\lambda_2)}{E_d(\lambda_1) + E_d(\lambda_2)}. \quad (6.6)$$

The subsequent spectral correlation surfaces were constructed from the Pearson's correlation coefficients calculated from correlations of NDIs for each wavelength pair and snow depth (Mundy et al., 2007).

Table 6.1: Summary statistics for measured and calculated physical sea-ice parameters for the PS81 data set, non-flooded grid cells only (positive freeboard), and flooded grid cells only (negative freeboard). Reported values are mean values \pm its standard deviation or mode values. Extinction coefficients are estimated as bulk-extinction coefficients according to Equation 6.3 and separated for ice and snow applying an exponential fit according to Equation 6.4.

Parameter		All data points (n = 4595)	Non-flooded data points only (n = 1080)	Flooded data points only (n = 3515)
Sea-ice thickness (m)		0.93 ± 0.45	1.42 ± 0.51	0.78 ± 0.30
Snow depth (m)		0.39 ± 0.13	0.30 ± 0.12	0.42 ± 0.12
Ice freeboard (m)		-0.08 ± 0.10	0.05 ± 0.04	-0.12 ± 0.07
Light transmittance	mean	0.0024 ± 0.0030	0.0019 ± 0.0025	0.0026 ± 0.0031
	mode	0.0008	0.0008	0.0008
Bulk extinction coefficient (m^{-1})	mean	5.52 ± 1.66	4.49 ± 1.54	5.84 ± 1.56
	mode	5.5	3.75	5.5
Extinction coefficient (m^{-1})	ice	6.829 ± 0.045	1.264 ± 0.133	2.06 ± 0.97
	snow	7.737 ± 0.049	31.76 ± 0.69	31.22 ± 0.53
	slush	-	-	6.21 ± 3.23

6.3 Results

6.3.1 Physical properties of the ice floe and their distribution functions

The surveyed large ice floe ($> 1 \text{ km}^2$) was a compound first-year sea-ice floe with significant deformation and variable snow cover. GEM2-based ice thickness and Magna Probe snow-depth surveys for the entire floe show a mean ice thickness and snow depth of $1.00 \pm 0.48 \text{ m}$ and $0.38 \pm 0.15 \text{ m}$, respectively. Considering the ROV grid only, which measured approx. 100m-by-100m, the mean sea-ice thickness decreased to $0.93 \pm 0.45 \text{ m}$ with an additional snow layer of $0.39 \pm 0.13 \text{ m}$ (Table 6.1). The estimated ice freeboard reveals that 77% of the surface layer in the ROV grid is assumed to be flooded with a maximum negative freeboard of up to 0.40 m (Equation 6.2, Figure 6.4c, Table 6.1). Excluding the flooded grid cells, the mode of the GEM2-derived sea-ice thickness distribution shifts towards higher values, from 0.7 m (all data points) to 1.5 m (non-flooded data points only, Figure 6.5a). The snow depth distribution has a modal value of 0.25 m for non-flooded data points and 0.4 m for the entire data set, respectively (Figure 6.5b). Also the mean snow depth is lower for non-flooded data points compared to flooded ones ($0.30 \pm 0.12 \text{ m}$ and $0.42 \pm 0.12 \text{ m}$, Table 6.1).

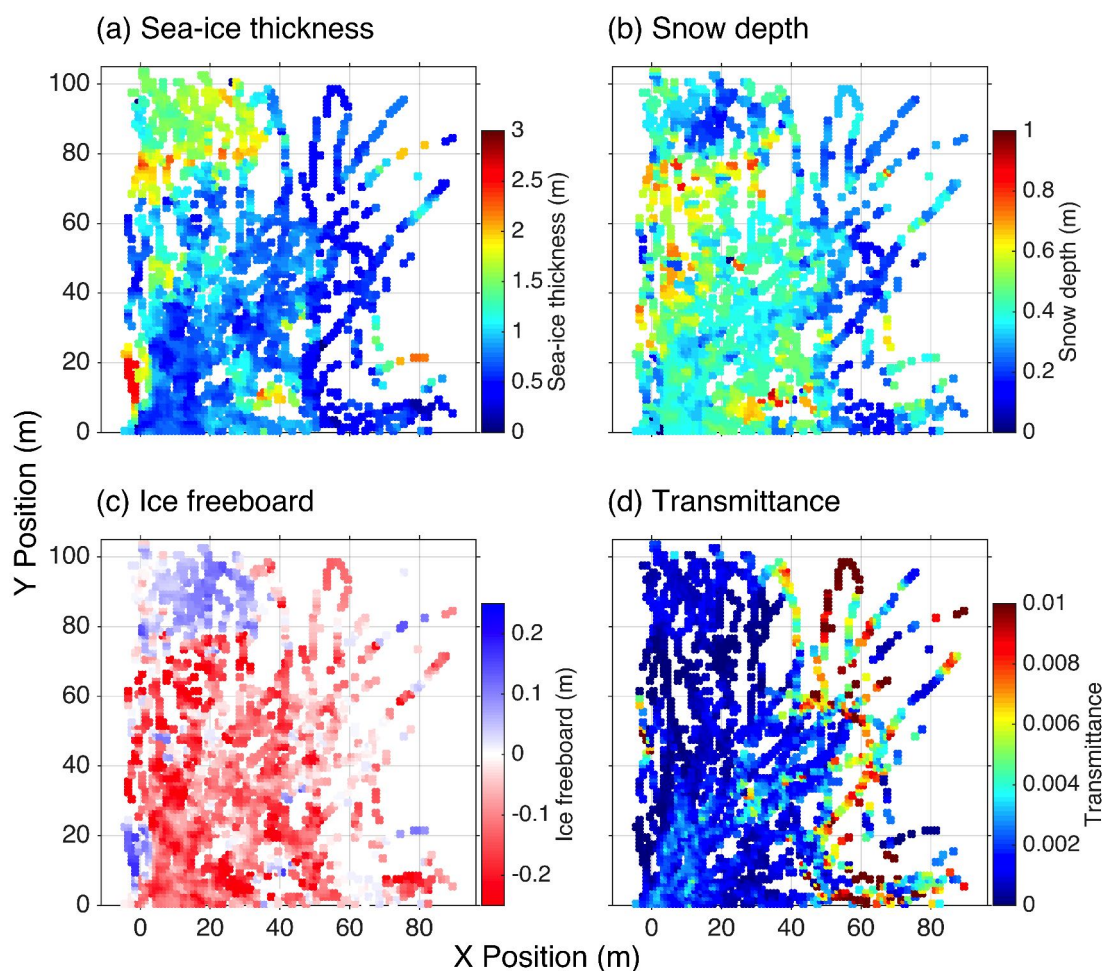


Figure 6.4: Physical properties of the ice floe within the Remotely Operated Vehicle (ROV) survey area. (a) Sea-ice thickness derived from the ground-based multi-frequency electromagnetic induction instrument (GEM-2). (b) Snow depth measured with the Magna Probe. (c) Ice freeboard estimated from Equation 6.1. (d) Light transmittance derived as the ratio of measured transmitted irradiance and incoming solar irradiance above the surface. Sea-ice thickness and snow depth measurements as well as ice freeboard are interpolated to the ROV transect lines. All data are gridded to a 2m-by-2m grid.

This is expected, as thicker sea ice and less snow are clear indicators for non-flooded sea ice.

The light transmittance distribution shows a modal value of 0.0008 (0.08 %) for the entire data set (Figure 6.5c, Table 6.1). The right part of the ROV-grid ($x > 40$ m, Figure 6.4d) is dominated by a stronger variability in the light transmittance with values up to 0.05 (5 %) leading to an overall mean light transmittance of 0.0024 ± 0.0030 (0.24 ± 0.30 %). Distinguishing for flooded and non-flooded data points, the modal transmittance values

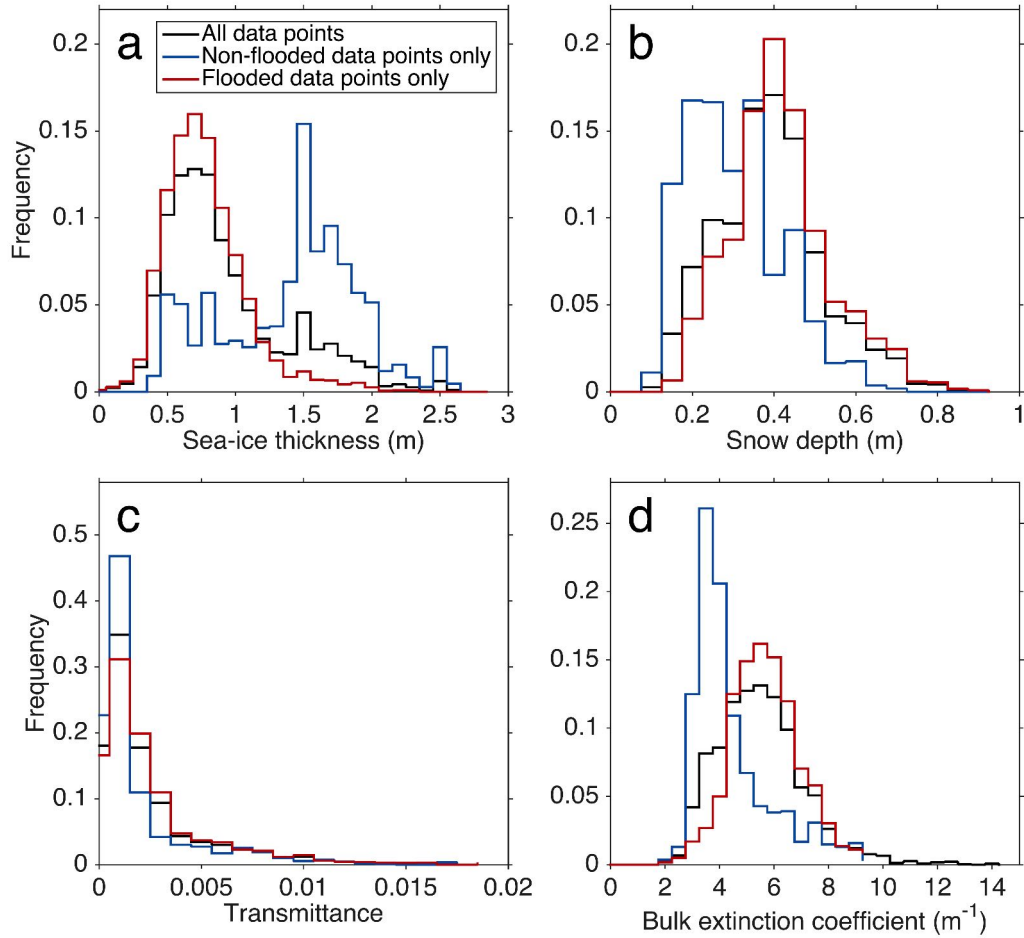


Figure 6.5: Histograms of (a) sea-ice thickness, (b) snow depth, (c) light transmittance, and (d) calculated bulk light extinction coefficients for the entire data set (black), non-flooded data points only (blue), and flooded data points only (red).

remain both at 0.0008 (0.08%). In contrast, considering flooded areas only (Figure 6.4d, Table 6.1) the average transmittance shifts towards 0.0026 ± 0.0031 ($0.26 \pm 0.31\%$). Non-flooded areas show a lower averaged transmittance of 0.0019 ± 0.0025 ($0.19 \pm 0.25\%$).

6.3.2 Light attenuation

Relating the (bulk) light transmittance to both sea-ice thickness and snow depth requires a multi-dimensional exponential model (Equation 6.4). Single snow and ice extinction coefficients were computed for both the entire data set and the subsets of flooded and non-flooded data points only. Analyzing the entire data set results in bulk extinction coefficients of $6.829 \pm 0.045 \text{ m}^{-1}$ and $7.737 \pm 0.049 \text{ m}^{-1}$ for sea ice and snow. The extinction

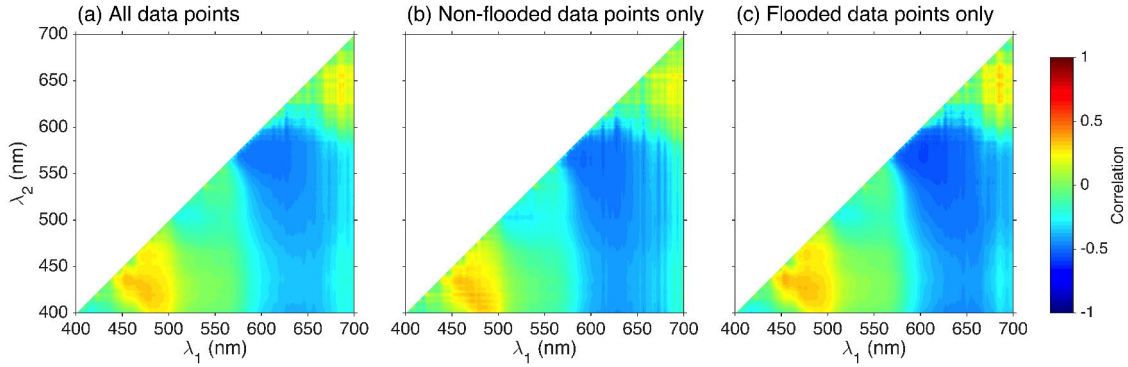


Figure 6.6: Correlation surfaces of normalized difference indices (NDI) for snow depth for (a) all data points, (b) non-flooded data points only, and (c) flooded data points only. λ_1 and λ_2 indicate the used wavelength pairs according to Equation 6.6.

coefficient for sea ice seems to be extremely high (expected between 0.8 and 1.5 m^{-1} , Light et al. (2008); Perovich (1996)) and for snow comparable low (expected between 10 and 100 m^{-1} , Perovich (2007); Warren (1982)). The analysis shows that only 65 % of variance in the under-ice light field can be explained by sea-ice thickness and snow depth. Extending the model towards a third component for the snow-slush layer on flooded areas only (Equation 6.2.2), the exponential fit explains still only 61 % of the light transmittance variations and leads to extinction coefficients of $2.06 \pm 0.97 \text{ m}^{-1}$, $6.21 \pm 3.23 \text{ m}^{-1}$ and $31.22 \pm 0.53 \text{ m}^{-1}$ for sea ice, the flooding layer and snow, respectively (Table 6.1). In contrast, fitting non-flooded data points only results in extinction coefficients for sea ice and snow differing by one order of magnitude, $1.264 \pm 0.133 \text{ m}^{-1}$ (sea ice) and $31.76 \pm 0.69 \text{ m}^{-1}$ (snow) and the exponential fit explains 74 % of the light transmittance variations. These extinction coefficients are much more realistic and compare well with previously reported values (e.g. Grenfell and Maykut, 1977; Perovich, 1996, 2007).

Bulk light extinction coefficients calculated from bulk light transmittance and total ice thickness (sea-ice thickness plus snow depth, Equation 6.3) show a uni-modal distribution for both the entire data set and the chosen subsets (Figure 6.5d). The modal bulk extinction coefficient for the entire data set and the flooded data points is 5.5 m^{-1} whereas bulk extinction coefficients are lower for non-flooded data points with a distinct modal value at 3.75 m^{-1} . The tail of the distribution is longer (maximum 14 m^{-1}) for the entire data set than for the non-flooded data points only (maximum 10 m^{-1}).

6.3.3 Spectral correlation surfaces

Figure 6.6 shows the correlation surfaces of normalized difference indices (NDIs) for snow depth, which shows distinct changes between positive and negative correlations along the diagonal at approx. 440, 580 and 670 nm for both the entire data set and the non-flooded

data points only. These sign changes are due to inflection points in the spectral attenuation and absorption of impurities (ice algae) and snow (Perovich, 1996), the almost linear increase in snow attenuation from 570 nm leads to a negative correlation coefficient (Mundy et al., 2007).

The correlations between the NDIs and snow depth are quite weak with correlation coefficients of 0.49, 0.52 and 0.57 for the entire data set, non-flooded and flooded data points only, respectively. The highest absolute correlations were found at wavelength pairs of 613:581 nm (entire data set) and 613:580 nm (non-flooded data points only) while the one for flooded tends towards lower wavelengths (601:570 nm). The weakest pronounced effect of snow on the transmitted spectral irradiance is shown at wavelengths between 400 and 570 nm, and 620 and 700 nm, which can be associated with the prevalent biomass absorption in these wavelength bands (Ficek et al., 2004).

6.3.4 Spectral light attenuation and transmission

Figure 6.7 shows the mean spectral transmitted irradiance, light transmittance and bulk extinction coefficients for the examined survey area distinguished for flooded and non-flooded areas (Figure 6.7a,c,e) as well as subdivided into snow depth classes, one smaller than 0.2 m and the other one between 0.2 and 0.4 m for an equal sea-ice thickness of 0.8 to 1 m (Figure 6.7b,d,f).

Flooded and non-flooded areas reveal the same spectral shape for transmitted irradiance, bulk light transmission and bulk extinction coefficients, with flooded transmittance and under-ice irradiance values being slightly larger (Figure 6.7a). Extinction coefficients at PAR wavelengths were about 30 % larger for flooded and denser snow than for non-flooded areas (Figure 6.7e). In both cases, the largest spectral light transmittance and smallest spectral bulk extinction coefficient were found between 470 and 570 nm. The absolute spectral minimum shifts from 520 nm for non-flooded data points to 550 to 560 nm for flooded data points, most likely as a result of increasing impurities in the slush layer. Moreover, transmitted irradiance and light transmittance decreases with increasing snow depth (Figure 6.7b), and thus increasing scattering in the snow. The spectral under-ice irradiance field and bulk extinction coefficients indicate less wavelength dependence below than above wavelengths of 570 nm. For wavelengths beyond 570 nm, light attenuation follows an almost linear increase (Figure 6.7e), a typical feature of higher ice absorption at longer wavelengths, which implicates a prominent decrease in the spectral transmitted irradiance and light transmittance (Figure 6.7c,e). Even though the absolute correlation coefficients with snow increase in the same wavelength range, the correlation is not significant (Figure 6.6), indicating the low spectral dependency of snow attenuation (Perovich, 1996). Our results for non-flooded data points only show a steeper increase in transmittance and irradiance decrease for thinner than a thicker snow at wavelengths beyond 570 nm (Figure 6.7b) and therefore also higher correlation coefficients (Figure 6.6b),

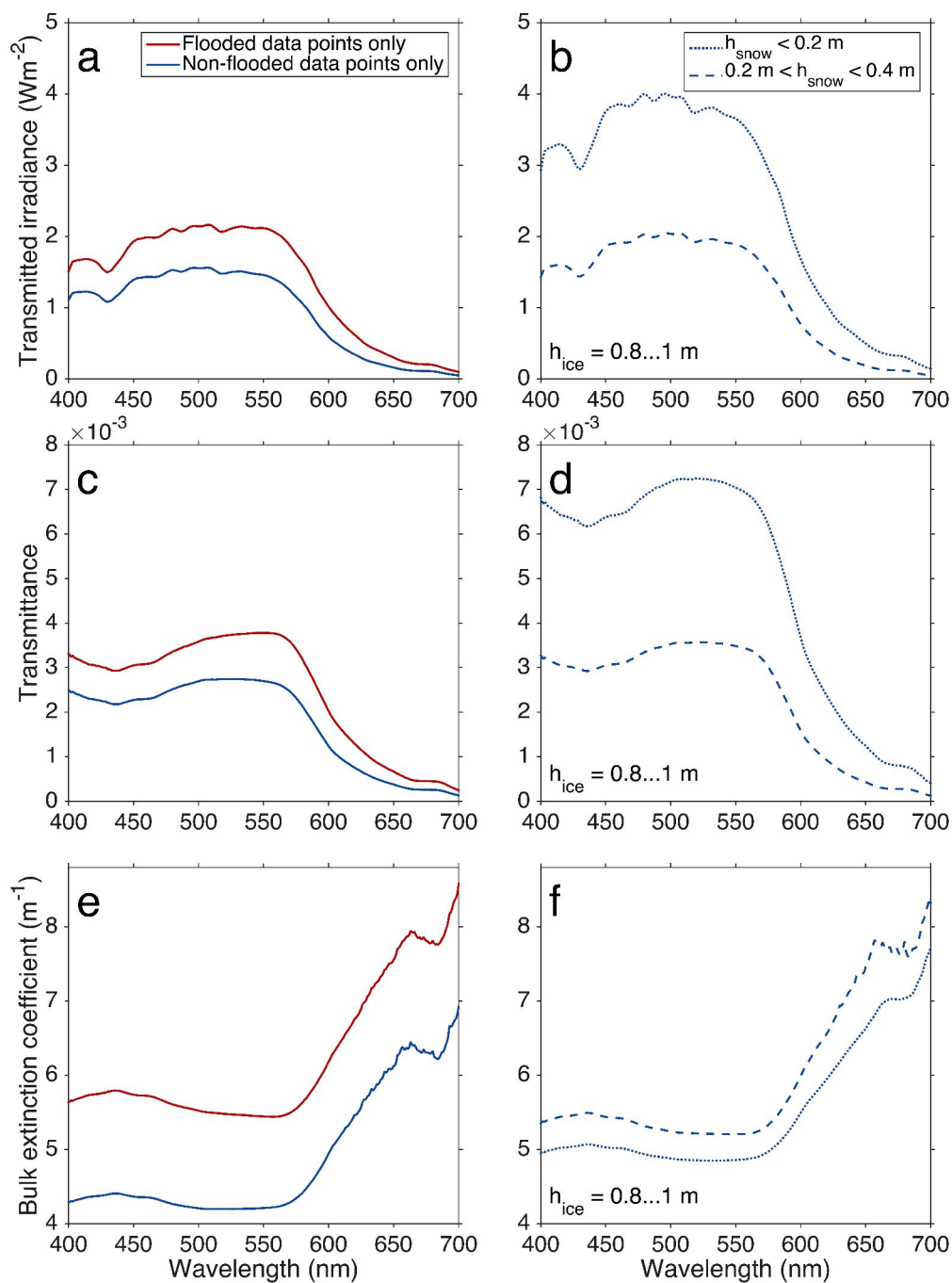


Figure 6.7: Mean spectral (a,b) transmitted irradiance, (c,d) light transmittance and (e,f) bulk extinction coefficient for (a,c,e) flooded data points only (red) and non-flooded data points only (blue) and (b,d,f) non-flooded data points only with a sea-ice thickness between 0.8 and 1 m subdivided into two snow classes: snow depth $< 0.2 \text{ m}$ (dotted lines) and snow depth $> 0.2 \text{ m}$ and $< 0.4 \text{ m}$ (dashed lines).

whereas the maximum of 0.52 at 614:518 nm is still not substantial for a suitable relation between snow depth and NDI.

6.4 Discussion

6.4.1 Spatial variability of the under-ice radiation

The presented case study shows an overall dark under-ice light regime for austral spring (September) Weddell Sea pack ice with a modal light transmittance below 0.1%. Our study also illustrates the importance to distinguish between flooded and non-flooded areas when relating the spatial variability of optical properties to Antarctic sea-ice characteristics. The results from non-flooded grid cells show high extinction coefficients for snow ($31.76 \pm 0.69 \text{ m}^{-1}$, Section 6.3.3) revealing a strong scattering in the respective snowpack. Since Antarctic sea ice is covered with snow during most of the year (Massom et al., 2001), seasonal snowmelt processes (Arndt et al., 2016) lead to a snowpack consisting of highly compacted and metamorphic layers of snow with internal ice layers (Nicolaus et al., 2009). This highly inhomogeneous snowpack and density structure leads to weak observed correlations of transmitted solar radiation with snow depth (Figure 6.6). In contrast, sea-ice in the marginal-ice zone (MIZ) is expected to have a younger and less metamorphous snow layer compared to our studied pack-ice floe. Thus, point-measurements during WWOS in austral spring 2006, and the SIPEX voyages during austral spring 2007 and 2012 in the MIZ (see Section 6.1) show strong correlations between light transmittance and snow depth. The more homogeneous snowpack in the area leads to correlation coefficients of up to 0.744 and 0.789, respectively (Melbourne-Thomas et al., 2015).

Regarding flooding areas, an additional layer of water-saturated snow needs to be considered. Although slush may contain more light-absorbing impurities, it has less interfaces than snow and is therefore expected to reveal a reduced scattering, and thus has an extinction coefficient much lower than the one of snow ($6.21 \pm 3.23 \text{ m}^{-1}$ vs. $31.22 \pm 0.53 \text{ m}^{-1}$). High uncertainties of the estimated extinction coefficients might be related to the complex and not quantified geometry of the slush layer. Moreover, the calculated extinction coefficient of sea ice is slightly higher than for non-flooded areas ($2.06 \pm 0.97 \text{ m}^{-1}$ vs. $1.26 \pm 0.13 \text{ m}^{-1}$). This might be explained by a combination of several factors: Flooded sea ice is expected to have higher snow loads (Figure 6.5b) translating directly into increasing extinction coefficients compared to non-flooded areas. In contrast, the flooded snow layer (slush) has a different geometry related to less scattering and lower extinction coefficients. However, since flooding is caused by sea water penetrating from the ocean/ice to the snow/ice interface, flooded sea ice is expected to have more impurities leading to an increased scattering. Overall, the combination of the different geometry of sea ice, slush and snow leads to slightly higher bulk extinction coefficients of flooded compared to non-flooded areas.

Moreover, snow-slush is expected to refreeze rapidly and form subsequent snow-ice at the sea-ice surface. Consequently, the horizontal and vertical inhomogeneous distributions of snow, slush and snow-ice at the sea-ice surface prevent a more detailed description of the flooded sea-ice and snow column. Nevertheless, changing physical properties of flooded snow, as e.g. higher densities emphasizes dominant scattering processes in the flooded (thicker) snowpack, which drive the magnitude of the extinction coefficient and the related transmittance (Perovich, 1996). In contrast, the wavelength-dependence of flooded and non-flooded areas is similar indicating a similar absorption behavior for both media.

Our case study on one pack-ice floe demonstrates that the spatial variability of light levels of the Antarctic under-ice light regime is driven by the presence of surface flooding on scales of smaller than 100m-by-100m. On larger scales the widespread and persistent snow cover prevents light transmission through the snow and ice column into the upper ocean. Instead, the under-ice light regime might be determined by light transmitted into the ocean through leads and breaks between the ice floes (lateral incidence of light), as studied during a recent study in the Weddell Sea (Boebel, 2015). Consequently, the entire vertical light profile in the upper ocean must be considered, as the light maximum might not occur at the ice-ocean interface but in deeper layers (Frey et al., 2011; Katlein et al., 2016). The broad variety and abundance of organisms in the ice-covered Southern Ocean also supports the notion of sufficient light availability in the upper ocean column (Taylor et al., 2013).

To quantify relations of physical properties of the snowpack and underlying sea ice, more studies of the under-ice light field are necessary, not only in the pack ice but also in the marginal sea-ice zone. The latter is expected to reveal different relationships between surface properties and the light regime in the upper ocean, compared to the (inner) pack ice.

6.4.2 Comparison to Arctic light transmittance

Arctic and Antarctic sea-ice areas are known as being rather different - not only regarding their opposing evolution in sea-ice extent during the last decades (Stammerjohn et al., 2012) but particularly in their distinctly different dominant surface properties in spring and summer. Snow on Arctic sea ice melts during the spring-summer transition (Markus et al., 2009), leading to a subsequently widespread ponding of the sea-ice surface (Rösel and Kaleschke, 2012; Webster et al., 2015). In contrast, snow on Antarctic sea ice persists year-round (Massom et al., 2001) with diurnal freeze-thaw cycles at the snow surface modifying the physical properties of the entire snowpack (Arndt et al., 2016; Willmes et al., 2009), most evident by the formation of ice lenses and superimposed ice at the snow/ice interface (Nicolaus et al., 2009). Thicker snow and thinner ice in the Antarctic as compared to Arctic sea ice, result in widespread surface-flooding of Antarctic sea ice which can affect about 15-30% of the Antarctic sea-ice zone (Arrigo, 2014, and citations

therein). Flooding is rather rare in the Arctic.

The high cover of Arctic sea ice with seasonal melt ponds causes not only the high amount of transmitted solar radiation during summer (Arndt and Nicolaus, 2014; Hudson et al., 2013; Nicolaus et al., 2012) but also drives the spatial variability of the under-ice light field on scales smaller 1000 m² (Katlein et al., 2015). While the transmittance of bare first-year (multi-year) ice reaches up to 4 (1) % during Arctic summer, it increases for ponded first-year (multi-year) ice up to 22 (15) % (Arndt and Nicolaus, 2014; Nicolaus et al., 2012). Considering larger areas, Katlein et al. (2015) describe variations in sea-ice thickness as indicator for the variability in the Arctic-wide light transmission. In contrast, the present study indicates that snow depth and flooding are key variables controlling the magnitude and spatial distribution of the Antarctic under-ice light field on scales smaller than 10000 m².

Our results suggest that, due to the highly heterogeneous quality of the snowpack, the impact of snow depth on the Antarctic under-ice light field cannot be extrapolated to larger scales without additional in-situ information. Instead, a future Antarctic-wide up-scaling of light transmittance will need to consider the history and thus former melt processes of the snowpack in every single grid cell. This may then allow an estimate of internal physical properties as well as the quantification of, e.g., metamorphous snow layers and ice lenses (Arndt et al., 2016). To account for seasonal changes in the Antarctic snowpack, local observations from autonomous systems, as e.g. snow or ice-mass balance buoys, can be used (Maksym et al., 2012). The annual cycle of processes at the snow/ice interface, as e.g. surface flooding, snow-ice formation, or superimposed ice formation, can be derived from radar backscatter data (Haas, 2001), since comprehensive field observations are not feasible. Recent studies on snow depth and ice thickness observations from radar and passive microwave sensors allow for an additional Antarctic-wide estimation of sea-ice freeboard and related quantification of sea-ice surface flooding (Kern et al., 2016; Kern and Ozsoy-Çiçek, 2016). In contrast, the distinct seasonal cycle of Arctic surface properties and more homogeneous vertical snowpack properties allow the parameterization of Arctic-wide light transmittance during all seasons (Arndt and Nicolaus, 2014).

6.5 Summary and Conclusions

This case study presents first measurements of the spatial variability of under-ice light transmission connected to measurements of spatially varying surface properties of an Antarctic pack ice floe. An improved understanding of optical properties of Antarctic sea ice and the quantification of light penetrating through sea ice into the upper ocean are needed to further understanding of the timing and amount of interior sea-ice melt (sea-ice mass balance) as well as under-ice ecosystem dynamics.

Even though the amount of light transmission through Antarctic sea ice is low (< 0.1 %) during austral spring, we were able to identify key processes determining the spatial vari-

ation of the under-ice light field. While the distinction between flooded and non-flooded sea-ice regimes dominates the spatial scales of under-ice variability for areas smaller than 100m-by-100m, a distinct relation between Antarctic surface properties and the under-ice light field appears not feasible. Although the strong scattering of the thicker snowpack in flooded areas controls the high magnitude of its extinction coefficients, the dominant heterogeneous snowpack prevents the description of optical properties as a function of sea-ice surface properties. In contrast, the Arctic under-ice light field can be directly quantified from sea-ice properties, e.g. sea-ice type and melt pond coverage (Hudson et al., 2013; Nicolaus et al., 2012). Combining surface properties with Arctic-wide remote sensing data, has allowed up-scaling of the under-ice light regime for all seasons (Arndt and Nicolaus, 2014). Performing a similar up-scaling for Antarctic sea ice requires a more extensive approach. Firstly, an analysis of the temporal evolution of the snowpack from microwave remote sensing observations is needed (Arndt et al., 2016; Haas, 2001). This would allow for a better quantification of the amount of metamorphous snow layers and ice lenses in the prevalent snowpack. Secondly, we suggest a more detailed analysis of the vertical snow structure associated with light transmission measurements for future field work. The combination of sea-ice thickness, snow depth, and its stratigraphy with under-ice solar radiation measurements will contribute to a better understanding of snow/ice interface processes which, according to our study, will be key to understand transmission and for potential Antarctic-wide up-scaling approaches of the under-ice light.

7

Key findings and Outlook

In this thesis the influence of sea-ice surface properties on the energy and mass budgets of Arctic and Antarctic sea ice is examined. Satellite remote sensing data and in-situ observations of sea ice and its snow cover are combined to describe in detail the seasonal cycle of dominant surface characteristics in the northern and southern hemisphere. The seasonal and inter-annual changes of the physical properties of the snowpack and underlying sea ice differ crucially in both hemispheres, suggesting that different processes govern the energy and mass budgets of the Arctic and Southern Oceans. An improved understanding of these hemispheric differences in sea-ice and snow surface properties is crucially needed to better interpret and use a variety of available sea-ice remote sensing data products. The additional knowledge gained within this thesis allows for an enhanced area-wide description and quantification of the currently observed sea-ice evolution.

7.1 Implications of seasonal effects on the sea-ice mass and energy budgets: A bi-polar view

The overall aim of the thesis is to investigate the influence of seasonal changes of surface properties on the energy and mass budgets of Arctic and Antarctic sea ice. The main focus is therefore the analysis of the transition from spring to summer conditions, because its timing is identified as the main driver of the Arctic annual energy and mass budgets.

Arctic sea ice

Sea-ice surface properties in the Arctic are generally characterized by a distinct seasonal cycle. The most pronounced changes occur during the spring-summer transition, starting when liquid water forms within the snow due to increasing radiative heating and light absorption in the upper snowpack. The subsequent melt leads to a complete snowmelt and widespread formation of melt ponds at the sea-ice surface (Figure 7.1). So far, an improved understanding of the impact of the current changes in sea-ice conditions on the Arctic-wide partitioning of solar energy under the sea ice is missing. Thus, in the first presented study (Chapter 3), a parameterization is developed to quantify the annual cycle

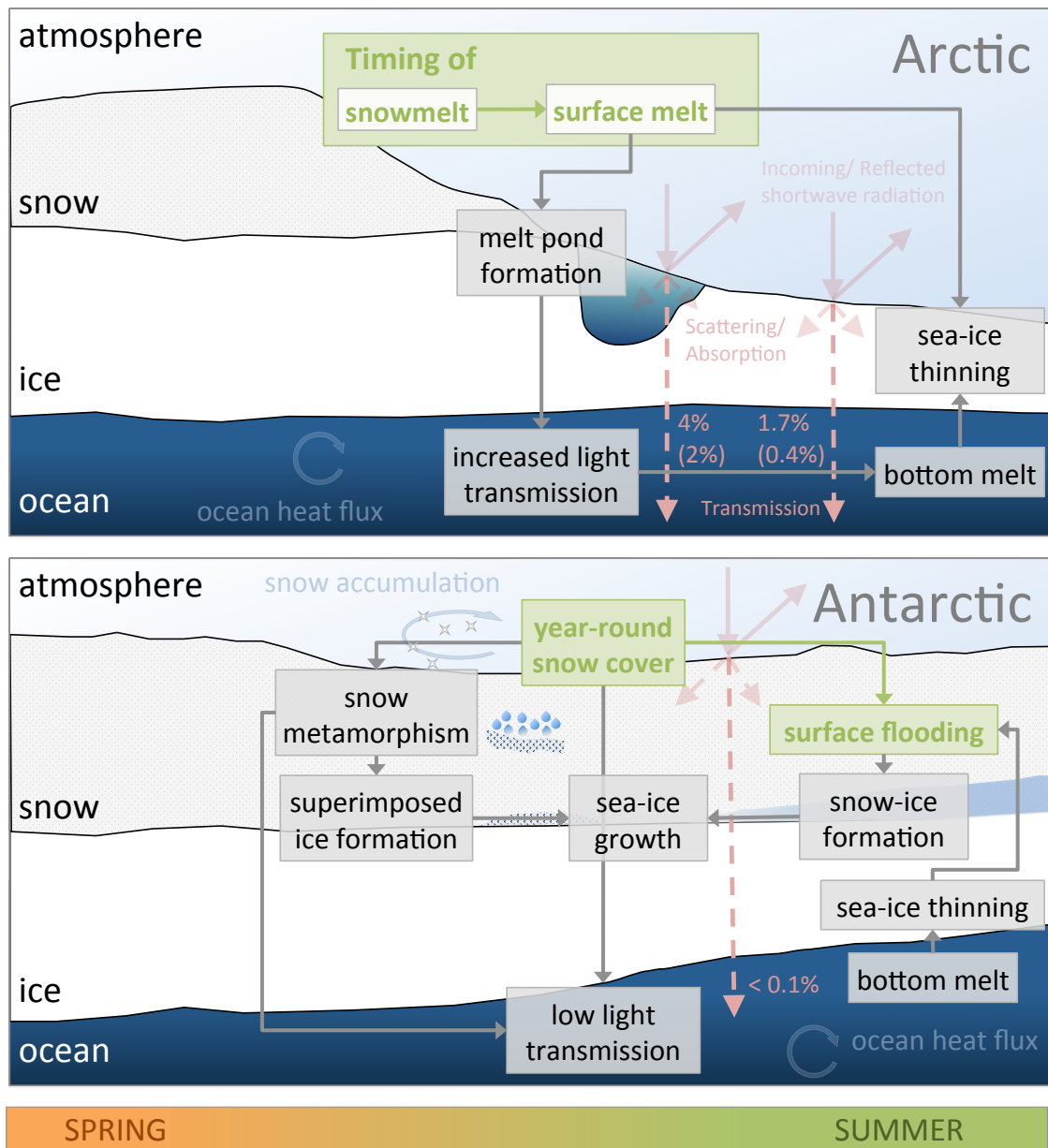


Figure 7.1: Schematic of dominant processes influencing the energy and mass budgets in the Arctic (upper panel) and Southern (lower panel) Oceans during the spring-summer transition. To highlight the opposing seasonal evolution of surface and bottom melt processes of Arctic and Antarctic sea ice, this schematic neglects that sea ice floats in an hydrostatic equilibrium. The radiation-arrow labels in the lower panel correspond to the ones in the upper panel. Light transmission values are given for the respective spring season. Arctic light transmission is given for bare and pond-covered first-year (multi-year) ice. Surface properties, which dominate the under-ice light field, are marked in green.

of light transmission through Arctic sea ice as a function of the seasonality of the respective surface properties. In order to obtain an Arctic-wide estimate, this parametrization was

7.1 Implications of seasonal effects on the sea-ice mass and energy budgets: A bi-polar view

applied to the entire ice-covered ocean in the northern hemisphere from 1979 to 2011. Since no long-term and consistent datasets of sea-ice thickness and snow depth are available to date, a simple sea-ice type classification (first-year and multi-year ice) is used as its proxy as well as an indicator of surface roughness and deformation.

Considering the entire Arctic sea-ice cover, 96 % of the annual solar heat input through sea ice occurs during only 4 months, from May to August - the period between initial surface melt and the end of the melt season in late summer. Since Arctic sea ice has been shown to become thinner, younger and more seasonal (e.g. Comiso, 2012; Haas et al., 2008; Maslanik et al., 2011, 2007), and the melt season has been extending (Markus et al., 2009), additional sensitivity studies focusing on the spring-summer transition were performed. Assuming that snowmelt starts two weeks earlier, the annual solar heat input into the upper ocean increases by 20 %. Continuing also the trend to a seasonal sea-ice cover only results in an increase in light transmission by another 18 %. Considering the period between 1979 and 2011, an annual increase in light transmission of 1.5 %, with regional maxima up to 4 %, was recorded. The higher light transmission increases the ocean heat flux, leading to an estimated annual bottom ice melt of up to 1.3 m. These results emphasize the increasing importance of basal melt for the Arctic sea-ice mass budget, leading to more basal- and internal-driven sea-ice thinning in the future (Figure 7.1).

Thus, the results of the present study highlight the direct dependency of seasonal and inter-annual changes of sea-ice surface properties and the Arctic energy and mass budgets. To quantify the effect of the changes in the physical environment on the ice-associated ecosystem, more comprehensive investigations of the bio-geo-physical interactions in the northern ice-covered ocean are needed. One of the key questions is, whether, e.g., the contribution of sub-ice algae to the primary productivity will increase with thinning sea ice or decrease with declining sea-ice extent due to increased phytoplankton blooms (Fernandez-Mendez et al., 2015). While local studies on the net primary production in the Arctic Ocean reveal a clear link between the seasonal sea-ice evolution and the local primary productivity, they also underline the lack of the temporal and spatial coverage of available data (Fernandez-Mendez et al., 2015; Lee et al., 2015).

Overall, the results of this thesis would benefit greatly from an improved Arctic-wide snow depth and sea-ice thickness data product, which would lower the uncertainty of the presented study (Section 7.2). While the seasonality of the snow cover drives the subsequent melt pond formation and therefore the small-scale under-ice light variability, sea-ice thickness determines the light transmission on larger scales (Katlein et al., 2015). The combination of improved sea-ice thickness and snow depth datasets with radiative transfer models would improve the quantification of the energy and mass budgets of Arctic sea ice during the spring-summer transition - the origin for major Arctic-wide changes.

Antarctic sea ice

Compared to the pronounced seasonal cycle of surface properties of Arctic sea ice, with its characteristic melt ponds and a mainly seasonal snow cover, Antarctic sea ice is very different. Its snow cover generally persists throughout the year, but undergoes substantial seasonal changes in its physical properties. The mechanisms that drive these changes and their timing are still unclear. Therefore, the second major part of the thesis (Chapter 4 and 5) focuses on processes in the snowpack during the spring-summer transition, when the biggest changes are expected. The analysis covers different regions around Antarctica, since, e.g., sea ice in the southern Weddell Sea is expected to have much more snow on top compared to areas in East Antarctica. The seasonal change of snow properties is initiated by diurnal freeze-thaw cycles in the snowpack, which are described by the diurnal variations in the brightness temperature, retrieved from passive microwave observations. In addition, the combination of different frequencies and polarizations allows for the retrieval of the continuous snowmelt onset in deeper snow layers (Section 7.2). Combining both snowmelt onsets reveals four surface regimes with substantial differences in their melt characteristics. The results of this study show evidence of diurnal freeze-thaw cycles in the surface snow layer in about 40 % of all detected melt events, which is characteristic of temporary melt. For another 12 % of the detected melt events, the temporary surface snowmelt leads to subsequent continuous snowmelt in deeper snow layers. Less than 2 % of the detected melt events reveal continuous melt only, while for about 48 %, no surface melt is observed at all.

In a next step, we investigated the timing of snow melt processes using daily brightness temperature values from 1988 to 2015. It was discovered that, in that period, no significant temporal trends for the timing of snowmelt processes in the Southern Ocean occur. Instead, the presented results show strong inter-annual variations in the derived melt onset dates and the spatial extent of the four characteristic surface types. Hence, the ongoing increase in sea-ice extent, sea-ice concentration, and ice season duration in certain regions of the Antarctic sea ice during the last decades is not reflected in inter-annual snowmelt variations, or vice versa. Examining the observed trend in sea-ice extent, it must be considered that its overall increase is composed of regionally contrasting sea-ice changes, in particular related to a decrease in the Bellingshausen and Amundsen Seas and an increase in the Ross Sea (Parkinson and Cavalieri, 2012; Stammerjohn et al., 2012; Turner et al., 2015). Several studies suggest to relate the observed changes to variations in the large-scale atmospheric circulation patterns and oceanic conditions (Turner et al., 2013a, 2015) (Section 2.4). The contrasting regional trend in sea-ice extent can be therefore related to the deepening of the Amundsen Sea Low (ASL) associated with a stronger meridional flow over the Ross Sea and a subsequently more extensive and longer-living sea-ice cover in the region (Stammerjohn et al., 2008; Turner et al., 2014). In contrast, stronger warm winds from the north along the limb at the Antarctic Peninsula speed up the sea-ice retreat

7.1 *Implications of seasonal effects on the sea-ice mass and energy budgets: A bi-polar view*

in the Bellingshausen Sea in spring and delay the sea-ice advance in autumn (Maksym et al., 2012; Turner et al., 2013a, 2015, 2016). Other studies have proposed enhanced basal melting from the Antarctic shelf resulting in a freshening of the Southern Ocean (Bintanja et al., 2013, 2015), changes in wind stress (Lefebvre and Goosse, 2008; Liu et al., 2004), and increasing near-surface winds (Holland and Kwok, 2012) as contributions to the enhanced sea-ice formation. To quantify the impacts of the changing polar environment on exchange processes across the air/snow and ice/ocean interface, further investigations on area-wide as well as local microwave satellite observations are needed (Section 7.2).

Moreover, comparisons of the snowmelt onsets, retrieved from the newly developed algorithm presented above, with in-situ snow depth data from autonomous monitoring systems suggest that neither temporary nor continuous snowmelt processes necessarily translate into changes in snow depth. Instead, both melt processes rather affect the internal stratigraphy and vertical density structure of the snowpack, leading to enhanced snow metamorphism and layering (Figure 7.1). While the diurnal freeze-thaw cycles at the surface mainly modify the optical properties of the snowpack through rounding and growth of snow grains, the continuous snowmelt potentially has important implications for the sea-ice mass budget of the Southern Ocean. For example, comparisons with studies by Haas (2001) reveal a coincidental spatial appearance of continuous snowmelt and superimposed ice formation in areas of perennial sea ice. The expected refreezing snow meltwater at the snow/ice interface leads to the sea-ice growth from the top, and thereby contributes to the annual sea-ice mass budget variations. Also, the prevalent snow cover amplifies the sea-ice growth from above due to initiated widespread flooding of the sea-ice surface and related snow-ice formation (Figure 7.1). Hence, snow volume loss is expected to result rather from snow-to-ice conversion at the bottom of the snowpack than by extensive snowmelt from the top.

Considering the importance of surface melt processes for the under-ice light field, as shown for the Arctic in Chapter 3, the question is now, whether a similar relation is valid for the Antarctic. Doing so, the third major part of this thesis (Chapter 6) links the surface properties of a representative Southern Ocean pack ice floe to the spectrally resolved under-ice irradiance. The results reveal extremely low light levels under the pack ice floe during austral spring, with a mean transmitted irradiance of less than 0.1%. Furthermore, it is shown how the distinction between flooded and non-flooded sea-ice regimes dominates the spatial scales of under-ice light variability for areas smaller than 100 m-by-100 m. The thicker snowpack, mainly present in flooded areas, acts as a strong scatterer and controls therefore the higher magnitude of the respective extinction coefficients compared to non-flooded areas. However, it is also evident from our study, that the heterogeneous and widely metamorphous snow on Antarctic sea ice prevents a direct correlation between surface properties and the under-ice light field. Hence, the procedure of an area-wide up-scaling of the under-ice light field, as described for the Arctic in Chapter 6, cannot easily be translated to the Southern Ocean. In order to implement that for the Antarctic, a

7 Key findings and Outlook

better understanding of the evolution of the physical properties within the snow cover and at the snow/ice interface, as well as the associated processes is required. Thus, the stages of snowmelt are crucial to estimate the strength of snow metamorphism in the snowpack as well as the likelihood of superimposed ice formation at the snow/ice interface. Again, reliable data sets of snow depth and sea-ice thickness from radar or passive microwave observations would allow for an additional Antarctic-wide estimation of sea-ice freeboard and a related quantification of flooding at the sea-ice surface. A combination of the described direct and indirect sea-ice variables will contribute for potential Antarctic-wide up-scaling approaches of the under-ice light field.

Overall, this thesis highlights the contrasting processes controlling the sea-ice energy and mass budgets of the Arctic and Southern Oceans. The variability of the under-ice light regime and its associated influence on the mass budget of Arctic sea ice is controlled by seasonal variations in the surface properties, and thus by the interactions at the air/snow- or air/sea-ice interface. In contrast, the mass and energy budgets of Antarctic sea ice are dominated by processes at the snow/ice interface as well as changing physical properties of the snowpack throughout the seasonal cycle. These distinct hemispheric differences play a major role for the retrieval of main sea-ice variables, such as sea-ice thickness, concentration, and age, from recent passive microwave and satellite scatterometer observations as well as model simulations.

7.2 Knowledge gain for remote sensing applications

Satellite remote sensing techniques are the only means to describe sea-ice characteristics on an Arctic- and Antarctic-wide scale. Several comprehensive studies exist that describe Arctic-wide different stages of sea-ice surface melt processes. In contrast, comparable studies that characterize seasonal changes in surface properties of Antarctic sea ice are largely missing. Willmes et al. (2009) detected the characteristic diurnal freeze-thaw cycles during the spring-summer transition on Antarctic sea ice from the diurnal difference in microwave brightness temperatures at 37 GHz using a fixed threshold (Section 7.1). However, the strength and depth of these freeze-thaw cycles is highly variable in space and time due to the heterogeneous snow properties and the prevalent atmospheric conditions. In an effort to better identify the crucially needed temporary snowmelt on Antarctic sea ice, Chapter 4 introduces a newly developed method to detect snowmelt on Antarctic sea ice based on individual local thresholds, which are applied to the described diurnal variations of the microwave brightness temperature at 37 GHz. In order to describe additional snowmelt processes below the penetration depth of passive microwaves with a frequency of 37 GHz, the 19 GHz channel was used to obtain subsurface melt processes deeper within the snowpack. The analysis of both passive microwave channels yielded a dataset of intermittent and continuous melt onsets. The application of both melt indicators allows

determining characteristic surface melt patterns on Antarctic sea ice.

In order to be able to resolve seasonal melt processes in the lower snowpack, an additional study based on the backscatter signal from satellite scatterometer sensors was performed in Chapter 5. The newly developed method uses the backscatter time series obtained from ERS-1/2, QSCAT and ASCAT missions with frequencies of 5.6 and 13.4 GHz, and corresponding deeper penetration depths than the previously described passive microwave signals. While Haas (2001) shows that the daily averaged backscatter coefficients over perennial sea ice reveal a rapid spring rise which is characteristic for snowmelt and intense superimposed ice formation at the snow/ice interface, preceding temporal rises indicate pre-melt conditions related to the initial change of physical properties in the lower snowpack. Comparing in this thesis the retrieved snowmelt onsets on perennial sea ice from satellite scatterometer and passive microwave observations, shows later onset dates from the scatterometer signal. This might be linked to the longer wavelengths of the scatterometer observations leading to a later response to snow grain growth, and the overall later snowmelt in deeper snow layers over cold perennial sea ice.

Studying diurnal variations in the backscatter signal during spring, as previously done for the microwave brightness temperature from passive microwave observations, allows to indicate the characteristic freeze-thaw cycles in the snowpack also from scatterometer observations. Comparing these results with the previously retrieved snowmelt onset dates from passive microwave observations reveals an overall good agreement between both onset dates for seasonal and perennial sea ice.

Both studies clearly show that only a combination of passive microwave and scatterometer observations yields the necessary understanding of the seasonal changes and relevant processes in the snowpack on Antarctic sea ice. On the one hand, the good agreement between melt onsets derived from diurnal variations in brightness temperature from passive microwave observations and backscatter coefficients from scatterometer observations allow for a higher spatial resolution of temporary snowmelt processes. On the other hand, the different penetration depths of satellite scatterometer and passive microwave observations enable a description of melt processes taking place at different depths within the snowpack. Passive microwave data allow to describe diurnal freeze-thaw cycles at the air/snow interface and continuous melt processes in the inner snowpack associated with increasing fresh water content and snow metamorphism, both initiated from changing atmospheric conditions. However, scatterometer observations are more sensitive to transition processes at the snow/ice interface, as the formation of superimposed ice, and changes in the oceanic heat flux of the Southern Ocean and the related heat transport to the snow/ice interface.

The additional knowledge gained from this thesis on snow processes and particularly on snowmelt onsets due to increasing fresh water in the Antarctic snowpack is crucial to increase the accuracy of various sea-ice data products based on satellite remote sensing.

7 Key findings and Outlook

A wet snowpack, for example, impacts and limits both the sea-ice concentration retrieval from passive microwave data (e.g. Comiso et al., 1992) and the sea-ice thickness and snow depth retrieval based on microwave radiometry and radar altimetry (Cavalieri et al., 2012; Kern et al., 2016; Kern and Ozsoy-Çiçek, 2016; Ricker et al., 2014). Thus, the newly obtained knowledge on the onset of increasing liquid water content at the air/snow and snow/ice interfaces provides the valid time frame for, e.g., reliable sea-ice thickness and snow depth retrievals, which primarily determine the Antarctic-wide sea-ice volume. Further, the extended knowledge about potential density changes of the snowpack due to enhanced internal melt processes and snow metamorphism is also helpful to increase the accuracy of the freeboard to thickness conversion of Antarctic sea ice, as for example used for CryoSat-2 data (Schwegmann et al., 2015). The temporary snowmelt onset in the upper snow layers and the associated increasing liquid water content, both early in the season, may also occur in the northern hemisphere. Thus, it is worth considering similar techniques to derive seasonal transition onsets on Arctic sea ice, as shown for the Southern Ocean, providing a valid time frame for reliable sea-ice thickness and snow depth retrievals.

7.3 Ideas for future field campaigns and research

An extensive field work program was carried out for the studies described in Chapters 3 and 6. This data was crucial to improve our understanding on light transmission through Arctic and Antarctic sea ice. The results from this thesis suggest crucial hemispheric differences in key parameters controlling the spatial variability of the under-ice light field. While the melt pond coverage and prevalent ice type determine the under-ice light field of Arctic sea ice during summer, the dominant heterogeneous snowpack on Antarctic sea ice prevents the description of optical properties as a function of sea-ice surface properties.

To improve the understanding of relations between the spatial variability of snow properties and the energy budget of Antarctic sea ice, the results in Chapter 6 suggest a more detailed analysis of the vertical (two-dimensional) snow structure co-located with light transmission measurements. This could be achieved by using high-resolution snow penetrometers to obtain information about the snow meso- and microstructure (Schneebeili et al., 1999). The obtained vertical profiles provide information on dominant stratigraphic structures, such as snow metamorphism, ice lenses, superimposed ice and snow-ice formation at the snow/ice interface. Moreover, the fast-acquired vertical profile (within a minute per profile) allows investigations on the spatial variability of, e.g., snow density by repeated measurements in a certain area (Proksch et al., 2015; Schneebeili et al., 1999). Combining the two-dimensional snow profile data, including density and microstructure, with under-ice solar radiation measurements is essential to better understand processes at the interfaces between snow, sea ice and ocean. The vertical snow structure and associated spatial variability of solar radiation under sea ice impacts not only the physical properties

7.3 Ideas for future field campaigns and research

but also biological processes and bio-geochemical fluxes in the sea ice and the uppermost ocean (Arrigo et al., 2012; Fritsen et al., 2011; Perovich, 1996, 2007). Due to their different spectral absorption characteristics, snow, sea ice, sea water, biota, sediments, and other impurities affect the spectral composition of the light penetrating from the air/snow interface to the upper ocean (Belzile et al., 2000; Mundy et al., 2005; Perovich, 1996; Uusikivi et al., 2010). An improved understanding of seasonal processes in the snowpack and at the snow/ice interface would therefore increase the accuracy of biota estimates based on the spectral composition of transmitted under-ice light measurements (Campbell et al., 2015; Mundy et al., 2007).

Moreover, also the interpretation of seasonal variations in scatterometer and passive microwave satellite observations of the Antarctic snowpack could benefit from the ability of detailed local snow stratigraphy. Even if ship-based field work is performed usually during summer or even freeze-up conditions in the Southern Ocean, the vertical (density) structure of the snow could give indications on the intensity and vertical propagation of melt processes within the snowpack. In addition, to account for seasonal changes in the Antarctic snowpack, local observations from networks of autonomous systems can be used. Platforms, such as Ice Mass-balance Buoys (IMBs), allow for the description of detailed vertical temperature and conductivity profiles from the air/snow interface through the snow and ice column down to the upper ocean. The vertical profiles can be analyzed to detect temporal and small-scale changes in the snowpack, and especially at the snow/ice interface. This information combined with the retrieved snowmelt onsets from scatterometer and passive microwave satellite observations help to improve our understanding on penetration depth and microstructure disturbances within the snowpack on the microwave signals.

The case study conducted on a single pack ice floe in the Weddell Sea (Chapter 6) demonstrates how flooding of the sea-ice surface dominates the under-ice light variability for areas smaller 100 m-by-100 m. On larger scales, the light transmitted into the ocean through leads and breaks between the ice floes is suggested to determine the under-ice light regime. Consequently, the depth of maximum light intensity is expected to be found in deeper ocean layers, rather than at the ice/ocean interface. Hence, the general under-ice light regime would rather be a function of floe size than of (snow) surface properties. To confirm this hypothesis, future field work on light transmission measurements under Antarctic sea ice should focus on both horizontal and vertical profiling through the under-ice water column to quantify the potential lateral light incidence. In contrast, the marginal ice zone is characterized by a lower sea-ice concentration than the inner pack ice, with a much smaller floe size and even higher surface variability. This outer sea-ice belt is therefore expected to show different relations between sea-ice properties and the under-ice light field.

While the present thesis represents the first steps towards a better understanding on

7 Key findings and Outlook

key parameters driving the annual energy and mass budgets, a better coverage of sea-ice thickness, snow depth and transmitted solar radiation measurements is needed to extrapolate the results. Therefore, one should distinguish between different priorities and ways to acquire the needed data. Networks of autonomous platforms, such as Snow and Ice Mass-balance Buoys as well as autonomous radiation stations, allow to observe seasonal changes on one floe drifting with the current sea-ice motion through the Arctic and Southern Oceans. Since flooding of the sea-ice surface is identified as the key process governing the variability of sea-ice surface growth and the under-ice light field in the Southern Ocean, it is suggested to select both flooded and non-flooded floes for future deployments of autonomous platforms. To account for a better coverage of small- and large-scale spatial variabilities, as well as a detailed analysis of relations between the under-ice solar radiation and sea-ice and snow properties, it is mandatory to conduct in addition comprehensive ship-based field work in different characteristic regions (marginal ice zone, first-year ice, multi-year ice) in the Arctic and Antarctic sea-ice regime.

Bibliography

- Abdalati, W. and Steffen, K.: Passive Microwave-Derived Snow Melt Regions on the Greenland Ice-Sheet, *Geophysical Research Letters*, 22, 787–790, doi:10.1029/95gl00433, 1995.
- Abdalati, W. and Steffen, K.: Snowmelt on the Greenland ice sheet as derived from passive microwave satellite data, *Journal of Climate*, 10, 165–175, doi:10.1175/1520-0442(1997)010%3C0165:Sotgis%3E2.0.Co;2, 1997.
- Andersen, S., Breivik, L., Eastwood, S., Godoy, O., Lind, M., Porcires, M., and Schyberg, H.: OSI SAF Sea Ice Product Manual–v3. 5, EUMETSAT OSI SAF–Ocean and Sea Ice Sattelite Application Facility, Tech. rep., Tech. Rep. SAF/OSI/met. no/TEC/MA/125, 2007.
- Andreas, E. L. and Ackley, S. F.: On the differences in ablation seasons of Arctic and Antarctic sea ice, *Journal of the Atmospheric Sciences*, 39, 440–447, doi:10.1175/1520-0469(1982)039%3C0440:otdias%3E2.0.co;2, 1982.
- Armstrong, R., Knowles, K., Brodzik, M. J., and Hardman, M. A.: DMSP SSM/I-SSMIS Pathfinder Daily EASE-Grid Brightness Temperatures. Version 2, Tech. rep., NASA DAAC National Snow and Ice Data Center Distributed Active Archive Center: Boulder, CO, USA, doi:10.5067/3EX2U1DV3434., 1994.
- Arndt, S.: Seasonality and spatial distribution of soar radiation under Arctic sea ice, Master thesis, University of Hamburg, Germany, 2013.
- Arndt, S. and Nicolaus, M.: Seasonal cycle and long-term trend of solar energy fluxes through Arctic sea ice, *The Cryosphere*, 8, 2219–2233, doi:10.5194/tc-8-2219-2014, 2014.
- Arndt, S., Willmes, S., Dierking, W., and Nicolaus, M.: Timing and regional patterns of snowmelt on Antarctic sea ice from passive microwave satellite observations, *Journal of Geophysical Research: Oceans*, 121, 5916–5930, doi:10.1002/2015JC011504, 2016.
- Arndt, S., Meiners, K. M., Ricker, R., Krumpfen, T., Katlein, C., and Nicolaus, M.: Influence of snow depth and surface flooding on light transmission through Antarctic pack ice, *Journal of Geophysical Research: Oceans*, under review.

Bibliography

- Arrigo, K. R.: Sea ice ecosystems, *Annual Review of Marine Science*, 6, 439–467, doi:10.1146/annurev-ma-7-120414-100001, 2014.
- Arrigo, K. R., Perovich, D. K., Pickart, R. S., Brown, Z. W., van Dijken, G. L., Lowry, K. E., Mills, M. M., Palmer, M. A., Balch, W. M., Bahr, F., Bates, N. R., Benitez-Nelson, C., Bowler, B., Brownlee, E., Ehn, J. K., Frey, K. E., Garley, R., Laney, S. R., Lubelczyk, L., Mathis, J., Matsuoka, A., Mitchell, B. G., Moore, G. W. K., Ortega-Retuerta, E., Pal, S., Polashenski, C. M., Reynolds, R. A., Schieber, B., Sosik, H. M., Stephens, M., and Swift, J. H.: Massive Phytoplankton Blooms Under Arctic Sea Ice, *Science*, 336, 1408–1408, doi:10.1126/science.1215065, 2012.
- Ashcraft, I. S. and Long, D. G.: Increasing temporal resolution in greenland ablation estimation using passive and active microwave data, in: *Geoscience and Remote Sensing Symposium, 2003. IGARSS 2003. Proceedings. 2003 IEEE International*, vol. 3, pp. 1604–1606, IEEE, doi:10.1109/IGARSS.2003.1294190, 2003.
- Barber, D. G., Papakyriakou, T. N., Ledrew, E. F., and Shokr, M. E.: An Examination of the Relation between the Spring Period Evolution of the Scattering Coefficient (Sigma-Degrees) and Radiative Fluxes over Landfast Sea-Ice, *International Journal of Remote Sensing*, 16, 3343–3363, doi:10.1080/01431169508954634, 1995.
- Barber, D. G., Fung, A. K., Grenfell, T. C., Nghiem, S. V., Onstott, R. G., Lytle, V. I., Perovich, D. K., and Gow, A. J.: The role of snow on microwave emission and scattering over first-year sea ice, *IEEE Transactions on Geoscience and Remote Sensing*, 36, 1750–1763, doi:10.1109/36.718643, 1998.
- Belchansky, G. I., Douglas, D. C., and Platonov, N. G.: Duration of the Arctic Sea ice melt season: Regional and interannual variability, 1979-2001, *Journal of Climate*, 17, 67–80, doi:10.1175/1520-0442(2004)017%3C0067:Dotasi%3E2.0.Co;2, 2004.
- Belzile, C., Johannessen, S. C., Gosselin, M., Demers, S., and Miller, W. L.: Ultraviolet attenuation by dissolved and particulate constituents of first-year ice during late spring in an Arctic polynya, *Limnology and Oceanography*, 45, 1265–1273, doi:10.4319/lo.2000.45.6.1265, 2000.
- Bintanja, R., van Oldenborgh, G. J., Drijfhout, S. S., Wouters, B., and Katsman, C. A.: Important role for ocean warming and increased ice-shelf melt in Antarctic sea-ice expansion, *Nature Geoscience*, 6, 376–379, doi:10.1038/Ngeo1767, 2013.
- Bintanja, R., Van Oldenborgh, G. J., and Katsman, C. A.: The effect of increased fresh water from Antarctic ice shelves on future trends in Antarctic sea ice, *Annals of Glaciology*, 56, 120–126, doi:10.3189/2015AoG69A001, 2015.

- Boebel, O.: The Expedition PS89 of the Research Vessel POLARSTERN to the Weddell Sea in 2014/2015, *Berichte zur Polar-und Meeresforschung= Reports on polar and marine research*, 689, 2015.
- Brandt, R. E. and Warren, S. G.: Solar-heating rates and temperature profiles in Antarctic snow and ice, *Journal of Glaciology*, 39, 99–110, doi:10.3198/1993JoG39-131-99-110, 1993.
- Brandt, R. E., Warren, S. G., Worby, A. P., and Grenfell, T. C.: Surface albedo of the Antarctic sea ice zone, *Journal of Climate*, 18, 3606–3622, doi:10.1175/Jcli3489.1, 2005.
- Campbell, K., Mundy, C. J., Barber, D. G., and Gosselin, M.: Characterizing the sea ice algae chlorophyll a-snow depth relationship over Arctic spring melt using transmitted irradiance, *Journal of Marine Systems*, 147, 76–84, doi:10.1016/j.jmarsys.2014.01.008, 2015.
- Cavalieri, D. J. and Parkinson, C. L.: Antarctic sea ice variability and trends, 1979-2006, *Journal of Geophysical Research: Oceans*, 113, doi:10.1029/2007jc004564, 2008.
- Cavalieri, D. J. and Parkinson, C. L.: Arctic sea ice variability and trends, 1979-2010, *The Cryosphere*, 6, 881–889, doi:10.5194/tc-6-881-2012, 2012.
- Cavalieri, D. J., Gloersen, P., and Campbell, W. J.: Determination of Sea Ice Parameters with the Nimbus-7 Smmr, *Journal of Geophysical Research: Atmospheres*, 89, 5355–5369, doi:10.1029/Jd089id04p05355, 1984.
- Cavalieri, D. J., Markus, T., Ivanoff, A., Miller, J. A., Brucker, L., Sturm, M., Maslanik, J. A., Heinrichs, J. F., Gasiewski, A. J., Leuschen, C., Krabill, W., and Sonntag, J.: A Comparison of Snow Depth on Sea Ice Retrievals Using Airborne Altimeters and an AMSR-E Simulator, *IEEE Transactions on Geoscience and Remote Sensing*, 50, 3027–3040, doi:10.1109/tgrs.2011.2180535, 2012.
- Chuvieco, E. and Huete, A.: *Fundamentals of satellite remote sensing*, CRC press, doi: 10.1111/j.1477-9730.2010.00613.x, 2009.
- Coggins, J. H. J. and McDonald, A. J.: The influence of the Amundsen Sea Low on the winds in the Ross Sea and surroundings: Insights from a synoptic climatology, *Journal of Geophysical Research: Atmospheres*, 120, 2167–2189, doi:10.1002/2014jd022830, 2015.
- Colbeck, S. C.: *A Review of Sintering in Seasonal Snow*, Report, DTIC Document, 1997.
- Comiso, J. C.: Sea Ice Effective Microwave Emissivities from Satellite Passive Microwave and Infrared Observations, *Journal of Geophysical Research: Oceans and Atmospheres*, 88, 7686–7704, doi:10.1029/JC088iC12p07686, 1983.

Bibliography

- Comiso, J. C.: Bootstrap sea ice concentrations from Nimbus-7 SMMR and DMSP SSM/I. Version 2. National Snow and Ice Data Center, Tech. rep., NASA DAAC National Snow and Ice Data Center Distributed Active Archive Center: Boulder, CO, USA, doi:10.5067/J6JQLS9EJ5HU, 2000.
- Comiso, J. C.: Variability and Trends of the Global Sea Ice Cover, vol. 2, book section 6, pp. 205–246, Wiley-Blackwell, doi:10.1002/9781444317145.ch6, 2010.
- Comiso, J. C.: Large decadal decline of the Arctic multiyear ice cover, *Journal of Climate*, 25, 1176–1193, doi:10.1175/JCLI-D-11-00113.1, 2012.
- Comiso, J. C. and Nishio, F.: Trends in the sea ice cover using enhanced and compatible AMSR-E, SSM/I, and SMMR data, *Journal of Geophysical Research: Oceans*, 113, doi:10.1029/2007JC004257, 2008.
- Comiso, J. C., Grenfell, T. C., Lange, M., Lohanick, A. W., Moore, R. K., and Wadhams, P.: Microwave remote sensing of the Southern Ocean ice cover, vol. *Geophysical Monograph* 68, pp. 243–259, American Geophysical Union, doi:10.1029/GM068p0243, 1992.
- Comiso, J. C., Cavalieri, D. J., Parkinson, C. L., and Gloersen, P.: Passive microwave algorithms for sea ice concentration: A comparison of two techniques, *Remote Sensing of Environment*, 60, 357–384, doi:10.1016/S0034-4257(96)00220-9, 1997.
- Curry, J. A., Schramm, J. L., and Ebert, E. E.: Sea ice-albedo climate feedback mechanism, *Journal of Climate*, 8, 240–247, doi:10.1175/1520-0442(1995)008%3C0240:SIACFM%3E2.0.CO;2, 1995.
- Deal, C., Jin, M. B., Elliott, S., Hunke, E., Maltrud, M., and Jeffery, N.: Large-scale modeling of primary production and ice algal biomass within arctic sea ice in 1992, *Journal of Geophysical Research: Oceans*, 116, doi:10.1029/2010JC006409, 2011.
- Dee, D. P., Uppala, S. M., Simmons, A. J., Berrisford, P., Poli, P., Kobayashi, S., Andrae, U., Balmaseda, M. A., Balsamo, G., and Bauer, P.: The ERA-Interim reanalysis: Configuration and performance of the data assimilation system, *Quarterly Journal of the Royal Meteorological Society*, 137, 553–597, doi:10.1002/qj.828, 2011.
- Dieckmann, G. S. and Hellmer, H. H.: The importance of Sea Ice: An Overview, vol. 2, book section 1, pp. 1–22, Wiley-Blackwell, doi:10.1002/9781444317145.ch1, 2010.
- Drinkwater, M. R. and Liu, X.: Seasonal to interannual variability in Antarctic sea-ice surface melt, *IEEE Transactions on Geoscience and Remote Sensing*, 38, 1827–1842, doi:10.1109/36.851767, 2000.

- Drobot, S. D. and Anderson, M. R.: An improved method for determining snowmelt onset dates over Arctic sea ice using scanning multichannel microwave radiometer and Special Sensor Microwave/Imager data, *Journal of Geophysical Research: Atmospheres*, 106, 24 033–24 049, doi:10.1029/2000jd000171, 2001.
- Ducklow, H. W., Baker, K., Martinson, D. G., Quetin, L. B., Ross, R. M., Smith, R. C., Stammerjohn, S. E., Vernet, M., and Fraser, W.: Marine pelagic ecosystems: the west Antarctic Peninsula, *Philosophical Transactions of the Royal Society of London B: Biological Sciences*, 362, 67–94, doi:10.1098/rstb.2006.1955, 2007.
- Eicken, H., Lange, M. A., Hubberten, H. W., and Wadhams, P.: Characteristics and distribution patterns of snow and meteoric ice in the Weddell Sea and their contribution to the mass balance of sea ice, *Annales Geophysicae: Atmospheres, Hydrospheres and Space Sciences*, 12, 80–93, doi:10.1007/s00585-994-0080-x, 1994.
- Eicken, H., Fischer, H., and Lemke, P.: Effects of the snow cover on Antarctic sea ice and potential modulation of its response to climate change, *Annals of Glaciology*, 21, 369–376, doi:10.3198/1995AoG21-1-369-376, 1995.
- Eppler, D. T., Farmer, L. D., Lohanick, A. W., Anderson, M. R., Cavalieri, D. J., Comiso, J. C., Gloersen, P., Garrity, C., Grenfell, T. C., and Hallikainen, M.: Passive Microwave Signatures of Sea Ice, book section 4, pp. 47–71, American Geophysical Union, *Geophysical Monograph* 68, Washington, D. C., doi:10.1029/GM068p0047, 1992.
- Ezraty, R. and Cavanié, A.: Intercomparison of backscatter maps over Arctic sea ice from NSCAT and the ERS scatterometer, *Journal of Geophysical Research: Oceans*, 104, 11 471–11 483, 1999.
- Fernandez-Mendez, M., Katlein, C., Rabe, B., Nicolaus, M., Peeken, I., Bakker, K., Flores, H., and Boetius, A.: Photosynthetic production in the central Arctic Ocean during the record sea-ice minimum in 2012, *Biogeosciences*, 12, 3525–3549, doi:10.5194/bg-12-3525-2015, 2015.
- Fetterer, F.: *Sea Ice Index: Interpretation Resources for Sea Ice Trends and Anomalies.*, NSIDC Informal Technical Report, 2002.
- Ficek, D., Kaczmarek, S., Ston-Egiert, J., Wozniak, B., Majchrowski, R., and Dera, J.: Spectra of light absorption by phytoplankton pigments in the Baltic; conclusions to be drawn from a Gaussian analysis of empirical data, *Oceanologia*, 46, 533–555, 2004.
- Flocco, D., Schroeder, D., Feltham, D. L., and Hunke, E. C.: Impact of melt ponds on Arctic sea ice simulations from 1990 to 2007, *Journal of Geophysical Research: Oceans*, 117, doi:10.1029/2012JC008195, 2012.

Bibliography

- Fogt, R. L. and Wovrosh, A. J.: The Relative Influence of Tropical Sea Surface Temperatures and Radiative Forcing on the Amundsen Sea Low, *Journal of Climate*, 28, 8540–8555, doi:10.1175/Jcli-D-15-0091.1, 2015.
- Foster, J. L., Hall, D. K., Chang, A. T. C., and Rango, A.: An overview of passive microwave snow research and results, *Reviews of Geophysics*, 22, 195–208, doi:10.1029/RG022i002p00195, 1984.
- Frey, K. E., Perovich, D. K., and Light, B.: The spatial distribution of solar radiation under a melting Arctic sea ice cover, *Geophysical Research Letters*, 38, doi:10.1029/2011GL049421, 2011.
- Fritsen, C. H., Ackley, S. F., Kremer, J. N., and Sullivan, C. W.: Flood-Freeze Cycles and Microalgal Dynamics in Antarctic Pack Ice, *Antarctic sea ice: biological processes, interactions and variability*, pp. 1–21, 1998.
- Fritsen, C. H., Wirthlin, E. D., Momberg, D. K., Lewis, M. J., and Ackley, S. F.: Bio-optical properties of Antarctic pack ice in the early austral spring, *Deep-Sea Research Part II: Topical Studies in Oceanography*, 58, 1052–1061, doi:10.1016/j.dsr2.2010.10.028, 2011.
- Garrity, C.: Characterization of snow on floating ice and case studies of brightness temperature changes during the onset of melt, vol. 68, journal article 16, pp. 313–328, American Geophysical Union, Washington, D. C, doi:10.1029/GM068p0313, 1992.
- Gloersen, P., Campbell, W. J., Cavalieri, D. J., Comiso, J. C., Parkinson, C. L., and Zwally, H. J.: Arctic and Antarctic sea ice, 1978-1987: Satellite passive-microwave observations and analysis, NASA Publication, Washington, DC., p. 290 pp., 1992.
- Grenfell, T. C. and Maykut, G. A.: The optical properties of ice and snow in the Arctic Basin, *Journal of Glaciology*, 18, 445–463, doi:10.3198/1977JoG18-80-445-463, 1977.
- Grenfell, T. C., Light, B., and Perovich, D. K.: Spectral transmission and implications for the partitioning of shortwave radiation in arctic sea ice, *Annals of Glaciology*, 44, 1–6, doi:10.3189/172756406781811763, 2006.
- Haas, C.: The seasonal cycle of ERS scatterometer signatures over perennial Antarctic sea ice and associated surface ice properties and processes, *Annals of Glaciology*, 33, 69–73, doi:10.3189/172756401781818301, 2001.
- Haas, C., Thomas, D. N., and Bareiss, J.: Surface properties and processes of perennial Antarctic sea ice in summer, *Journal of Glaciology*, 47, 613–625, doi:10.3189/172756501781831864, 2001.

- Haas, C., Pfaffling, A., Hendricks, S., Rabenstein, L., Etienne, J. L., and Rigor, I.: Reduced ice thickness in Arctic Transpolar Drift favors rapid ice retreat, *Geophysical Research Letters*, 35, doi:10.1029/2008GL034457, 2008.
- Haas, C., Hendricks, S., Eicken, H., and Herber, A.: Synoptic airborne thickness surveys reveal state of Arctic sea ice cover, *Geophysical Research Letters*, 37, doi:10.1029/2010GL042652, 2010.
- Hallikainen, M. and Winebrenner, D. P.: The physical basis for sea ice remote sensing, book section 3, pp. 29–46, American Geophysical Union, doi:10.1029/GM068p0029, 1992.
- Hellmer, H. H., Haas, C., Dieckmann, G. S., and Schröder, M.: Sea ice feedbacks observed in western Weddell Sea, *Eos, Transactions, American Geophysical Union*, 87, 173–179, doi:10.1029/eost2006EO18, 2006.
- Holland, P. R. and Kwok, R.: Wind-driven trends in Antarctic sea-ice drift, *Nature Geoscience*, 5, 872–875, doi:10.1038/ngeo1627, 2012.
- Hudson, S. R., Granskog, M. A., Sundfjord, A., Randelhoff, A., Renner, A. H. H., and Divine, D. V.: Energy budget of first-year Arctic sea ice in advanced stages of melt, *Geophysical Research Letters*, 40, 2679–2683, doi:10.1002/grl.50517, 2013.
- Hunkeler, P. A., Hendricks, S., Hoppmann, M., Paul, S., and Gerdes, R.: Towards an estimation of sub-sea-ice platelet-layer volume with multi-frequency electromagnetic induction sounding, *Annals of Glaciology*, 56, 137–146, doi:10.3189/2015AoG69A705, 2015.
- Hunkeler, P. A., Hendricks, S., Hoppmann, M., Farquharson, C. G., Kalscheuer, T., Grab, M., Kaufmann, M. S., Rabenstein, L., and Gerdes, R.: Improved 1D inversions for sea ice thickness and conductivity from electromagnetic induction data: Inclusion of nonlinearities caused by passive bucking, *Geophysics*, 81, Wa45–Wa58, doi:10.1190/Geo2015-0130.1, 2016.
- Huwald, H., Tremblay, L., and Blatter, H.: Reconciling different observational data sets from Surface Heat Budget of the Arctic Ocean (SHEBA) for model validation purposes, *Journal of Geophysical Research: Oceans*, 110, doi:10.1029/2003JC002221, 2005.
- Jeffries, M. O., Worby, A. P., Morris, K., and Weeks, W. F.: Seasonal variations in the properties and structural composition of sea ice and snow cover in the Bellingshausen and Amundsen seas, Antarctica, *Journal of Glaciology*, 43, 138–151, doi:10.3198/1997JoG43-143-138-151, 1997.

Bibliography

- Katlein, C., Nicolaus, M., and Petrich, C.: The anisotropic scattering coefficient of sea ice, *Journal of Geophysical Research: Oceans*, 119, 842–855, doi:10.1002/2013JC009502, 2014.
- Katlein, C., Arndt, S., Nicolaus, M., Perovich, D. K., Jakuba, M. V., Suman, S., Elliott, S., Whitcomb, L. L., McFarland, C. J., Gerdes, R., Boetius, A., and German, C. R.: Influence of ice thickness and surface properties on light transmission through Arctic sea ice, *Journal of Geophysical Research: Oceans*, 120, 5932–5944, doi:10.1002/2015jc010914, 2015.
- Katlein, C., Perovich, D. K., and Nicolaus, M.: Geometric Effects of an Inhomogeneous Sea Ice Cover on the under Ice Light Field, *Frontiers in Earth Science*, 4, 6, doi:10.3389/feart.2016.00006, 2016.
- Kern, S. and Ozsoy-Çiçek, B.: Satellite Remote Sensing of Snow Depth on Antarctic Sea Ice: An Inter-Comparison of Two Empirical Approaches, *Remote Sensing*, 8, 450, doi:10.3390/rs8060450, 2016.
- Kern, S., Ozsoy-Çiçek, B., and Worby, A. P.: Antarctic Sea-Ice Thickness Retrieval from ICESat: Inter-Comparison of Different Approaches, *Remote Sensing*, 8, 538, doi:10.3390/rs8070538, 2016.
- Knight, C. A.: Formation of slush on floating ice, *Cold Regions Science and Technology*, 15, 33–38, doi:10.1016/0165-232X(88)90035-3, 1988.
- König-Langlo, G.: Continuous meteorological surface measurement during POLARSTERN cruise ANT-XXIX/7, doi:10.1594/PANGAEA.858532, URL <https://doi.pangaea.de/10.1594/PANGAEA.858532>, 2016.
- Krishfield, R., Toole, J., Proshutinsky, A., and Timmermans, M. L.: Automated Ice-Tethered Profilers for Seawater Observations under Pack Ice in All Seasons, *Journal of Atmospheric and Oceanic Technology*, 25, 2091–2105, doi:10.1175/2008JTECHO587.1, 2008.
- Kwok, R.: Annual cycles of multiyear sea ice coverage of the Arctic Ocean: 1999–2003, *Journal of Geophysical Research: Oceans*, 109, C11 004, doi:10.1029/2003JC002238, 2004.
- Kwok, R. and Rothrock, D. A.: Decline in Arctic sea ice thickness from submarine and ICESat records: 1958–2008, *Geophysical Research Letters*, 36, doi:10.1029/2009gl039035, 2009.
- Lange, M. A., Schlosser, P., Ackley, S. F., Wadhams, P., and Dieckmann, G. S.: O-18 Concentrations in Sea Ice of the Weddell Sea, Antarctica, *Journal of Glaciology*, 36, 315–323, doi:10.3189/002214390793701291, 1990.

- Lavergne, T., Killie, M. A., Eastwood, S., and Breivik, L.-A.: Extending the CryoClim Arctic sea ice extent time series with operational OSI SAF products from 2008 onwards, Tech. rep., Norwegian Meteorological Institute, 2010.
- Laxon, S. W., Giles, K. A., Ridout, A. L., Wingham, D. J., Willatt, R., Cullen, R., Kwok, R., Schweiger, A., Zhang, J. L., Haas, C., Hendricks, S., Krishfield, R., Kurtz, N., Farrell, S., and Davidson, M.: CryoSat-2 estimates of Arctic sea ice thickness and volume, *Geophysical Research Letters*, 40, 732–737, doi:10.1002/grl.50193, 2013.
- Lee, Y., Matrai, P. A., Friedrichs, M. A. M., Saba, V. S., Antoine, D., Ardyna, M., Asanuma, I., Babin, M., Belanger, S., Benoit-Gagne, M., Devred, E., Fernandez-Mendez, M., Gentili, B., Hirawake, T., Kang, S. H., Kameda, T., Katlein, C., Lee, S. H., Lee, Z. P., Melin, F., Scardi, M., Smyth, T. J., Tang, S., Turpie, K. R., Waters, K. J., and Westberry, T. K.: An assessment of phytoplankton primary productivity in the Arctic Ocean from satellite ocean color/in situ chlorophyll-a based models, *Journal of Geophysical Research: Oceans*, 120, 6508–6541, doi:10.1002/2015jc011018, 2015.
- Lefebvre, W. and Goosse, H.: An analysis of the atmospheric processes driving the large-scale winter sea ice variability in the Southern Ocean, *Journal of Geophysical Research: Oceans*, 113, doi:10.1029/2006JC004032, 2008.
- Lemke, P.: The expedition of the research vessel "Polarstern" to the Antarctic in 2006 (ANT-XXIII/7), *Berichte zur Polar-und Meeresforschung (Reports on Polar and Marine Research)*, 586, 2009.
- Lemke, P., Trinkl, E., and Hasselmann, K.: Stochastic dynamic analysis of polar sea ice variability, *Journal of Physical Oceanography*, 10, 2100–2120, doi:10.1175/1520-0485, 1980.
- Leu, E., Wiktor, J., Soreide, J. E., Berge, J., and Falk-Petersen, S.: Increased irradiance reduces food quality of sea ice algae, *Marine Ecology Progress Series*, 411, 49–60, doi:10.3354/meps08647, 2010.
- Lieser, J. L., Massom, R. A., Fraser, A. D., Haward, M. G., Heil, P., Lannuzel, D., Meiners, K., Melbourne-Thomas, J., Press, A. J., and Williams, G. D.: Position analysis: Antarctic sea ice and climate change 2014, Report, Antarctic Climate and Ecosystems Cooperative Research Centre, Hobart, Tasmania, Australia, 2014.
- Light, B., Grenfell, T. C., and Perovich, D. K.: Transmission and absorption of solar radiation by Arctic sea ice during the melt season, *Journal of Geophysical Research: Oceans*, 113, doi:10.1029/2006JC003977, 2008.
- Lindsay, R. and Schweiger, A.: Arctic sea ice thickness loss determined using subsurface, aircraft, and satellite observations, *The Cryosphere*, 9, 269–283, doi:10.5194/tc-9-269-2015, 2015.

Bibliography

- Lindsay, R., Wensnahan, M., Schweiger, A., and Zhang, J.: Evaluation of Seven Different Atmospheric Reanalysis Products in the Arctic*, *Journal of Climate*, 27, 2588–2606, doi:10.1175/JCLI-D-13-00014.1, 2014.
- Liu, J. P., Curry, J. A., and Martinson, D. G.: Interpretation of recent Antarctic sea ice variability, *Geophysical Research Letters*, 31, doi:10.1029/2003gl018732, 2004.
- Livingstone, C. E., Onstott, R. G., Arsenault, L. D., and Singh, K. P.: Microwave sea-ice signatures near the onset of melt, *IEEE Transactions on Geoscience and Remote Sensing*, GE-25, 174–187, doi:10.1109/TGRS.1987.289816, 1987.
- Long, D. G., Hardin, P. J., and Whiting, P. T.: Resolution Enhancement of Spaceborne Scatterometer Data, *IEEE Transactions on Geoscience and Remote Sensing*, 31, 700–715, doi:10.1109/36.225536, 1993.
- Lubin, D. and Massom, R.: *Polar Remote Sensing: Volume I: Atmosphere and Oceans*, Springer Science and Business Media, 2006.
- Maksym, T., Stammerjohn, S. E., Ackley, S., and Massom, R.: Antarctic Sea Ice-A Polar Opposite?, *Oceanography*, 25, 140–151, doi:10.5670/oceanog.2012.88, 2012.
- Markus, T., Cavalieri, D. J., Gasiewski, A. J., Klein, M., Maslanik, J. A., Powell, D. C., Stankov, B. B., Stroeve, J. C., and Sturm, M.: Microwave signatures of snow on sea ice: Observations, *IEEE Transactions on Geoscience and Remote Sensing*, 44, 3081–3090, doi:10.1109/TGRS.2006.883134, 2006.
- Markus, T., Stroeve, J. C., and Miller, J. A.: Recent changes in Arctic sea ice melt onset, freezeup, and melt season length, *Journal of Geophysical Research: Oceans*, 114, C12024, doi:10.1029/2009JC005436, 2009.
- Martinson, D. G.: Antarctic circumpolar current’s role in the Antarctic ice system: An overview, *Palaeogeography, Palaeoclimatology, Palaeoecology*, 335, 71–74, doi:10.1016/j.palaeo.2011.04.007, 2012.
- Martinson, D. G. and Iannuzzi, R. A.: Antarctic Ocean–ice interaction: Implications from ocean bulk property distributions in the Weddell Gyre, Wiley Online Library, doi:10.1029/AR074p0243, 1998.
- Maslanik, J. and Stroeve, J.: Near-real-time DMSP SSM/I-SSMIS daily polar gridded sea ice concentrations, National Snow and Ice Data Center, Boulder, CO, digital media., URL http://nsidc.org/data/docs/daac/nsidc0081_ssmi_nrt_seaice.gd.html, 1999.
- Maslanik, J., Stroeve, J., Fowler, C., and Emery, W.: Distribution and trends in Arctic sea ice age through spring 2011, *Geophysical Research Letters*, 38, doi:10.1029/2011GL047735, 2011.

- Maslanik, J. A., Fowler, C., Stroeve, J., Drobot, S., Zwally, J., Yi, D., and Emery, W.: A younger, thinner Arctic ice cover: Increased potential for rapid, extensive sea-ice loss, *Geophysical Research Letters*, 34, doi:10.1029/2007GL032043, 2007.
- Massom, R. A. and Stammerjohn, S. E.: Antarctic sea ice change and variability—physical and ecological implications, *Polar Science*, 4, 149–186, doi:10.1016/j.polar.2010.05.001, 2010.
- Massom, R. A., Eicken, H., Haas, C., Jeffries, M. O., Drinkwater, M. R., Sturm, M., Worby, A. P., Wu, X. R., Lytle, V. I., Ushio, S., Morris, K., Reid, P. A., Warren, S. G., and Allison, I.: Snow on Antarctic Sea ice, *Reviews of Geophysics*, 39, 413–445, doi:10.1029/2000rg000085, 2001.
- Matear, R. J., O’Kane, T. J., Risbey, J. S., and Chamberlain, M.: Sources of heterogeneous variability and trends in Antarctic sea-ice, *Nature communications*, 6, doi:10.1038/ncomms9656, 2015.
- Mätzler, C. and Hüppi, R.: Review of signature studies for microwave remote sensing of snowpacks, *Advances in Space Research*, 9, 253–265, doi:10.1016/0273-1177(89)90493-6, 1989.
- Maykut, G. A. and Untersteiner, N.: Some results from a time-dependent thermodynamic model of sea ice, *Journal of Geophysical Research: Oceans*, 76, 1550–1575, doi:10.1029/JC076i006p01550, 1971.
- Meier, W. N., Hovelsrud, G. K., Oort, B. E. H., Key, J. R., Kovacs, K. M., Michel, C., Haas, C., Granskog, M. A., Gerland, S., and Perovich, D. K.: Arctic sea ice in transformation: A review of recent observed changes and impacts on biology and human activity, *Reviews of Geophysics*, 52, 185–217, doi:10.1002/2013RG000431, 2014.
- Meiners, K. M., Golden, K. M., Heil, P., Lieser, J. L., Massom, R., Meyer, B., and Williams, G. D.: Introduction: SIPEX-2: A study of sea-ice physical, biogeochemical and ecosystem processes off East Antarctica during spring 2012, *Deep Sea Research Part II: Topical Studies in Oceanography*, doi:10.1016/j.dsr2.2016.06.010, 2016.
- Melbourne-Thomas, J., Meiners, K. M., Mundy, C., Schallenberg, C., Tattersall, K. L., and Dieckmann, G. S.: Algorithms to estimate Antarctic sea ice algal biomass from under-ice irradiance spectra at regional scales, *Marine Ecology Progress Series*, 536, 107–121, doi:10.3354/meps11396, 2015.
- Meyer, B. and Auerswald, L.: The expedition of the research vessel “Polarstern” to the Antarctic in 2013 (ANT-XXIX/7), *Berichte zur Polar-und Meeresforschung= Reports on polar and marine research*, 674, 2014.

Bibliography

- Michael, K. J. and Higgins, J.: Diffuse Attenuation Coefficients for East Antarctic Pack Ice and Snow at Ultraviolet and Visible Wavelengths, *Ieee Transactions on Geoscience and Remote Sensing*, 52, 4455–4461, doi:10.1109/Tgrs.2013.2282158, 2014.
- Mortin, J., Schrøder, T. M., Walløe Hansen, A., Holt, B., and McDonald, K. C.: Mapping of seasonal freeze–thaw transitions across the pan–Arctic land and sea ice domains with satellite radar, *Journal of Geophysical Research: Oceans*, 117, doi:10.1029/2012JC008001, 2012.
- Mortin, J., Howell, S. E. L., Wang, L. B., Derksen, C., Svensson, G., Graversen, R. G., and Schroder, T. M.: Extending the QuikSCAT record of seasonal melt-freeze transitions over Arctic sea ice using ASCAT, *Remote Sensing of Environment*, 141, 214–230, doi:10.1016/J.Rse.2013.11.004, 2014.
- Mundy, C. J., Barber, D. G., and Michel, C.: Variability of snow and ice thermal, physical and optical properties pertinent to sea ice algae biomass during spring, *Journal of Marine Systems*, 58, 107–120, doi:10.1016/j.jmarsys.2005.07.003, 2005.
- Mundy, C. J., Ehn, J. K., Barber, D. G., and Michel, C.: Influence of snow cover and algae on the spectral dependence of transmitted irradiance through Arctic landfast first-year sea ice, *Journal of Geophysical Research: Oceans*, 112, doi:10.1029/2006JC003683, 2007.
- Nghiem, S. V., Rigor, I. G., Clemente-Colón, P., Neumann, G., and Li, P. P.: Geophysical constraints on the Antarctic sea ice cover, *Remote Sensing of Environment*, 181, 281–292, doi:10.1016/j.rse.2016.04.005, 2016.
- Nicholls, K. W., Østerhus, S., Makinson, K., Gammelsrød, T., and Fahrback, E.: Ice–ocean processes over the continental shelf of the southern Weddell Sea, Antarctica: A review, *Reviews of Geophysics*, 47, doi:10.1029/2007RG000250, 2009.
- Nicolaus, M. and Katlein, C.: Mapping radiation transfer through sea ice using a remotely operated vehicle (ROV), *The Cryosphere*, 7, 763–777, doi:10.5194/Tc-7-763-2013, 2013.
- Nicolaus, M., Haas, C., and Bareiss, J.: Observations of superimposed ice formation at melt-onset on fast ice on Kongsfjorden, Svalbard, *Physics and Chemistry of the Earth*, 28, 1241–1248, doi:10.1016/j.pce.2003.08.048, 2003.
- Nicolaus, M., Haas, C., Bareiss, J., and Willmes, S.: A model study of differences of snow thinning on Arctic and Antarctic first-year sea ice during spring and summer, *Annals of Glaciology*, 44, 147–153, doi:10.3189/172756406781811312, 2006.
- Nicolaus, M., Haas, C., and Willmes, S.: Evolution of first-year and second-year snow properties on sea ice in the Weddell Sea during spring–summer transition, *Journal of Geophysical Research: Oceans*, 114, doi:10.1029/2008JD011227, 2009.

- Nicolaus, M., Gerland, S., Hudson, S. R., Hanson, S., Haapala, J., and Perovich, D. K.: Seasonality of spectral albedo and transmittance as observed in the Arctic Transpolar Drift in 2007, *Journal of Geophysical Research: Oceans*, 115, doi:10.1029/2009JC006074, 2010a.
- Nicolaus, M., Hudson, S. R., Gerland, S., and Munderloh, K.: A modern concept for autonomous and continuous measurements of spectral albedo and transmittance of sea ice, *Cold Regions Science and Technology*, 62, 14–28, doi:10.1016/j.coldregions.2010.03.001, 2010b.
- Nicolaus, M., Katlein, C., Maslanik, J., and Hendricks, S.: Changes in Arctic sea ice result in increasing light transmittance and absorption, *Geophysical Research Letters*, 39, doi:10.1029/2012GL053738, 2012.
- Nicolaus, M., Arndt, S., Katlein, C., Maslanik, J., and Hendricks, S.: Correction to “Changes in Arctic sea ice result in increasing light transmittance and absorption”, *Geophysical Research Letters*, 40, 2699–2700, doi:10.1002/grl.50523, 2013.
- Onstott, R. G. and Shuchman, R. A.: SAR measurements of sea ice, vol. 3, pp. 81–115, National Oceanic and Atmospheric Administration, Washington, DC, 2004.
- Overland, J. E. and Wang, M.: Large-scale atmospheric circulation changes are associated with the recent loss of Arctic sea ice, *Tellus A*, 62, 1–9, doi:10.1111/j.1600-0870.2009.00421.x, 2010.
- Overland, J. E. and Wang, M. Y.: Future regional Arctic sea ice declines, *Geophysical Research Letters*, 34, doi:10.1029/2007gl030808, 2007.
- Parkinson, C. L. and Cavalieri, D. J.: Antarctic sea ice variability and trends, 1979–2010, *The Cryosphere*, 6, 871–880, doi:10.5194/tc-6-871-2012, 2012.
- Parkinson, C. L. and Washington, W. M.: A large-scale numerical model of sea ice, *Journal of Geophysical Research: Oceans*, 84, 311–337, doi:10.1029/JC084iC01p00311, 1979.
- Perovich, D. K.: Theoretical estimates of light-reflection and transmission by spatially complex and temporally varying sea ice covers, *Journal of Geophysical Research: Oceans*, 95, 9557–9567, doi:10.1029/JC095iC06p09557, 1990.
- Perovich, D. K.: Seasonal changes in sea ice optical properties during fall freeze-up, *Cold Regions Science and Technology*, 19, 261–273, doi:10.1016/%200165-232X(91)90041-E, 1991.
- Perovich, D. K.: *The Optical Properties of Sea Ice*, Report, U.S. Cold Reg. Res. and Eng. Lab. Monogr., 1996.

Bibliography

- Perovich, D. K.: UV radiation and the optical properties of sea ice and snow, UV radiation and Arctic ecosystems. Berlin, Springer Verlag, pp. 73–89, 2001.
- Perovich, D. K.: Light reflection and transmission by a temperate snow cover, *Journal of Glaciology*, 53, 201–210, doi:10.3189/172756507782202919, 2007.
- Perovich, D. K. and Polashenski, C.: Albedo evolution of seasonal Arctic sea ice, *Geophysical Research Letters*, 39, doi:10.1029/2012GL051432, 2012.
- Perovich, D. K. and Richter-Menge, J. A.: Loss of Sea Ice in the Arctic*, *Annual Review of Marine Science*, 1, 417–441, doi:10.1146/annurev.marine.010908.163805, 2009.
- Perovich, D. K., Elder, B. C., and Richter-Menge, J. A.: Observations of the annual cycle of sea ice temperature and mass balance, *Geophysical Research Letters*, 24, 555–558, doi:10.1029/97GL00185, 1997.
- Perovich, D. K., Roesler, C. S., and Pegau, W. S.: Variability in Arctic sea ice optical properties, *Journal of Geophysical Research: Oceans*, 103, 1193–1208, doi:10.1029/97JC01614, 1998.
- Perovich, D. K., Grenfell, T. C., Light, B., and Hobbs, P. V.: Seasonal evolution of the albedo of multiyear Arctic sea ice, *Journal of Geophysical Research: Oceans*, 107, doi:10.1029/2000JC000438, 2002.
- Perovich, D. K., Light, B., Eicken, H., Jones, K. F., Runciman, K., and Nghiem, S. V.: Increasing solar heating of the Arctic Ocean and adjacent seas, 1979–2005: Attribution and role in the ice-albedo feedback, *Geophysical Research Letters*, 34, doi:10.1029/2007GL031480, 2007a.
- Perovich, D. K., Nghiem, S. V., Markus, T., and Schweiger, A.: Seasonal evolution and interannual variability of the local solar energy absorbed by the Arctic sea ice-ocean system, *Journal of Geophysical Research: Oceans*, 112, doi:10.1029/2006JC003558, 2007b.
- Perovich, D. K., Jones, K. F., Light, B., Eicken, H., Markus, T., Stroeve, J., and Lindsay, R.: Solar partitioning in a changing Arctic sea-ice cover, *Annals of Glaciology*, 52, 192–196, doi:10.3189/172756411795931543, 2011a.
- Perovich, D. K., Richter-Menge, J. A., Jones, K. F., Light, B., Elder, B. C., Polashenski, C., Laroche, D., Markus, T., and Lindsay, R.: Arctic sea-ice melt in 2008 and the role of solar heating, *Annals of Glaciology*, 52, 355–359, doi:10.3189/172756411795931714, 2011b.
- Popova, E. E., Yool, A., Coward, A. C., Dupont, F., Deal, C., Elliott, S., Hunke, E., Jin, M. B., Steele, M., and Zhang, J. L.: What controls primary production in the Arctic

- Ocean? Results from an intercomparison of five general circulation models with biogeochemistry, *Journal of Geophysical Research: Oceans*, 117, doi:10.1029/2011JC007112, 2012.
- Proksch, M., Lowe, H., and Schneebeli, M.: Density, specific surface area, and correlation length of snow measured by high-resolution penetrometry, *Journal of Geophysical Research: Earth Surface*, 120, 346–362, doi:10.1002/2014jf003266, 2015.
- Rees, W. G.: Remote sensing of snow and ice, CRC press, 2005.
- Renner, A. H. H., Gerland, S., Haas, C., Spreen, G., Beckers, J. F., Hansen, E., Nicolaus, M., and Goodwin, H.: Evidence of Arctic sea ice thinning from direct observations, *Geophysical Research Letters*, 41, 5029–5036, doi:10.1002/2014gl060369, 2014.
- Ricker, R., Hendricks, S., Helm, V., Skourup, H., and Davidson, M.: Sensitivity of CryoSat-2 Arctic sea-ice freeboard and thickness on radar-waveform interpretation, *The Cryosphere*, 8, 1607–1622, doi:10.5194/tc-8-1607-2014, 2014.
- Ridler, T. W. and Calvard, S.: Picture thresholding using an iterative selection method, *IEEE Trans. Syst. Man Cybern.*, SMC-8, 630–632, 1978.
- Rösel, A. and Kaleschke, L.: Exceptional melt pond occurrence in the years 2007 and 2011 on the Arctic sea ice revealed from MODIS satellite data, *Journal of Geophysical Research: Oceans*, 117, doi:10.1029/2011JC007869, 2012.
- Rösel, A., Kaleschke, L., and Birnbaum, G.: Melt ponds on Arctic sea ice determined from MODIS satellite data using an artificial neural network, *The Cryosphere*, 6, 431–446, doi:10.5194/tc-6-431-2012, 2012.
- Sandven, S., Johannessen, O., and Kloster, K.: Sea ice monitoring by remote sensing, inbook 8, pp. 241–283, American Society for Photogrammetry and Remote Sensing, 3 edn., doi:10.1002/9780470027318.a2320, 2006.
- Schmitt, C., Wassermann, S., Drinkwater, M., and Kottmeier, C.: Atlas of Antarctic Sea Ice Drift, Universität Karlsruhe. Institut für Meteorologie und Klimaforschung, 2004.
- Schneebeli, M., Pielmeier, C., and Johnson, J. B.: Measuring snow microstructure and hardness using a high resolution penetrometer, *Cold Regions Science and Technology*, 30, 101–114, doi:10.1016/S0165-232X(99)00030-0, 1999.
- Schröder, D., Feltham, D. L., Flocco, D., and Tsamados, M.: September Arctic sea-ice minimum predicted by spring melt-pond fraction, *Nature Climate Change*, 4, 353–357, doi:10.1038/nclimate2203, 2014.

Bibliography

- Schwegmann, S., Rinne, E., Ricker, R., Hendricks, S., and Helm, V.: About the consistency between Envisat and CryoSat-2 radar freeboard retrieval over Antarctic sea ice, *The Cryosphere Discuss.*, 9, 4893–4923, doi:10.5194/tcd-9-4893-2015, 2015.
- Sedlar, J., Tjernström, M., Mauritsen, T., Shupe, M. D., Brooks, I. M., Persson, P. O. G., Birch, C. E., Leck, C., Sirevaag, A., and Nicolaus, M.: A transitioning Arctic surface energy budget: the impacts of solar zenith angle, surface albedo and cloud radiative forcing, *Climate Dynamics*, 37, 1643–1660, doi:10.1007/s00382-010-0937-5, 2011.
- Shokr, M.: Field observations and model calculations of dielectric properties of Arctic sea ice in the microwave C-band, *IEEE Transactions on Geoscience and Remote Sensing*, 36, 463–478, doi:10.1109/36.662730, 1998.
- Shokr, M. and Sinha, N.: *Ice Physics and Physical Processes*, John Wiley and Sons, , Ltd: New York, NY, USA Sons, doi:10.1002/9781119028000.ch2, 2015.
- Smith, S. D., Muench, R. D., and Pease, C. H.: Polynyas and leads: an overview of physical processes and environment, *Journal of Geophysical Research: Oceans*, 95, 9461–9479, doi:10.1029/JC095iC06p09461, 1990.
- Spreen, G., Kaleschke, L., and Heygster, G.: Sea ice remote sensing using AMSR-E 89-GHz channels, *Journal of Geophysical Research: Oceans*, 113, doi:10.1029/2005jc003384, 2008.
- Spreen, G., Kwok, R., and Menemenlis, D.: Trends in Arctic sea ice drift and role of wind forcing: 1992–2009, *Geophysical Research Letters*, 38, doi:10.1029/2011GL048970, 2011.
- Stammerjohn, S., Massom, R., Rind, D., and Martinson, D.: Regions of rapid sea ice change: An inter-hemispheric seasonal comparison, *Geophysical Research Letters*, 39, doi:10.1029/2012GL050874, 2012.
- Stammerjohn, S. E., Martinson, D. G., Smith, R. C., Yuan, X., and Rind, D.: Trends in Antarctic annual sea ice retreat and advance and their relation to El Niño–Southern Oscillation and Southern Annular Mode variability, *Journal of Geophysical Research: Oceans*, 113, doi:10.1029/2007JC004269, 2008.
- Stroeve, J. C., Serreze, M. C., Holland, M. M., Kay, J. E., Malanik, J., and Barrett, A. P.: The Arctic’s rapidly shrinking sea ice cover: a research synthesis, *Climatic Change*, 110, 1005–1027, doi:10.1007/S10584-011-0101-1, 2012.
- Stroeve, J. C., Markus, T., Boisvert, L., Miller, J., and Barrett, A.: Changes in Arctic melt season and implications for sea ice loss, *Geophysical Research Letters*, 41, 1216–1225, doi:10.1002/2013GL058951, 2014.

- Sturm, M. and Massom, R. A.: Snow and Sea Ice, vol. 2, pp. 153–204, Wiley-Blackwell, doi:10.1002/9781444317145.ch5, 2010.
- Sturm, M., Holmgren, J., and Perovich, D. K.: Winter snow cover on the sea ice of the Arctic Ocean at the Surface Heat Budget of the Arctic Ocean (SHEBA): Temporal evolution and spatial variability, *Journal of Geophysical Research: Oceans*, 107, doi:10.1029/2000JC000400, 2002.
- Taylor, M. H., Losch, M., and Bracher, A.: On the drivers of phytoplankton blooms in the Antarctic marginal ice zone: A modeling approach, *Journal of Geophysical Research: Oceans*, 118, 63–75, doi:10.1029/2012jc008418, 2013.
- Tedesco, M.: Remote Sensing of the Cryosphere, John Wiley and Sons, , Ltd: New York, NY, USA, 2015.
- Thomas, D. N. and Dieckmann, G. S.: Antarctic sea ice—a habitat for extremophiles, *Science*, 295, 641–644, doi:10.1126/science.1063391, 2002.
- Turner, J. and Overland, J.: Contrasting climate change in the two polar regions, *Polar Research*, 28, 146–164, doi:10.1111/j.1751-8369.2009.00128.x, 2009.
- Turner, J., Bracegirdle, T. J., Phillips, T., Marshall, G. J., and Hosking, J. S.: An Initial Assessment of Antarctic Sea Ice Extent in the CMIP5 Models, *Journal of Climate*, 26, 1473–1484, doi:10.1175/Jcli-D-12-00068.1, 2013a.
- Turner, J., Phillips, T., Hosking, J. S., Marshall, G. J., and Orr, A.: The Amundsen Sea low, *International Journal of Climatology*, 33, 1818–1829, doi:10.1002/joc.3558, 2013b.
- Turner, J., Barrand, N. E., Bracegirdle, T. J., Convey, P., Hodgson, D. A., Jarvis, M., Jenkins, A., Marshall, G., Meredith, M. P., Roscoe, H., Shanklin, J., French, J., Goosse, H., Guglielmin, M., Gutt, J., Jacobs, S., Kennicutt, M. C., Masson-Delmotte, V., Mayewski, P., Navarro, F., Robinson, S., Scambos, T., Sparrow, M., Summerhayes, C., Speer, K., and Klepikov, A.: Antarctic climate change and the environment: an update, *Polar Record*, 50, 237–259, doi:10.1017/S0032247413000296, 2014.
- Turner, J., Hosking, J. S., Bracegirdle, T. J., Marshall, G. J., and Phillips, T.: Recent changes in Antarctic sea ice, *Philosophical Transactions of the Royal Society of London A: Mathematical, Physical and Engineering Sciences*, 373, 20140163, doi:10.1098/rsta.2014.0163, 2015.
- Turner, J., Hosking, J. S., Marshall, G. J., Phillips, T., and Bracegirdle, T. J.: Antarctic sea ice increase consistent with intrinsic variability of the Amundsen Sea Low, *Climate Dynamics*, 46, 2391–2402, doi:10.1007/s00382-015-2708-9, 2016.

Bibliography

- Ulaby, F., Moore, R. K., and Fung, A. K.: Microwave Remote Sensing. Active and Passive. Vol. 3. From Theory to Applications., Addison Wesley Pub., London, U.K., doi:10.1017/S0016756800015831, 1986.
- Uusikivi, J., Vahatalo, A. V., Granskog, M. A., and Sommaruga, R.: Contribution of mycosporine-like amino acids and colored dissolved and particulate matter to sea ice optical properties and ultraviolet attenuation, *Limnology and Oceanography*, 55, 703–713, doi:10.4319/lo.2009.55.2.0703, 2010.
- Wang, C., Granskog, M. A., Gerland, S., Hudson, S. R., Perovich, D. K., Nicolaus, M., Ivan Karlsen, T., Fossan, K., and Bratrein, M.: Autonomous observations of solar energy partitioning in first-year sea ice in the Arctic Basin, *Journal of Geophysical Research: Oceans*, 119, 2066–2080, doi:10.1002/2013JC009459, 2014.
- Warren, S. G.: Optical properties of snow, *Reviews of Geophysics*, 20, 67–89, doi:10.1029/RG020i001p00067, 1982.
- Wassmann, P. and Reigstad, M.: Future Arctic Ocean Seasonal Ice Zones and Implications for Pelagic-Benthic Coupling, *Oceanography*, 24, 220–231, 2011.
- Webster, M. A., Rigor, I. G., Perovich, D. K., Richter-Menge, J. A., Polashenski, C. M., and Light, B.: Seasonal evolution of melt ponds on Arctic sea ice, *Journal of Geophysical Research: Oceans*, 120, 5968–5982, doi:10.1002/2015JC011030, 2015.
- Weeks, W. F. and Ackley, S. F.: *The Growth, Structure, and Properties of Sea Ice*, pp. 9–164, Springer US, doi:10.1007/978-1-4899-5352-0_2, 1986.
- Williams, G. D., Maksym, T., Kunz, C., Kimball, P., Singh, H., Wilkinson, J., Lachlan-Cope, T., Trujillo, E., Steer, A., Massom, R., Meiners, K., Heil, P., Lieser, J., and Leonard, K.: Beyond Point Measurements: Sea Ice Floes Characterized in 3-D, *Eos, Transactions American Geophysical Union*, 94, 69–70, doi:10.1002/2013EO070002, 2013.
- Willmes, S.: Characterization of the snowmelt period on Antarctic sea ice during summer through remote sensing and field measurements, Phd thesis, 2007.
- Willmes, S., Bareiss, J., Haas, C., and Nicolaus, M.: The importance of diurnal processes for the seasonal cycle of sea-ice microwave brightness temperatures during early summer in the Weddell Sea, Antarctica, *Annals of Glaciology*, 44, 297–302, doi:10.3189/172756406781811817, 2006.
- Willmes, S., Haas, C., Nicolaus, M., and Bareiss, J.: Satellite microwave observations of the interannual variability of snowmelt on sea ice in the Southern Ocean, *Journal of Geophysical Research: Oceans*, 114, doi:10.1029/2008jc004919, 2009.

- Willmes, S., Nicolaus, M., and Haas, C.: The microwave emissivity variability of snow covered first-year sea ice from late winter to early summer: a model study, *The Cryosphere*, 8, 891–904, doi:10.5194/tc-8-891-2014, 2014.
- Winebrenner, D. P., Long, D. G., and Holt, B.: Mapping the progression of melt onset and freeze-up on Arctic sea ice using SAR and scatterometry, pp. 129–144, Springer Berlin, doi:10.1007/978-3-642-60282-5_7, 1998.
- Worby, A. P., Markus, T., Steer, A. D., Lytle, V. I., and Massom, R. A.: Evaluation of AMSR-E snow depth product over East Antarctic sea ice using in situ measurements and aerial photography, *Journal of Geophysical Research: Oceans*, 113, doi:10.1029/2007jc004181, 2008.
- Worby, A. P., Steer, A., Lieser, J. L., Heil, P., Yi, D. H., Markus, T., Allison, I., Massom, R. A., Galin, N., and Zwally, J.: Regional-scale sea-ice and snow thickness distributions from in situ and satellite measurements over East Antarctica during SIPEX 2007, *Deep-Sea Research Part II: Topical Studies in Oceanography*, 58, 1125–1136, doi:10.1016/j.dsr2.2010.12.001, 2011.
- Yackel, J. J., Barber, D. G., Papakyriakou, T. N., and Breneman, C.: First-year sea ice spring melt transitions in the Canadian Arctic Archipelago from time-series synthetic aperture radar data, 1992–2002, *Hydrological Processes*, 21, 253–265, doi:10.1002/Hyp.6240, 2007.
- Yi, D., Zwally, H. J., and Robbins, J. W.: ICESat observations of seasonal and interannual variations of sea-ice freeboard and estimated thickness in the Weddell Sea, Antarctica (2003–2009), *Annals of Glaciology*, 52, 43–51, doi:10.3189/172756411795931480, 2011.
- Yuan, X. J.: ENSO-related impacts on Antarctic sea ice: a synthesis of phenomenon and mechanisms, *Antarctic Science*, 16, 415–425, doi:10.1017/S0954102004002238, 2004.
- Zwally, H. J., Comiso, J. C., Parkinson, C. L., Cavalieri, D. J., and Gloersen, P.: Variability of Antarctic sea ice 1979–1998, *Journal of Geophysical Research: Oceans*, 107, doi:10.1029/2000jc000733, 2002.

List of Figures

1.1	Schematic of dominant processes and interaction of Arctic and Antarctic sea ice.	2
2.1	Arctic and Antarctic sea-ice concentration in 2016.	8
2.2	Photographs of level sea ice with a distinct lead and ridged sea ice.	9
2.3	Schematic of the seasonal cycle of surface properties of Arctic and Antarctic sea ice.	11
2.4	Schematic of processes modifying the mass budget of sea ice.	12
2.5	Overview of Arctic and Antarctic regions.	13
2.6	Monthly mean Arctic and Antarctic sea-ice extent in March and September.	14
2.7	Schematic of the microwave brightness temperature and its emission depth.	18
3.1	Schematic of the surface energy budget of sea ice.	27
3.2	Seasonality of surface properties and associated sea-ice types.	29
3.3	Annual cycle of light transmittance for pond covered and bare sea ice.	31
3.4	Monthly mean of total solar heat input under Arctic sea ice for the year 2011.	36
3.5	Average and trend of the annual total solar heat input through Arctic sea from 1979 to 2011.	38
3.6	Arctic-wide annual and monthly solar heat flux under sea ice and its trend from 1979 to 2011.	39
3.7	Comparison between parameterization and measurements during the drift of Tara in 2007.	41
3.8	Changes in annual total solar heat input through sea ice in 2011, resulting from a sensitivity study assuming an extended melt season.	44
3.9	Variograms of surface albedo, sea-ice draft and light transmittance.	47
4.1	Eight example time series of diurnal variations in brightness temperature and the cross-polarized ratio from July 2004 to June 2005.	54
4.2	Flowchart of the snowmelt onset retrieval algorithm.	56
4.3	One example grid cell of a multi- and uni-modal distribution of dT_B and its spatial distribution for the example melt season 2004/2005.	57

List of Figures

4.4	Individual transition threshold, Temporary Snowmelt Onset, and Continuous Snowmelt Onset for the melt transition 2004/2005.	59
4.5	Classification of Antarctic sea ice into four characteristic snowmelt types for the seasons from 1988/1989 to 2014/2015.	60
4.6	Derived standard deviations for the individual transition threshold, the Temporary Snowmelt Onset, and the Continuous Snowmelt Onset for the melt transition 2004/2005.	62
4.7	Snow Buoy tracks and their daily averaged snow depth and air temperature during the expected melt season 2014/2015.	65
4.8	Spatial extent of melt types and dates of Temporary Snowmelt Onset and Continuous Snowmelt Onset from 1988/1989 to 2014/2015.	67
5.1	Map of the Antarctic showing the 12 study locations on perennial sea ice.	72
5.2	Example time series of the daily backscatter signal, its diurnal variations and the diurnal brightness temperature variations, and its respective melt onset dates.	75
5.3	Example of a multi- and uni-modal distribution of $d\sigma^0$ and its spatial distribution in 2004/2005.	77
5.4	Time series of backscatter signals from 1992 to 2014 with denoted melt/transition onset dates from passive and microwave observations.	78
5.5	Initial transition onset and snowmelt onset retrieved from daily and diurnal active microwave observations in 2004/2005.	79
5.6	Difference between transition dates retrieved from Ku-Band and C-Band for the study locations.	80
5.7	Point-to-point difference between melt onset dates retrieved from Ku-Band and C-Band.	81
5.8	Point-to-point differences between transition dates retrieved from passive and active microwave observations in 2004/2005.	83
5.9	Mean differences between retrieved snowmelt onset from scatterometer and passive microwave observations from 1992/1993 to 2014/2015.	84
5.10	Time series of retrieved spring-summer transition from daily backscatter signals and its diurnal variations from 1992/1993 to 2014/2015.	86
6.1	Ice-station location sampled during voyage ANT-29/7 in the Weddell Sea in September 2013.	92
6.2	Weather conditions during the ice camp from 18 to 26 September 2013.	93
6.3	Two typical states of Antarctic sea ice.	94
6.4	Physical properties of the ice floe within the Remotely Operated Vehicle (ROV) survey area.	97
6.5	Histograms of examined physical properties.	98

List of Figures

6.6 Correlation surfaces of normalized difference indices (NDI). 99

6.7 Spectral light transmittance and bulk extinction coefficients. 101

7.1 Schematic of dominant processes modifying the energy and mass budgets
of Arctic and Antarctic sea ice. 108

List of Tables

3.1	Transmittance values of different sea-ice and surface types.	34
3.2	Data sources of the different parameters used in this study.	35
3.3	Annual Arctic-wide solar heat input (and relative changes) under sea ice in 2011 for the reference method and several sensitivity studies.	45
4.1	Sensitivity study on different sea-ice concentration thresholds for the retrieval Temporary Snowmelt Onset and Continuous Snowmelt Onset for the melt transition 2004/2005.	64
6.1	Summary statistics for measured and calculated physical sea-ice parameters for the PS81 data set.	96

Acknowledgements

First and foremost, I would like to thank Marcel Nicolaus for his outstanding support during the last years. You always found the right words to guide me through my time as a PhD student, and gave me so many suggestions, hints and feedbacks for manuscripts, presentations, and the everyday-life, in- and outside science. Moreover, we had a great time during our joint fieldwork in Antarctica and several conferences and meetings. For me, you have always been not just a great advisor, but have become a close friend.

I am also grateful to my supervisors Peter Lemke and Christian Haas who will not only review this thesis, but also supported this thesis and myself, and gave always very constructive remarks.

I am grateful to my PhD committee at AWI, including Peter Lemke, Christian Haas, Marcel Nicolaus and Wolfgang Dierking. Together with Sascha Willmes (University of Trier), you gave me always great support, feedbacks and suggestions for my current and future work.

I would like to thank for the support of the Alfred-Wegener-Institut Helmholtz-Zentrum für Polar- und Meeresforschung providing all logistics for the realized expeditions during my PhD time, as well as all needed materials and working space in Bremerhaven.

Furthermore, I would like to acknowledge the support of the Helmholtz Alliance ‘Remote Sensing and Earth System Dynamics’ (HA-310), not only for the funding but especially for the possibility of studying in an interdisciplinary framework during several project meetings and workshops. Therefore, I would like to thank in particular Angelika Humbert, the leader of the Cryosphere working package, who always supported my work.

Many thanks to POLMAR, and especially to Claudia Hanfland and Claudia Sprengel for their great personal and financial support for conferences and my studies abroad.

I would like to thank the entire AWI Sea-Ice Physics section including former and present colleagues, particularly Marcel Nicolaus, Robert Ricker, Priska Hunkeler, Mario Hoppmann, Stephan Paul, Anja Nicolaus, Christian Katlein, Leonard Rossmann, Marcus Huntemann, Martin Schiller, Stefan Hendricks, Thomas Krumpfen, Polona Itkin, Valeria Selyuzhenok, Giulia Castellani, Kathrin Riemann-Campe, Michael Karcher, Frank Kauker, Hiroshi Sumata, Sandra Schwegmann, Hannes Schulz, Ingrid Linck-Rosenhaim

Acknowledgements

and Louisa Tiemann, and many other AWI colleagues, for a nice and warm working atmosphere that made me always feel being not only at work but spending time with my second family.

Special thanks go to Klaus Meiners for the warm welcome and incredible time at IMAS in Hobart (Tasmania) for 2.5 months. I am looking forward to come back at some point and spend an other great time with you and Tony Worby, Rob Massom, Guy Williams, Petra Heil and all young researchers.

I had the possibility to join three expeditions on R/V Polarstern during my PhD time. I want to thank everybody who made this possible and especially the chief scientists (Antje Boetius, Olaf Böbel and Michael Schröder) and the respective captains and crew on board.

Finally, I would like to express my deepest gratitude to my parents and my brother who always support me, whatever I do and wherever I go.

Stefanie Arndt

Curriculum Vitae

Bussestraße 27–29
D-27570 Bremerhaven
☎ +49 471 4831 2707
✉ stefanie.arndt@awi.de

In Person

Nationality German
Birth Date 30.10.1988
Place of Birth Berlin, Germany

Education

- Oct 2013– Dec 2016 **PhD Candidate**, *University of Bremen, Alfred-Wegener-Institut Helmholtz-Zentrum für Polar- und Meeresforschung*, Bremerhaven, Germany.
PhD thesis: "Sea-ice surface properties and their impact on the under-ice light field from remote sensing data and in-situ measurements"
- Since Oct 2013 **Member of the Helmholtz Graduate School for Polar and Marine Research**, (*POLMAR*).
- Sep– Nov 2012 **Arctic Geophysics**, *University Centre in Svalbard (UNIS)*, Longyearbyen/Norway.
- Oct 2011– June 2013 **Master of Science in Meteorology**, *Universität Hamburg*, Germany.
Master thesis: "Seasonality and spatial distribution of solar radiation under Arctic sea ice"
- Oct 2008– June 2011 **Bachelor of Science in Meteorology**, *Freie Universität Berlin*, Germany.
Bachelor thesis: "Trends and variability of tropical water vapour content in the stratosphere"

Experience

Vocational

- Jan 2017 onwards **PostDoc**, *Sea Ice Physics/Climate Sciences*, Alfred-Wegener-Institut Helmholtz-Zentrum für Polar- und Meeresforschung, Bremerhaven, Germany.
Responsibilities: Analysis of the snowpack on Antarctic sea ice from microwave satellite observations and field data. Coordination of sea-ice related field work in the Southern Ocean.
- Feb– April 2016 **Research stay abroad**, *Sea Ice Physics*, Institute for Marine and Antarctic Studies, visiting Klaus Meiners and colleagues, Hobart, TAS, Australia.
Responsibilities: Physical analysis of the under-ice light field of Antarctic sea ice.
- June 2013– Dec 2016 **Research Associate**, *Sea Ice Physics/Climate Sciences*, Alfred-Wegener-Institut Helmholtz-Zentrum für Polar- und Meeresforschung, Bremerhaven, Germany.
Responsibilities: Analysis of passive microwave satellite observations to describe seasonal changes in snow and sea-ice properties. Participation in several expeditions to the Arctic and Southern Oceans.

Field Work

- 2015/2016 **Expedition to the Weddell Sea, Antarctic, PS96 (FROSN)**, Research Vessel Polarstern.
Responsibilities: Group leader 'Sea-ice physics', deployment of autonomous measuring systems, snow depth surveys, physical snow properties, sea-ice observations, ice navigation support.
- 2014/2015 **Expedition to the Weddell Sea, Antarctic, PS89 (ANT-30/2)**, Research Vessel Polarstern.
Responsibilities: Optical light measurements with remotely operated vehicle under Antarctic sea ice, physical snow properties.
- 2014 **Expedition to the Arctic Ocean, PS86 (ARK-28/3)**, Research Vessel Polarstern.
Responsibilities: Deployment of autonomous measuring systems, snow depth surveys.
- 2013 **Expedition to the Weddell Sea, Antarctic, ANT-29/6**, Research Vessel Polarstern.
Responsibilities: Physical snow properties.
- 2012 **Expedition to Fram Strait, Arctic**, Research Vessel Lance.
Responsibilities: Shipborne oceanographical measurements, basic sea-ice measurements.
- 2010/2011 **Expedition to the Weddell Sea, Antarctic, ANT-27/2**, Research Vessel Polarstern.
Responsibilities: Shipborne oceanographical measurements, sea-ice observations.

Summer/ Winter schools

- 2015 **Winter School, 1st European Snow Science Winter School**, Sodankylä, Finland.
Lectures and application on snow measurement techniques.

Extra-curricular activities

- 2016 onwards **APECS Germany Board Member**.
- 2015 onwards **Young Scientist Speaker**, Helmholtz Alliance 'Remote Sensing and Earth System Dynamics'.
Representative of all young scientists in the HGF-EDA Steering Committee
- 2014–2015 **DokTeam Member**, *Alfred-Wegener-Institut Helmholtz-Zentrum für Polar- und Meeresforschung*, Bremerhaven, Germany.
Responsibilities: Support of new PhD students, communication, outreach
- 2014 onwards **Outreach activities**, *in German Schools*.
- 2013 onwards **Young Scientist Speaker**, Helmholtz Alliance 'Remote Sensing and Earth System Dynamics'.
Representative of the Cryosphere

Computer skills

- Scientific Advanced: MATLAB; Intermediate: ARCGIS, PYTHON, UNIX; Basic: FORTRAN
- Typography L^AT_EX, Microsoft Office

OS Linus/Unix, Windows, Mac OS X

Languages

German **Native**.
English **Fluent**, *speaking, reading, writing*.
French **Basic**, *speaking, reading, writing*.

Grants

- 2017 **ASPeCt/CliC travel grant**, to attend *IGS Symposium*, Wellington, New Zealand.
- 2016 **POLMAR outgoing scholarship**, for research stay at *IMAS*, Hobart, TAS, Australia.
- 2014 **DAAD travel grant**, to attend *IGS Symposium*, Hobart, TAS, Australia.

Contributions to Conferences and Workshops

- 2017 **International Symposium on The Cryosphere in a Changing Climate**, Wellington, New Zealand, talk.
- 2016 **AGU Fall meeting**, San Francisco, CA, USA, poster.
SCAR, Open Science Conference and Side Meetings, Kuala Lumpur, Malaysia, talk.
EGU General Assembly, Vienna, Austria, poster.
- 2015 **AGU Fall meeting**, San Francisco, CA, USA, poster.
Internationale Polartagung, München, Germany, poster.
- 2014 **Integrating Spatial and Temporal Scales in the changing Arctic system (ISTAS, ART workshop)**, Brest, France, talk.
International Symposium on Sea Ice in a Changing Environment, Hobart, TAS, Australia, talk and poster.
- 2013-2016 **Several project meetings/workshops**, for *Helmholtz Alliance 'Remote Sensing and Earth System Dynamics'*, Germany, talks and posters.

Publications

Peer-reviewed

- in prep. **Arndt, S.**, C. Haas (in prep.), Retrieval of seasonal snowmelt stages on Antarctic sea ice from satellite scatterometer observations.
- in prep. Meiners, K., **S. Arndt** et al. (in prep.), Identification of physical drivers of the floe-scale distribution of Antarctic pack-ice algae.
- under review **Arndt, S.**, K. M. Meiners, R. Ricker, T. Krumpfen, M. Nicolaus (under review), Influence of snow depth and surface flooding on light transmission through Antarctic pack ice, *Journal of Geophysical Research - Oceans*.

- 2016 **Arndt, S.**, M. Nicolaus, W. Dierking, S. Willmes (2016), Timing and regional patterns of snowmelt on Antarctic sea ice from passive microwave satellite observations, *Journal of Geophysical Research - Oceans*, doi:10.1002/2015JC011504.
- 2015 Katlein, C., **S. Arndt**, M. Nicolaus, M. V. Jakuba, S. Elliott, L.L. Whitcomb, C. J. McFarland, S. Suman, D. K. Perovich, R. Gerdes, A. Boetius and C. R. German (2015), Influence of ice thickness and surface properties on light transmission through Arctic sea ice, *Journal of Geophysical Research - Oceans*, doi:10.1002/2015JC010914.
- 2014 **Arndt, S.**, M. Nicolaus (2014), Seasonal cycle and long-term trend of solar energy fluxes through Arctic sea ice, *The Cryosphere*, 8, 2219–2233, doi:10.5194/tc-8-2219-2014.
- 2013 Nicolaus, M., **S. Arndt**, C. Katlein, J. Maslanik, S. Hendricks (2013), Correction to "Changes in Arctic sea ice result in increasing light transmittance and absorption", *Geophysical Research Letters*, doi:10.1002/grl.50523.

Erklärung

Hiermit erkläre ich, Stefanie Arndt, dass ich

1. die Arbeit ohne unerlaubte fremde Hilfe angefertigt habe,
2. keine anderen als die von mir angegebenen Quellen und Hilfsmittel verwendet habe,
und
3. die den benutzten Werken wörtlich oder inhaltlich entnommenen Stellen als solche
kenntlich gemacht habe.

Bremen, den

(Stefanie Arndt)

